

Cardiff University

School of Engineering

**The Development of Structure-Based Tidal Stream
Turbine Condition Monitoring Systems**

A thesis submitted to Cardiff University, for the Degree of Doctor of
Philosophy

By

Jianhao He

1225187

DECLARATION

This work has not been submitted in substance for any other degree or award at this or any other university or place of learning, nor is being submitted concurrently in candidature for any degree or other award.

Signed... Jianhao He (candidate)

Date ...17/4/18

STATEMENT 1

This thesis is being submitted in partial fulfilment of the requirements for the degree PhD

Signed... Jianhao He (candidate)

Date ...17/4/18

STATEMENT 2

This thesis is the result of my own independent work/investigation, except where otherwise stated, and the thesis has not been edited by a third party beyond what is permitted by Cardiff University's Policy on the Use of Third Party Editors by Research Degree Students. Other sources are acknowledged by explicit references. The views expressed are my own.

Signed... Jianhao He (candidate)

Date ...17/4/18

STATEMENT 3

I hereby give consent for my thesis, if accepted, to be available online in the University's Open Access repository and for inter-library loan, and for the title and summary to be made available to outside organisations.

Signed... Jianhao He (candidate)

Date ...17/4/18

STATEMENT 4: PREVIOUSLY APPROVED BAR ON ACCESS

I hereby give consent for my thesis, if accepted, to be available online in the University's Open Access repository and for inter-library loans **after expiry of a bar on access previously approved by the Academic Standards & Quality Committee.**

Signed... Jianhao He (candidate)

Date ...17/4/18

Acknowledgements

I would like to thank my supervisors, Roger I. Grosvenor and Paul W. Prickett, for their valuable advices and support during the whole period of my study. They not only gave me the confidence to overcome the problem, but also provided the best guidance for my research. In my darkest days, they also gave me the selfless encouragement and comfort. I think I will never forget everything about them over the past five years.

I would also like to give thanks to my friend and colleague Matthew J. Allmark for his help on my experimental work. From this handsome Welsh man, I saw his rigorous attitude towards science and friendship to friends. He made me love this country even more.

I would also like to give my acknowledgement to my mother Fengxiang Cheng for her financial support and encouragement. I also owe a debt of gratitude to my lovely girlfriend and future wife, Dr. Cao, for bringing a bright sunshine in my dark days which completely changed my destiny. They are the most important women in my life.

I dedicate this work to my father Xinglu He. I believe that he would be proud of me.

Abstract

The research presented considers the design, development and building of a structure-based condition monitoring system. A series of physical experiments were designed and conducted in a wind tunnel. This was able to initially prove the feasibility of the proposed system. Using a simulation of the continuous turbine rotation the self-initiated Phase-Angle curve was defined. The algorithms so produced were validated and tested using both the simulated waveforms and experimental data sets. This demonstrated that the proposed monitoring system was able to deal with the ever-changing flow conditions and turbine operation status.

The work showed that the use of the wind tunnel was feasible for developing the structure-based monitoring system. It has been shown that innovative ideas can be tested and validated in the wind tunnel. The relatively small size of the test rig and the utility of 3-D printing technology made the whole experiment based investigation very cost-effective. The progressive experiments were conducted to compare widely used monitoring techniques to the proposed monitoring system.

Some other physical phenomenon or extended thoughts such as blade tip deflection caused by the tower were considered and may be of interest to other researchers. The final discussion of the work presented was to introduce the potential problems and difficulties in applying the proposed system in the marine environment. This considered the sensor design, system installation, application methods and algorithm optimisation. This could further serve the useful information for the relevant researchers and the experiment or deployment of the proposed system on full-size turbine.

Contents

1. Introduction	1
1.1 Background Research	1
1.2 Tidal Energy	4
1.3 Tidal Stream Turbine.....	5
1.4 Condition Monitoring System for HATT.....	6
1.5 Research Objectives	7
1.6 Thesis Structure.....	8
2. Literature Review	10
2.1 Current Technologies for Tidal Energy	10
2.1.1 Tidal Barrier	11
2.1.2 Tidal Lagoon	13
2.1.3 Dynamic Tidal Power (DTP)	14
2.1.4 Tidal Stream Turbines (TST)	15
2.1.5 Yaw and Pitch Control System.....	21
2.2 Tidal Stream Turbines Evaluation	23
2.2.1 Seagen S and SeaFlow	24
2.2.2 OpenHydro.....	27
2.2.3 AK1000 and AR1000	29
2.2.4 HS300 and HS1000.....	31
2.3 Numerical and Experimental Studies of TST	32
2.3.1 Scaled Flume and Wind Tunnel Testing for Scaled TST	34
2.3.2 Structural-based Analysis of TST	37
2.3.3 Flow Profile and ADCP Measurement Techniques.....	42
2.3.4 Blade-Tower Interaction	47
2.4 Experience in Blade Health Monitoring (BHM) for Wind Turbine.....	55
2.4.1 Acoustic Emission (AE) Monitoring.....	57
2.4.2 Infrared Thermography (IRT)	58
2.4.3 Optical-Based Strain Measurements	59
2.4.4 Laser-based Tip Deflection Measurement	60
2.4.5 Feasibility Assessment	61
3. An Experiment-based Investigation on Dynamic Behaviour of the Small- scaled Turbine Structure	63
3.1 Introduction.....	63
3.2 Experiment 1	65
3.2.1 Experimental Setup	65
3.2.2 Experimental Procedure	75
3.2.3 Results & Analysis	76
3.2.4 Summary for Experiment 1	81
3.3 Experiment 2	82

3.3.1 Experimental Setup	82
3.3.2 Experimental Procedure	84
3.3.3 Results & Analysis	85
3.3.3 Summary for Experiment 2	89
4. An Innovative Method of Flow Pressure Profile Measurement and Blade	
Status Monitoring	91
4.1 Introduction	91
4.2 Preliminary Test	92
4.2.1 PAW sensors	93
4.2.2 Method for Preliminary Test	95
4.2.3 Results	96
4.2.4 Summary	97
4.3 Experimental Arrangements	98
4.3.1 3-D Printed Blades	99
4.3.2 Stanchion and Base Frame	99
4.3.3 Monitoring System for Test	101
4.4 Experiment Procedure	103
4.4.1 Static Test	104
4.4.2 Dynamic Test	105
4.5 Experimental Results and Analysis	108
4.5.1 Static Test	108
4.5.2 Summary	112
4.5.3 Dynamic Test	114
4.5.4 Summary	125
5. Pressure Signal Simulation and Blade Health Monitoring System	127
5.1.2 Simulation with Different Scenarios	129
5.2 Analysis with Blade Position	131
5.2.1 Duty Cycle Analysis	131
5.2.2 Initial Phase Angle Analysis	137
5.2.3 Overlap	144
5.3 The Analysis without Blade Position	148
5.4 Summary	151
6. Discussion	153
6.1 Wind Tunnel	153
6.2 Vibration-based Investigation on Blade Failures Of TST	157
6.2.1 Experiment 1	157
6.2.2 Experiment 2	160
6.3 Flow Profile Measurement and Pressure Variation on the Tower	160
6.3.1 The Flow Profile Measurement	161
6.3.2 The 3-D Printed Blade	163
6.3.3 Static Test	164

6.3.4 Dynamic Test	165
6.4 Pressure Signal Simulation and Analysis	168
6.4.1 Duty Cycle and P-A Curves	169
6.4.2 Overlap.....	170
6.4.3 Blade Health Monitoring (BHM) system.....	170
7. Conclusions	173
7.2 Recommendations and Future Work	175
7.2.1 Sensor Design	176
7.2.2. Blade Positioning System	177
7.2.3. Monitoring System.....	177
7.2.4. Structural Design.....	178
7.2.5. Flow Conditions	179
7.2.6 Implementation on Full-scale TST.....	179
References	181

List of Figures

Figure 1.1 The plan of the GHG Emissions Reductions to 2050.	2
Figure 1.2 Installed capacity (MW) of renewable energy sources in the UK between 2000 and 2015. Source: DBIS, 2017.....	3
Figure 2.1 Rance tidal power station: Source: Yekang and Schubert, 2011.	12
Figure 2.2 Changes of three gorges dam within 20 years. Source: Yue, 2016.....	12
Figure 2.3 Schematic diagram of tidal lagoon Source: Tidal Lagoon Cardiff Ltd, 2015.....	14
Figure 2.4 Top-down view of a DTP dam. Source: Hulsbergen, 2008	15
Figure 2.5 Basic configuration of a HATT. Source: Aqua-RET, 2008.	16
Figure 2.6 Forces acting on the turbine blade Sources: Ragheb, 2013.....	18
Figure 2.7 Schematic of actuator disc and tidal stream tube. Manwell et al, 2009	20
Figure 2.8 $C_p - \lambda$ curves	21
Figure 2.9 Block diagram of the WTPC system. Source: Fleming et al, 2013.....	22
Figure 2.10 Example of a yaw system. Source: Lee et al, 2013	23
Figure 2.11 Seagen S tidal turbine located in Strangford Lough; a) shows that rotor blades are lifted for inspection; Right) shows illustration of Seagen S system in operation. Source: MCT, 2008.....	25
Figure 2.12 General arrangement of the SEAFLOW turbine system off the north coast of Devon Source: Europe Commission, 2005. Elghali et al, 2007.	26
Figure 2.13 Evolution of the OpenHydro tidal turbine systems Sources: Energy Insight, 2009.....	28
Figure 2.14 AK1000 Tidal turbine assembled on the land Source: Jupiter Hydro Inc.,2012.....	30
Figure 2.15 Installation of the AR1000 tidal turbine Source: Jupiter Hydro Inc., 2012.....	31
Figure 2.16 Structure of the HS1000 tidal turbine system Source: Mcewen,2012.....	32
Figure 2.17 Aspects to modelling a TST. Source: Robinson and Byrne, 2008.....	33
Figure 2.18 General water flume test arrangement. Source: Allmark, 2017	35
Figure 2.19 Configurations of the scaled TST model. Source: Allmark, 2017.....	36
Figure 2.20 Schematic view of blade deformation. Source: Rezaei et al, 2015	38
Figure 2.21 Tip deflection and cantilever beam with UDHL. Source: Tartibu and Kilfoil, 2012.....	39
Figure 2.22 Flap-wise tip deflection of the turbine blade in different azimuth positions	40
Figure 2.23 A typical blade region classification.....	41
Figure 2.24 Velocity profile and power distribution through water column. Source: Fraenkel, 2011	43
Figure 2.25 Schematic diagram of the ADCPs in operation	44
Figure 2.26 Estimated velocity profile in vertical direction. Source: Epler et al (2010)	45
Figure 2.27 Changes of seabed-based ADCP after two years of operation. Source: Houde, 2012.....	46

Figure 2.28 Schematic diagram of downwind B-T interactions. Source: Gan et al, 2017.....	48
Figure 2.29 Normalized power coefficient over one revolution. Source: Frau et al, 2015.....	49
Figure 2.30 Evolution of one blade flap-wise moment over one rotor revolution. Source: Frau et al, 2015	50
Figure 2.31 Simulated vortex lattices and wake panels. Source: Kim et al, 2011	51
Figure 2.32 Normal force versus azimuth angle in various yaw errors at 5 m/s. Source: Kim et al, 2011	52
Figure 2.33 Tower pressure distribution for 5 and 10 m/s wind speed. Source: Wang et al, 2012.....	53
Figure 2.34 Examples of the faulty tidal turbine system. Sources: Elasha et al, 2014 and Zhou et al, 2016.....	54
Figure 2.35 Proposed configuration of acoustic wireless units. Source: Bouzid et al, 2002.....	58
Figure 2.36 Thermal image of the rotating blades. Source: Meinschmidt, 2006.....	59
Figure 2.37 Schematic of fiber optic sensors	60
Figure 2.38 Schematic diagram of the laser-based tip deflection measurement.....	61
Figure 3.1 Schematic diagrams of two test rigs	64
Figure 3.2 Armfield C2 subsonic wind tunnel	66
Figure 3.3 Measured point wind speed along the vertical direction in the wind tunnel	67
Figure 3.4 Overview of the small wind tunnel test rig. A) shows pro/e 3-D design, B) shows upper platform with small motor structure, C) shows location of the accelerometer. D) shows the rear view of the tunnel without motor structure.	68
Figure 3.5 Wind speeds in the small wind tunnel with different input voltage settings	69
Figure 3.6 Optimal and deliberately made faulty blade.....	70
Figure 3.7 Schematic diagram of the hardware connections	71
Figure 3.8 PmodHB5 block diagram	71
Figure 3.9 Block diagram of the Main program. A) Timed Loop for reading and recording the 3-axis vibration signal, B) While Loop for generating the PWM signal by setting the duty cycle, C) While Loop for calculating the instant rotational speed.	72
Figure 3.10 FFT LabVIEW program for the 3-Axis vibration data.....	74
Figure 3.11 Coordinate system of the vibration signal	74
Figure 3.12 Data logging program in the PC	75
Figure 3.13 Rotational speed of the two rotors in different wind speed (without speed control).....	77
Figure 3.14 Amplitude spectrums of the OBM with 0.3, 0.5 and 0.7 duty cycle.	78
Figure 3.15 Amplitude spectrums of the reference blade operated at 240 RPM with different wind speeds	80
Figure 3.16 Amplitude spectrums of the offset blade operated at 240 RPM with different wind speeds	81

Figure 3.17 Cross-section of the tower and the blade part.....	83
Figure 3.18 Final assembly of the testing rig.....	84
Figure 3.19 Results of the rotational speed in normal operation	85
Figure 3.20 Vibration data for reference blade at 40% wind speed and 1 duty cycle... 86	
Figure 3.21 Vibration data for offset blade at 40% wind speed and 1 duty cycle	86
Figure 3.22 Waterfall amplitudes frequency spectrum for 21 optimum blades tests....	87
Figure 3.23 Comparison of amplitude frequency spectrum results.	88
Figure 4.1 Test rig of the preliminary test.....	93
Figure 4.2 Schematic diagram and picture of the PAW sensor. Source: RT Corporation, 2013.	94
Figure 4.3 Results of the wind speed measurement in initial test.....	96
Figure 4.4 Schematic diagram of the test rig	98
Figure 4.5 Instrumented 3D printed blade	99
Figure 4.6 Configurations of the test rig	100
Figure 4.7 Schematic diagram of the monitoring system	101
Figure 4.8 Front panel of monitoring system.....	102
Figure 4.9 A screen shot of the flow pressure measurement on the front panel	103
Figure 4.10 Diagram of the signal processing	107
Figure 4.11 Procedure of the resampling each loop.....	108
Figure 4.12 Wind pressure distribution on the tower at different wind speeds.....	109
Figure 4.13 Pressure variation on the tower with 3 cm tip clearance.	110
Figure 4.14 Pressure variation on the tower with 5 cm tip clearance.	110
Figure 4.15 Pressure variation on the tower with 60% wind speed.....	111
Figure 4.16 Static deflections at 60% wind speed.	112
Figure 4.17 Deflections of the blade in vertical position in static test.....	112
Figure 4.18 Tip deflection time series.....	114
Figure 4.19 Comparison between the static and dynamic tip deflection	115
Figure 4.20 Example of the estimated flow profile	116
Figure 4.21 Top view of the mesh plot of the pressure variation in 60% wind speed with s1 and 3 cm tip clearance.	117
Figure 4.22 Comparison of the pressure variation between 3 cm, 4 cm and 5 cm tip clearances.....	118
Figure 4.23 Comparison of the pressure variation in different wind speed.....	119
Figure 4.24 Pressure variation on the tower in 60% wind speed with different rotational speed.	120
Figure 4.25 Pressure variation on the tower with different widths.....	121
Figure 4.26 Comparison between the Optimal condition and Failure 1	121
Figure 4.27 Pressure comparisons between Optimal and F1	122
Figure 4.28 Pressure comparisons between F1 and F1+F2	123
Figure 4.29 Pressure comparisons between F1+F2 and F1+F2+F3	124
Figure 4.30 Pressure comparisons between Blade 1 and Blade 2.....	125
Figure 5.1 Procedure of the pressure signal simulation for one rotation.	128
Figure 5.2 Simulated trapezoidal waveforms	132
Figure 5.3 State levels estimation of the trapezoidal wave.....	133

Figure 5.4 Duty cycles of the trapezoidal wave TW1&TW2	134
Figure 5.5 Duty cycles of the trapezoidal wave TW3&TW4	134
Figure 5.6 Comparison between SN and SF1	135
Figure 5.7 Duty cycles of the SN and SF1	136
Figure 5.8 Frequency spectrums of the simulated trapezoidal waveforms.....	138
Figure 5.9 Simulated trapezoidal waves and corresponding frequency spectrums	139
Figure 5.10 Simulation of the occurrence of Failure 1 on Blade 3; a) is the simulated signal in 180 seconds; b) is the zoomed signal of one rotation of 3 reference blades in first 6 seconds; c) is the zoomed signal of one rotation of 2 reference blades and 1 faulty blade in from 90 to 96 second; d) is the zoomed waterfall plot of the frequency spectrums.	140
Figure 5.11 Fourier decomposition of the simulated pressure signal SN.	141
Figure 5.12 Extra simulated pressure signals between SN and SF1	142
Figure 5.13 P-A curve from SN to SF1.....	143
Figure 5.14 Complete P-A curves	143
Figure 5.15 Overlap of the pressure difference between Reference and Failure 1	145
Figure 5.16 Overlap of the pressure differences between Failure 1 and Failure 2	146
Figure 5.17 Overlap of the pressure differences between Failure 2 and Failure 3	147
Figure 5.18 Logical diagram of the proposed BHM system.....	148
Figure 5.19 Comparison between the simulated pressure signal with and without blade position	149
Figure 5.20 Generation of the logical signal.....	150
Figure 5.21 Procedure of the pressure signal processing without blade position signal	151

List of Tables

Table 2-1 The specifications of pre-commercial tidal turbines.	24
Table 2-2 Shipboard ADCP configuration. Source: Epler et al, 2010.....	44
Table 3-1 Wind speed and duty cycle settings for Experiment 1.....	76
Table 3-2 Wind speed and duty cycle settings for Experiment 2.....	84
Table 4-1 Dimensions of the round holes	95
Table 4-2 Arrangement of the blade in static and dynamic tests.....	104
Table 4-3 Static tests settings	105
Table 4-4 Dynamic tests settings	106
Table 5-1 Simulation of the estimated pressure signals from PAW1	130

Acronyms

ADCP	Acoustic Doppler Current Profiler
AE	Acoustic Emission
BBM	Bent Blade Motor
BBW	Bent Blade Wind
BHM	Blade Health Monitoring
BPs	Blade Positioning system
B-T Interaction	Blade-Tower Interaction
CMs	Condition Monitoring system
DTP	Dynamic Tidal Power
FFT	Fast Fourier Transform
GHG	Greenhouse-Gas
HATT	Horizontal Axis Tidal Stream Turbine
IGBT	Insulated-gate bipolar transistor
IRT	Infrared Thermography
MXP	myRIO Expansion Port
NDT	Non-destructive testing
NVCM	Nonlinear Vortex Correction Method
P-A	Phase Angle
PMG	Permanent Magnet Generators
PSP	Pressure-Sensitive Paint

PWM	Pulse Width Modulation
RBM	Reference Blade Motor
RBW	Reference Blade Wind
RPM	Revolutions per Minute
SHM	Structural Health Monitoring
TSR	Tip Speed Ratio
TST	Tidal Stream Turbine
VATT	Vertical Axis Tidal Stream Turbine
WT	Wind Turbine
DAQ	Data Acquisition
WTPC	Wind Turbine Pitch Control system
UDHL	Uniformly Distributed Hydrodynamic Load

Nomenclature

α	Axial Induction Factor
λ	Tip Speed Ratio
ρ	Fluid Density, $\text{kg} \cdot \text{m}^{-3}$
ω	Rotational Velocity, Rads^{-1}
A	Rotor Area, m^2
A_L	Cross Sectional Area of The Aerofoil
C_p	Power Coefficient
C_T	Thrust Coefficient
C_θ	Torque Coefficient
d	Unbalance Distance
$F_{unbalance}$	Unbalanced Force, N
f_s	Sampling Frequency, Hz
U	Flow Velocity, $\text{m} \cdot \text{s}^{-1}$
P_T	Total Extracted Power, W
R	Radius of the Rotor, m
T	Torque, $\text{N} \cdot \text{m}$
L	Lift Force, N
D	Drag Force, N
ΔP	Pressure Difference,

1. Introduction

This chapter introduces the background to research into renewable power generation and, in particular, tidal stream turbine technologies and condition monitoring of tidal turbines. The latest energy contribution trends for the UK and associated energy targets are presented. The beneficial tidal resources in the UK and tidal turbine technologies are discussed. Also of relevance are wind turbine industry applications and related technologies that have maturity. A discussion of the transferability of condition monitoring systems from wind turbine applications to tidal turbines is included. The above aspects set the framework for the motivations and objectives of the current research.

1.1 Background Research

The latest report from DESA (United Nations, 2017) shows that the world's population was estimated to be 7.6 billion. Further, there are one billion new-borns over the past 12 years. Due to the dramatically increased world population, the demand for energy poses many challenges. For example, the total energy consumption of the UK reached 2249 TWh in 2014 (Dietz, 2015) with approximately 30% increase compared to the consumption (1724 TWh) in 2012 (DECC, 2013). Developing countries such as China, where industrial electricity accounts for 71% of total power consumption (Lockhart, 2017), consume more resource to maintain their rapid economic growth. Also noted are lower power efficiencies and power structure is relatively simple (Zhu and Zhao, 2016). Climate and environmental change, mainly attributed to greenhouse-

gas (GHG) emissions, is a factor under consideration by many countries and organisations. Spanning the Kyoto Protocol (1997) to The Paris Agreement (2017), 195 countries have signed many agreements and each of them have respectively developed national energy plans during that 20-year period (UNTC, 2016). The UK has a new 2050 target of achieving at least an 80% reduction of GHG emissions (set by the Committee on Climate Change (CCC)). These dramatic changes are evident in Figure 1.1 (Climate Change Act 2008).

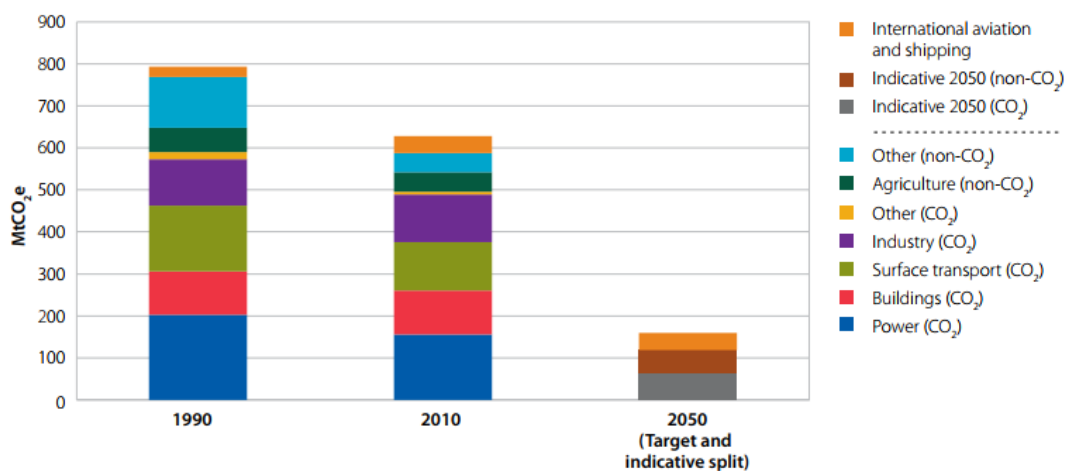


Figure 1.1 The plan of the GHG Emissions Reductions to 2050. Source: NAEI, 2012; CCC analysis.

The three main sources of the GHG emissions (before 2010) are surface transport, buildings and power generation. In order to meet this target renewable sources of energy as an alternative to coal-fired power are fundamental. By 2015, renewable energy contributed 23.7% of global electricity generation. The renewable technologies extract energy from wind, hydro, solar and biofuel sources and have obtained the highest investment, especially in the US and China (REN21, 2016). In the UK, relatively

mature technology and unique geographical features will offer huge advantages for the diversification of mainstream renewable sources. Figure 1.2 shows the growth in installed capacity for a range of renewable technologies, for the period 2000 to 2015.

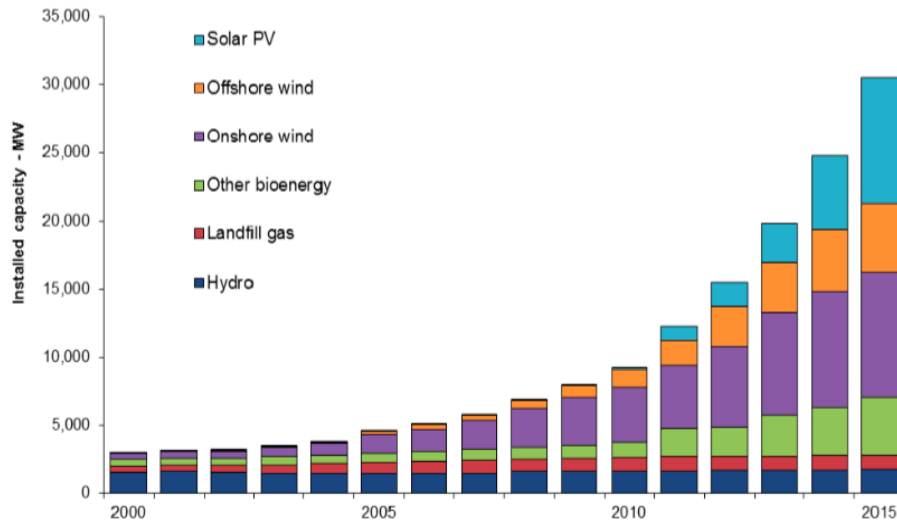


Figure 1.2 Installed capacity (MW) of renewable energy sources in the UK between 2000 and 2015. Source: DBIS, 2017.

There are particular effects, within the overall trends of Figure 1.2 that are worthy of note. In 2006, there was only 12 MW of photovoltaic (PV) capacity installed in the UK. Following the popularization of an (incentive) feed-in-tariff in 2010, a rapid growth equating to 230,000 solar power projects occurred between 2010 to 2011 (DECC, 2015). With the reduction of the cost of PV panels, the first large scale solar farm was built in Leicestershire in 2013. The largest solar farm in the UK at present is located in Bournemouth. Both of the projects made a major contribution to solar energy generation in the year of their completion. By end of the 2015, the total installed capacity of solar PV was more than 10,000MW. Also of note is that onshore and offshore wind farms have maintained steady and rapid growth in the past decade.

Offshore wind has much greater potential to generate power with higher prevalent wind speeds. However, with much higher capital and maintenance costs for offshore, the onshore farms appear to have been given priority for development and investment. As for hydropower, although it accounted for 21% of electricity generation from renewable sources in 2009 (DECC, 2011), its installed capacities have not changed in the past fifteen years as many of the related projects are yet connected to the grid. The hydropower sector is the focus for the current research.

1.2 Tidal Energy

In simple terms, tidal energy stems from the periodic changes of seawater levels due to the relative motions of the Earth-Moon system. Greater tidal range can provide huge increase in the potential of power generation. Unlike other sources of energy which originate from the Sun, tidal energy is relatively unaffected by weather (Robert, 2007). Energy extraction will depend on installation specific factors such as the local topography of the seafloor and coastline. However, these will not change significantly over long periods.

As one of the forms of hydropower, tidal energy has greater potential to serve the future electricity generation due to its steady stream of kinetic energy and good predictability (Tousif et al 2011).

At present, tidal energy is predominantly harvested in four forms (Morris, 2014): 1, Tidal barrier. 2, Dynamic tidal power. 3, Tidal lagoon. 4, Tidal stream turbine. The details of these are given in Chapter 2. The latter is of primary concern in this work and is introduced in the following section

1.3 Tidal Stream Turbine

The Tidal Stream Turbine (TST) as a concept was first proposed in 1970 (Caraiman et al, 2010), being termed as a stand-alone machine that extracts the energy from water currents in ocean or estuary in the same way as the wind turbine uses wind energy. The structural designs of TSTs have been a variety of fundamentally different types. According to the orientation of the main shaft with the flow, TSTs operate as a horizontal axis tidal stream turbine (HATT) or a vertical axis tidal stream turbine (VATT). Although the performance of the VATT are numerically (Hyun et al, 2010) or physically (Harries et al, 2016) evaluated and proved, the most of the current pre-commercial or commercial TSTs are HATT (Chen et al, 2012). There is much greater structural similarity between conventional wind turbines and HATTs, and thus much of the design, operation and applied monitoring techniques of wind turbines is more directly applicable (Burton et al, 2000). Typical differences such as Reynolds number regimes, stall characteristics and the possible occurrence of cavitation do distinguish the two types of turbines (Batten et al, 2005).

For commercial viability, a minimum average flow speed 2 m/s in turbine operation is required and the ideal flow speed should be between 1.5 and 3.5 m/s (Giorgi and Ringwood, 2013). After a series of geographic analyses, a report from Black & Veatch Ltd (2005) suggests that the water depths at potential TST deployment sites in the UK should be between 25 and 40 metres. Accordingly, the rotor diameter of the TST should be between 10 and 20 metres. In contrast, the rotor diameter of typical wind turbines has increased from 17 to 126 metres over the past 30 years. In addition to the

deployment site limitations for tidal turbines, there are huge loads acting on the blades. A parameter comparison between wind and tidal turbines, for equal output capacity, conducted by Elasha et al (2014) shows that the total thrust load on the latter could be 5 times larger. With the ever-changing flow velocities and non-symmetric flow profiles, higher fatigue loads prevail for TST blades. A detailed evaluation of representative TST designs follows in Chapter 2.

1.4 Condition Monitoring System for HATT

As the development of the TST is still in infancy, the monitoring system for each installed full device could be different with the monitoring targets, technology, operating environment. In addition, lack of standardisation throughout industry made that there is no clear unified concept of the CMs for the TST (Elasha et al, 2014). Although much of the information about design of TST and the corresponding CMs are not available for research organisations or institutions, CM and fault diagnosis are considered to be fundamental in increasing the long-term performance of turbine and investor confidence. An ideal Condition Monitoring system (CMs) for TST should meet the following requirements:

- Detects the developing faults and helps to avoid catastrophic failures.
- Remote access by web enabled reporting tool.
- Capture reliability/fault history for establishing the scheduled maintenance.
- Collect field information includes environment and ecology.
- Correct and timely decision making based on the real-time monitoring results.

- The reliability and long-term performance of the CMs itself must be secured.

The benefits of CMs for operating tidal turbine are summarized as below:

- ✧ Reduce risk of unscheduled shutdowns and improve the availability of the energy extraction (Yang et al, 2010).
- ✧ Predict remaining service life of the device or components and take actions in advance.
- ✧ Reduce maintenance costs which includes the shipping for replacing the faulty parts.
- ✧ The current field test data could conduce to the current turbine design iterations.

1.5 Research Objectives

The aims of this work were to consider the structural-based condition monitoring of the tidal turbine. By developing and using the proposed new method of the flow profile measurement, to realise the real-time monitoring of the blade health. The details of the work are listed in the following objectives:

- Development of the cost-effective research method and test rig for tidal turbine, which includes 3-D printing technology, wind tunnel test, sensors selection and structure design.
- To investigate the feasibility of the vibration-based monitoring for the entire structure in different turbine operating conditions.

- Design of scaled and simplified turbine structures for testing in different operating conditions. Utilise wind pressure variation on the tower for each set-up to evaluate the feasibility of using the blade wake to predict the blade status.
- Utilise the results of the physical experiments to simulate the continuous operation of a three-bladed turbine. To develop the analytical method for the simulated pressure signals and initially create a new system that combines the real-time flow profile monitoring and the blade health monitoring of the tidal turbine.

1.6 Thesis Structure

The remaining chapters of this thesis are structured as follows:

Chapter 2- gives a description of introduction and literature review of tidal stream turbine technology. To start with, the current technologies for extracting the tidal energy are summarised. Then, a detailed evaluation of the existing TST projects is given. Next, a selection of findings from literature relating to TST research is presented. The flow profile measurement and blade-tower interaction are highlighted. Last, the experience from blade health monitoring technique of wind turbines is discussed.

Chapter 3- presents an initial study of the dynamic behaviour of the small-scaled wind turbine structure in wind turbine, which aims to help establish an overlap FFT analysis node for blade status monitoring. Two test rigs were designed for capturing and understanding the characteristics of the turbine vibration caused by the rotor blades.

Chapter 4- introduces a cost-effective test rig with independent blade and pillar structures for the validation of the innovative methods of the wind profile measurement

and the proposed blade health monitoring. The LabVIEW-based monitoring system was developed for the experiment. The blade-tower interaction was studied by the static and dynamic test by using the data from strain gauge and PAW sensors (A pressure sensor designed by RT robot company, Japan). The 3-D pressure variation on the pillar was created by using the experimental data.

Chapter 5- presents the signal processing methods for the proposed blade health monitoring system. A series of the pressure signals were simulated by using the experimental data with different settings. The duty cycles analysis was created for initial failure detection of the simulated signals. The initial phase angle and the amplitude at the blade passing frequency are used for detailed analysis. With the overlap of simulated signals from other PAW sensors, a comprehensive blade health monitoring system was established

Chapter 6- discusses the findings from all the experiments conducted in the wind tunnel. The advantages of the utility of the wind tunnel to research the condition monitoring system of the tidal stream turbine are given. It also focuses on the discussion about the proposed technique and monitoring system applied on full-scaled TST.

Chapter 7-summaries the contribution of this research work and some considerations for the future experiments in the water flume.

2. Literature Review

This chapter introduces the background of tidal stream turbine (TST) technology and its application of condition monitoring system (CMs). The dynamic behaviour of the turbine blades and related approaches to blade health monitoring (BHM) are presented. To start with, the three forms of extracting tidal energy are described and compared with each other in detail. The evaluations of the existing, currently pre-commercial tidal turbines are given. At present, due to commercial considerations, most of the information about the full-scaled TST are not available in the public domain. This has prompted the use of scale turbines in water flume and wind tunnel tests. Associated research into factors such as blade status (expressed in terms of pitch angle, tip deflection and blade geometry), turbine performance and dynamic behaviour is then summarised. A specific overview of the Acoustic Doppler Current Profiler (ADCP) is given to illustrate the current challenges which are researched in thesis. Consideration of the influence of flow profile and blade-tower (BT) interactions on the turbine operation are presented. Finally, some mature BHM technologies mainly applied in wind turbine CM are evaluated to consider the feasibility of transferring them for TST CM.

2.1 Current Technologies for Tidal Energy

There are three main categories of tidal energy: tidal range, tidal stream (current) and their hybrids (Sandeep, 2014). As Chapter 1 mentioned, the current methods of extracting tidal energy can be classified into four methods based on the method of

construction and their location. These are: Tidal barrier, tidal lagoon, dynamic tidal power (DTP) and TST. The first two generate power by transferring the potential energy provided by the tidal range. This usually means the operation of some form of water turbine in which the flow is generally converted to electricity in the same way as with a conventional hydro-electric dam project. A TST converts the kinetic energy of tidal stream to electricity in a similar fashion as a wind turbine/generator. As an untried but promising hybrid application, DTP, is designed for the countries or regions that has a longer coastline. Followed by the feasibility study for two locations in China in 2014, the design of its first project will be completed by 2020 (Steijn, 2015). Each of these technologies is now briefly reviewed.

2.1.1 Tidal Barrier

The tidal barrier is a specialised dam constructed across the full width of an estuary to create a tidal basin. By controlling the water levels, the generators under the barrier can efficiently produce power during the selected periods. As one of the best-established methods, a tidal barrier currently offers lower operating costs and higher energy efficiency than other forms. It deploys mature and traditional hydraulic engineering methods. The first tidal barrier was constructed in the estuary of the River Rance in France and has been used to generate electricity for 50 years with 500 GWh annual output (Yekang and Schubert, 2011). Figure 2.1 shows the installed barrier, which has a length of 750m. In addition to generating power this has become an important cross-river traffic route for local users.



Figure 2.1 Rance tidal power station: Source: Yekang and Schubert, 2011.

However, there are some disadvantages related to such a tidal barrier which may cause long-term concerns to many different organisations. First, its potential impact on the local ecosystem is not always positive. An example of this may be the Three Gorges Dam in China (Yue, 2016), shown in Figure 2.2.



Figure 2.2 Changes of three gorges dam within 20 years. Source: Yue, 2016.

Although relating to a hydro power scheme the known problems with this installation suggest that the assertion that some of this concern can be related to tidal barrier

installations is not unreasonable.

The first concern is that the original state of the local environment, especially the condition of the land, is impossible to recover within the short term. Secondly, the selection of a site suitable for a tidal barrier is very difficult. It brings with it potentially extremely high construction costs and difficulties. Operational and maintenance costs can also be very high, particularly in the context of a wider estuary like the Severn estuary (Wentworth, 2013). Thirdly, the barrier restricts vessel access to open water and reduces the convenience of established routes (Thresher, 2011).

2.1.2 Tidal Lagoon

The concept of a tidal lagoon is derived from improvements to the functions of the tidal barrier. It is a potentially viable approach and a number of construction plans are ongoing. Figure 2.3 shows this approach has a similar structure and operating principle to a tidal barrier. However, the dam in which the turbines are installed is constructed to enclose an area of coastline rather than an outlet to the sea. Proposers of such schemes suggest that the isolated coastal environment created will enhance the growth of plants and animals along the coast and can expand the available space of the original water for leisure activities and sports. Due to the much less specific requirements this type of project has more optional sites within the globe than the tidal barrier but retains many of the advantages of the latter. A detailed comparison between tidal lagoons and tidal barriers has been reported (Crumpton, 2004). This involves consideration of capital costs, regional effects, transport considerations and environmental effects

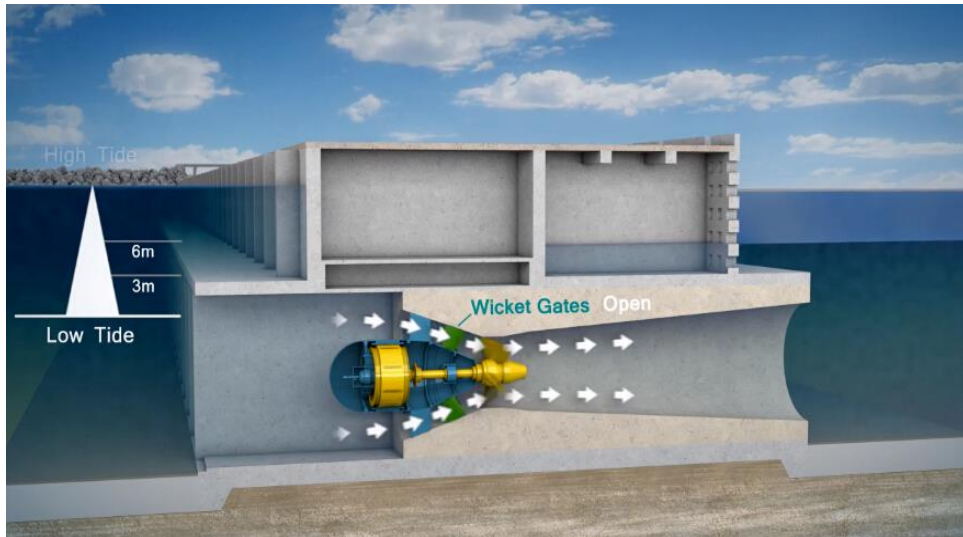


Figure 2.3 Schematic diagram of tidal lagoon Source: Tidal Lagoon Cardiff Ltd, 2015

One of the benefits brought by a tidal lagoon construction project is in creating many job opportunities in the local community before the project starts to operate. For example, the project proposed for Cardiff is estimated to create at least 1900 full time engineering jobs, covering a range of skill levels (Tidal Lagoon Cardiff Ltd, 2015). Another predictable benefit is that the water quality of the project location will be greatly improved as the sediment brought by the high tide is blocked by the barrier (Isshiki et al, 2016).

However, some of the potential problems associated with intermittent power generation have been raised (Todeschini 2017). This work suggested a solution implemented at La Rance tidal barrier: Pumping additional water into basin at low tide for continuous power generation (MacKay, 2009). A report from De Laleu (2009) proved that 10% additional energy is annually generated at La Rance due to this solution.

2.1.3 Dynamic Tidal Power (DTP)

DTP is an innovative concept that was proposed by Hulsbergen K. and Steijn R. in

1997 (2005). As shown in Figure 2.4, a dam-like structure with a 'T' shape is built from the shore perpendicular to the sea. The blue and red sea area respectively indicate low and high tides. A number of simulation results have estimated that at least a 30-km dam length is required to achieve economic viability (Hulsbergen et al, 2008). Although there is no operational installation to support this tentative plan, some other benefits and functions can be expected due to the characteristics associated with this site, namely: tsunami protection, created aquaculture and extended harbour functions.

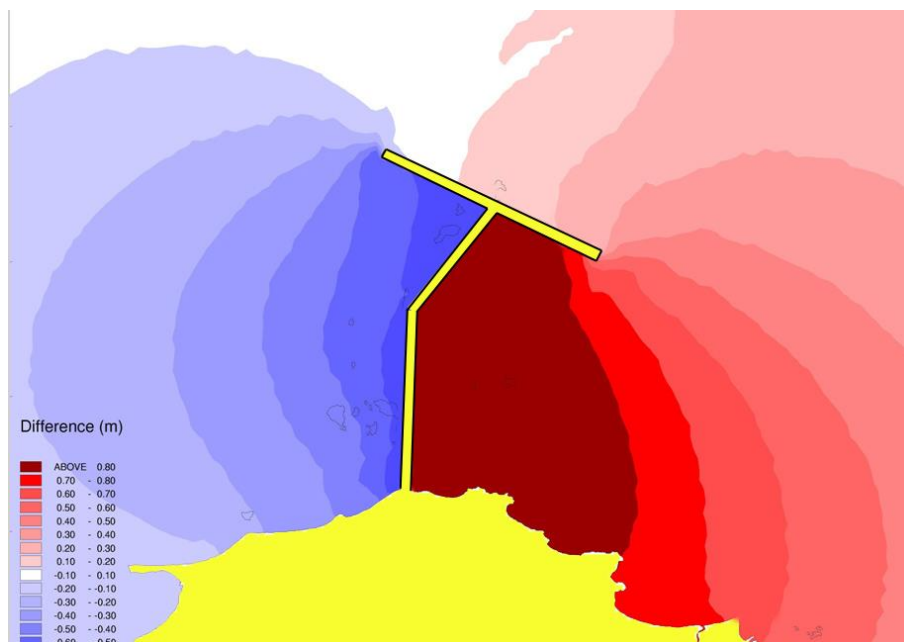


Figure 2.4 Top-down view of a DTP dam. Source: Hulsbergen, 2008

2.1.4 Tidal Stream Turbines (TST)

. The advantages of the TSTs can be summarised as

- Individual devices can be sized to meet the requirements of the specific and or local environment
- The capital cost for project construction is lower
- They are less disruptive to wildlife

- They form no barrier for sea transportation

There are a number of TST configurations, including HATT and VATT. The work in this thesis is primarily concerned with HATTs which are by far the most commonly deployed TST. An example of the HATT configuration is shown in the Figure 2.5.

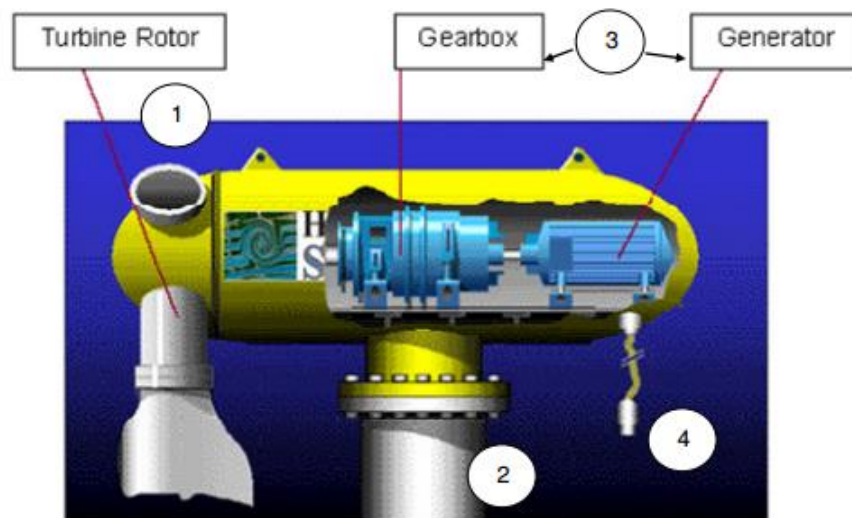


Figure 2.5 Basic configuration of a HATT. Source: Aqua-RET, 2008.

In this configuration, the essential features of a HATT are:

- 1) The rotor blade which extracts the flow normal to the swept area.
- 2) The tower which supports the nacelle.
- 3) The power train.
- 4) The cable connected to the onshore control system and grid.

It is helpful at this stage to outline the basic theory associated with the operation of a HATT.

The available max power within the swept area of the rotor can be calculated as:

$$P_{max} = 0.5 \rho A U^3 \quad (3.1)$$

Where ρ is the seawater density, A is the swept area of the turbine and U is the

velocity of the flow. Note that the density of the seawater varies depending on the temperature and salinity. The theoretical maximum power cannot be fully extracted by any turbine. The Power coefficient, C_p , is the ratio of the power extracted by the HATT to the theoretical power and was initially introduced by Albert Betz (1919). It is given by the equation:

$$C_p = \frac{P_T}{P_{max}} = \frac{P_T}{0.5 \rho A U^3} \quad (3.2)$$

After transformation,

$$P_T = 0.5 \rho A U^3 * C_p \quad (3.3)$$

Where P_T is the actual power extracted by the turbine. Betz indicated that the power coefficient of any turbine cannot be more than the factor 16/27 (59.3%) and performance close to this limit has been achieved in wind turbines (Yurdusev et al, 2006). The performance characteristic of a HATT can be quantified by this factor (Aleem et al, 2014). Note that the power coefficient of the currently deployed HATTs is reported to be more than that for a conventional wind turbine (Roberts et al, 2016). These instances relate to blockage effects in the cases where the turbine is of significant size with respect to the surroundings.

According to hydrodynamics, the geometry of the turbine blade is another important feature on determining the power coefficient. Figure 2.6 shows, that there are three forces being applied on the blade.

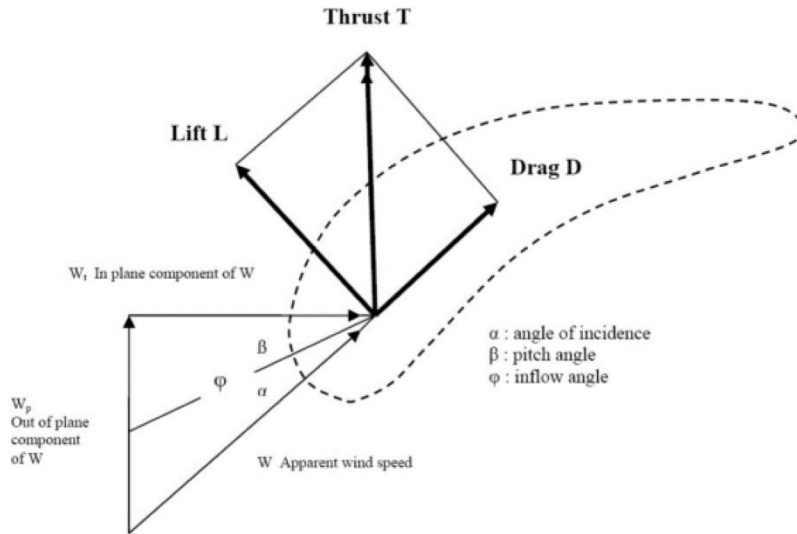


Figure 2.6 Geometry of forces acting on aerofoil; Ragheb 2013

The lift force, L , acts perpendicular to the tidal stream. According to Bernoulli's principle (Sources: Ragheb, 2013), the pressure on the top blade surface are lower than that on at bottom and this pressure difference causes the lift force. Consideration of the lift force can be used to express a lift coefficient as:

$$C_L = \frac{(L/A_L)}{0.5\rho U^2} \quad (3.4)$$

Where A_L is cross sectional area of the aerofoil.

In a lift-based tidal turbine, a high lift to drag ratio (L/D) is needed to obtain a higher efficiency at a given flow speed. In the same format as the C_L , the drag coefficient C_D is given by:

$$C_D = \frac{(D/A_D)}{0.5\rho U^2} \quad (3.5)$$

Where D is the drag force and A_D is the effective area of the aerofoil.

Thrust, T , is the resultant of the lift and drag forces as shown in Figure 2.6. The L/D

ratio, which directly determines the thrust, varies from the root to the tip as the turbine blade is twisted to different degrees at different positions. Based on Equation 3.4 and 3.5, the thrust coefficient C_T , which is an important dimensionless value, can be calculated as:

$$C_T = \frac{T}{0.5\rho AU^2} \quad (3.6)$$

As a means of exploring the behaviour associated with these equations an actuator disk model, which is based on a linear momentum theory, was proposed by Betz. (Betz, 1926). The approach was refined in later by researchers (Manwell et al, 2009) who outlined the following process: A control volume in which the boundaries are the surface of a stream tube is assumed. The nacelle and the tower are ignored in this model. The rotor is simplified to an actuator disk, which means the number of the blades is infinite. Therefore, the total wake caused by the rotation and blockage of the structure is simplified to the one caused by the disk. Figure 2.7 shows an actuator disk operating within a control volume. The following assumptions are then applied:

- Laws relating to incompressible, homogeneous, evenly distributed and steady state fluid is applied.
- There is no frictional drag.
- The thrust is calculated as a one-dimensional constant.
- The static pressure far upstream and downstream of the disk is equal to the undisturbed ambient pressure.

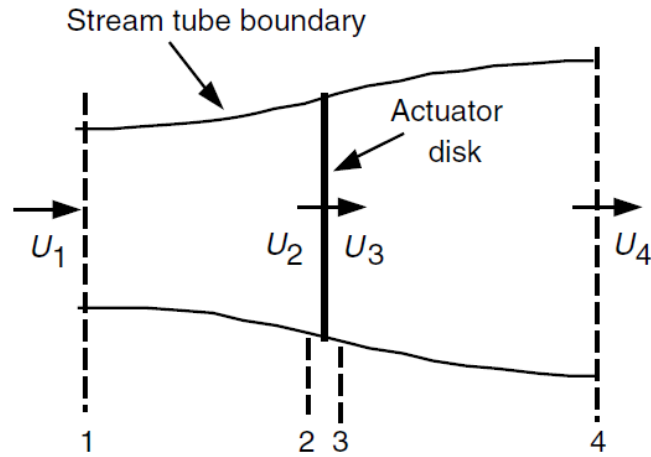


Figure 2.7 Schematic of actuator disk and tidal stream tube. Source: Manwell et al,

2009

Based on the above assumptions, the total thrust on the disk can then be calculated via the conservation of momentum:

$$T = \dot{m}(U_1 - U_4) \quad (3.7)$$

Where \dot{m} is the mass flow rate given by $\dot{m} = (\rho AU)_1 = (\rho AU)_4$ for steady state flow.

The axial induction factor, α , presents the reduction ratio of flow speed downstream of the actuator disk. It is calculated as:

$$\alpha = (U_1 - U_2)/U_1 \quad (3.8)$$

The tip speed ratio (TSR), λ , is ratio of the tangential velocity of the blade tip to the velocity of the flow speed. As the flow direction is not always perpendicular to the rotor plane, it can be used to estimate the working status of the turbine. It is given by:

$$\lambda = \frac{\omega R}{U} \quad (3.9)$$

Where ω is angular velocity and R is the radius of the swept area.

The TSR is an essential parameter to indicate the performance of the TST. An example graph of the relationship between TSR and C_p is shown in Figure 2.8. The maximum power extraction is obtained at the optimal TSR. Note that the TSR is not constant and the uncaptured power is caused by airfoil profile losses, rotor end losses and whirlpool losses. Some factors such as rotor blade number losses are also a potential reason for the dramatic decrease in C_p .

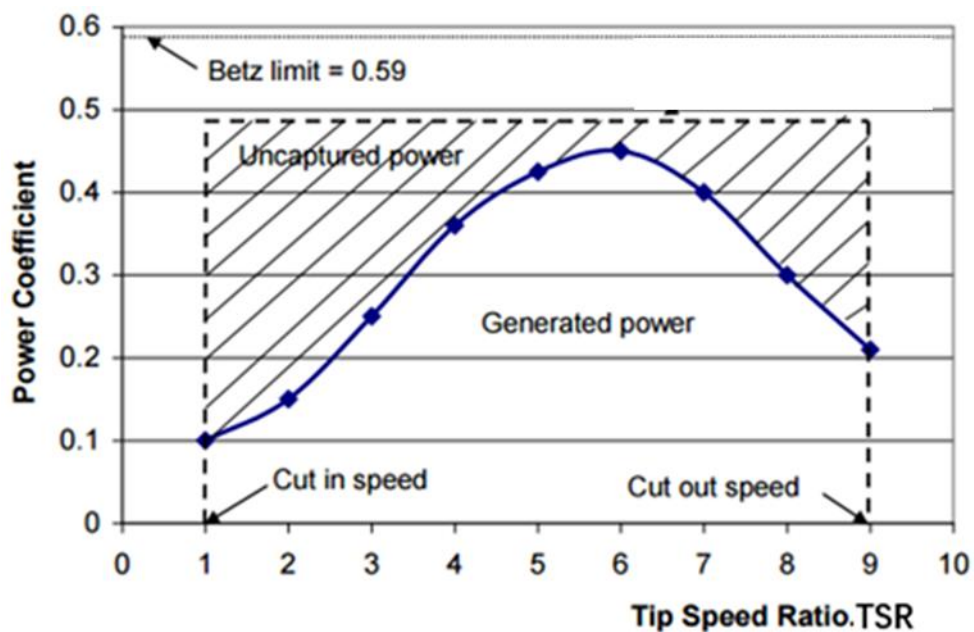


Figure 2.8 $C_p - \lambda$ curves

2.1.5 Yaw and Pitch Control System

The measured flow direction is a very crucial feedback for the yaw system which is directly responsible for the utilization efficiency of the turbine. And, the real-time wind velocity data not only can be synchronized with the rotational speed of the rotor to give the most intuitive state monitoring but also can be a very important input data for the pitch angle control system to provide blade protection during dangerously high wind.

Figure 2.9 shows a very typical wind turbine pitch control system (WTPC).

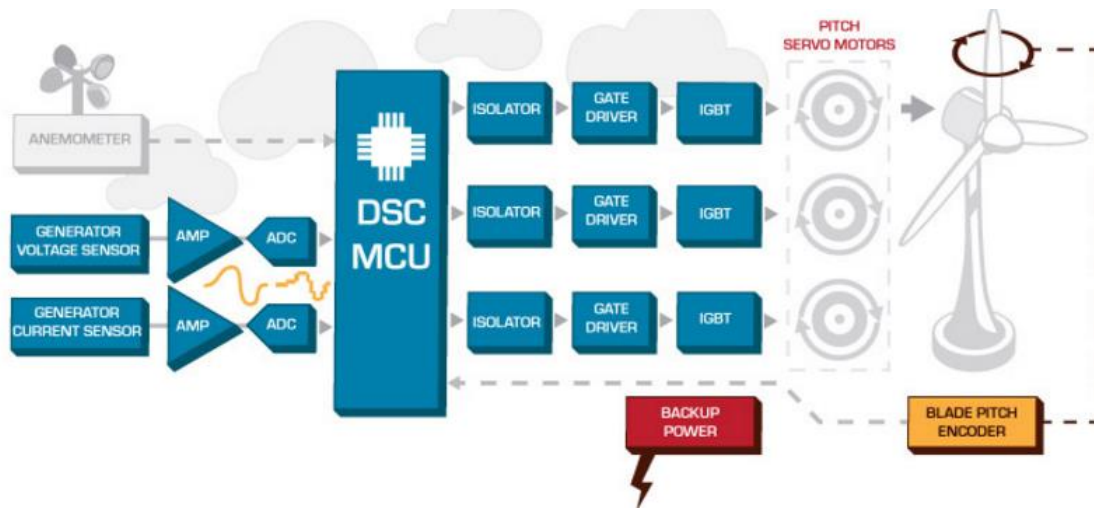


Figure 2.9 Block diagram of the WTPC system. Source: Fleming et al, 2013

When the velocity is lower than the rated velocity, the blade pitch angle will stay at 0° for maximum power output. As the wind speed exceeds the rated value and continues to increase, the controller will accordingly provide the instantaneous instruction for 3 separated pitch control mechanisms (for 3-bladed rotor), which is commonly comprised of rotary encoders, gate drivers, IGBT modules and servo motors (Kabir, 2015). For the wind turbines with different capacities, the specific algorithm will be programmed in advance to the system. It is impossible to find a unified algorithm or analytical solution for this system, as the parameters interact with each other in a complicated manner (Lee, 2013). In most advanced cases, the hybrid solution combined with yaw system and WTPC system was proposed to enable the wind turbine to face more complex and unpredictable wind conditions. By rotating the nacelle, the yaw system not only can steadily capture the highest energy within the rotor swept area but reduce the structure loads of both the turbine itself and downstream turbine, which is simulated by Fleming et al (2013). Figure 2.10 shows the sectional view of a yaw system.

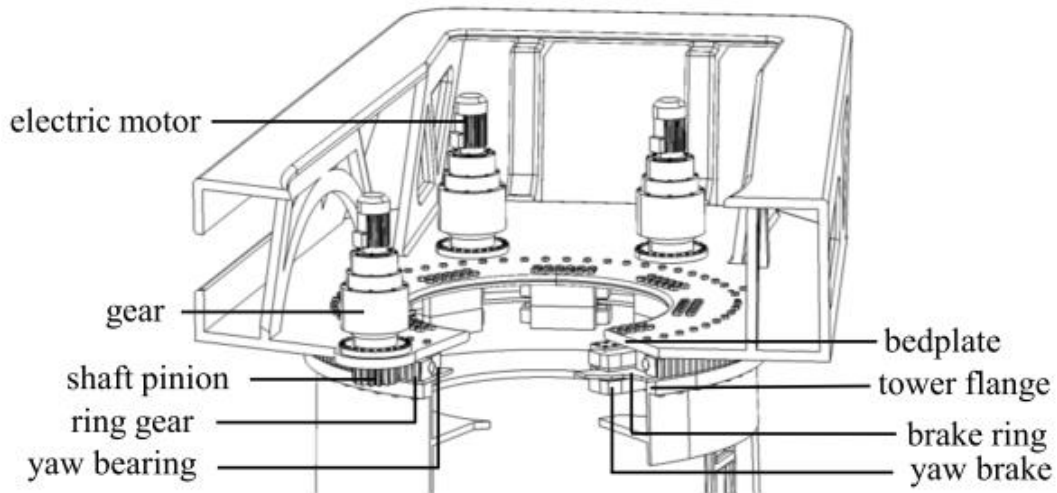


Figure 2.10 Example of a yaw system. Source: Lee et al, 2013

In the existing tidal stream generator, the use of yaw system is relatively conservative. This is partly because the tidal flow direction is relatively fixed, but mainly because some of the components inside this system such as hydraulic actuators (Not shown in the figure) are still in a higher maintenance rate (Hau, 2008), which is unacceptable for an offshore device. Unlike the wind turbine, the yaw system installed in the AR1500 tidal turbine is required to only activate the orientation every six hours for the changing tide and lock the angle during the power generation period (Atlantis Resources, 2015).

2.2 Tidal Steam Turbines Evaluation

Over the past 20 years, there are a number of full-scale prototype and derived small numbers of pre-production TSTs deployed. Some of these projects have been proven to offer the potential for excellent power production. An overview of the existing pre-commercial TST projects can provide much useful information about the structure, design, monitoring technology and problems, which is needed for this current research. Some full-scale tidal stream turbines are selected for evaluation and their specifications and operating environment are listed in the Table 2.1.

Table 2-1 The specifications of pre-commercial tidal turbines. Source: Fraenkel-Wright Ltd, 2012

Models	MCT Seaflow	MCT SeaGen S	AK1000	HS 300	HS 1000	Open Hydro
Rotor Type	Two-bladed Rotor	Twin Two-bladed Rotor	Twin 3-bladed Rotors	3-bladed Rotors	3-bladed Rotors	Open Centre
Rated Power	300 kW	1.2 MW	1 MW	300 kW	1000 kW	1 MW
Location	Lynmouth, Devon	Strangford Lough, Northern Ireland	Orkney, Scotland	Kvalsund, Norway	Orkney, Scotland	Bay of Fundy, Canada
Completion Year	2003	2008	2011	2003	2011	2010
Rotor Diameter(m)	11	16	18	20	21	16
Depth (m)	24 ± 5	25 ± 2	50	50	52	30
Sweep Area (m ²)	95	402	254	314	346	201

2.2.1 Seagen S and SeaFlow

The world's first commercial-scale tidal turbine, the Seagen S was developed by Marine Current Turbines Ltd (MCT). At the time, it was considered to be the most advanced tidal turbine. It had been constructed at Strangford Lough in 2008 and started to generate power only after 14 days installation (Power Technology, 2008). In 2012, the total power generation of 5 gigawatt-hours meant that this grid-connected turbine system can power 1500 homes in the UK (MCT, 2013). The most recent news stated that the Seagen S will be decommissioned before 2017 (BBC, 2016) and the MCT will do the further research for the life-cycle of commercial tidal turbine. Figure 2.11 shows the Seagen S system with its lifted two-bladed tidal turbines. The deployed turbine

configuration intended that the structural design of the two 16 m diameter rotors and the narrow support bar not only provided the minimum 300 m² rotor area needed for economic viability but also reduced the interaction between the blade and tower (Fraenkel 2007).



Figure 2.11 Seagen S tidal turbine located in Strangford Lough; a) shows that rotor blades are lifted for inspection; Right) shows illustration of Seagen S system in operation. Source: MCT, 2008

After one month from its first commissioning, one of the turbines failed to operate due to the wrongly pitched blade. This then suffered an overload caused by the strong flow from the wrong direction (Fraenkel, 2010). Although the design of the main tower with the lift device reduced the labour cost and difficulty of the blade replacement operation, the manufacturing of the new blade resulted in four months downtime (MCT, 2008). Another significant operational maintenance activity was conducted in 2014 and it took 28 days to inspect the main tower and crossbeam that directly holds the two turbines (SWN, 2014). Some other common failures (sensors, cable connections and coolant leakage), which didn't result in too much downtime or extra cost, have been

immediately solved by the engineers on board in scheduled maintenance (MacEnri et al, 2011).

As the older generation of Seagen S, the SeaFlow tidal turbine system (shown in Figure 2.12) consisted of a single rotor with 2.1 m diameter mounted on steel tower structure. In the context of this thesis the SeaFlow tidal turbine system provided much useful experience in TST related areas such as structural design and elements of manufacturing, construction, installation and field testing (Europe Commission, 2005). The adopted structure meant that the system could only operate with the tide in one direction. This was primarily due to the significant influence of the down-flow type of blade-tower interaction.

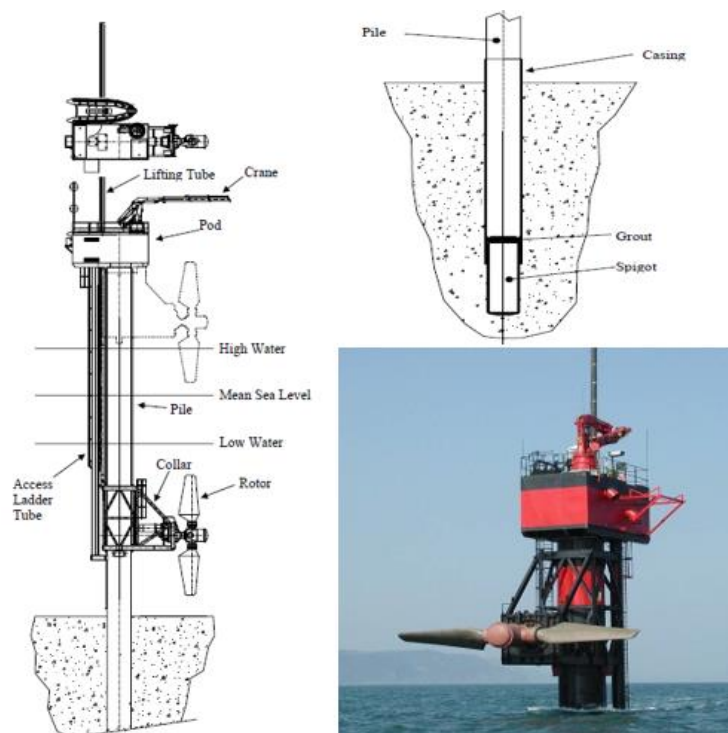


Figure 2.12 General arrangement of the SEAFLOW turbine system off the north coast of Devon Source: European Commission, 2005. Elghali et al, 2007.

Without the yaw control system on the tower, which was introduced in the Seagen S

turbine system that has similar horizontal axis structure, SeaFlow was only suitable for sites located in a channel or river. A study indicated that any variation of the flow direction toward the axis beyond 15 degrees will result in this system becoming non-effective (Robotham 2008).

The final report of the Environmental Monitoring Programme (EMP) for the SeaGen S system was published in 2011 (Keenan et al 2011). This was intended to ensure that this turbine system had no negative impact on the marine mammals and the seabed species. Although a previous report in 2009 provided evidences to prove that no such damage was occurring, the turbine was licenced to only operate in daytime until the completion of the final report (MCT, 2014). Since the turbine became fully operated, its annual power generation is more than 2 gigawatt-hours and there has been no significant failure during this period.

2.2.2 OpenHydro

The development and deployment of the OpenHydro tidal turbine system has earned a good reputation and has been supported by many successful projects. OpenHydro Ltd started to research its Open-Centre technology in 2004 and its first test was conducted in Scotland two years after. The recent contract with the Japanese Ministry of the Environment indicated that it is the first tidal turbine manufacturer break into the Asian tidal energy market. Unlike other tidal turbine energy companies, OpenHydro Ltd did not give any model name for each updated design of the system, although their structure, size and monitoring system are different. Figure 2.13 shows the evolution of the series of the OpenHydro tidal turbines in different projects over time.



Figure 2.13 Evolution of the OpenHydro tidal turbine systems Sources: Energy Insight, 2009.

- (a) The first OpenHydro tidal turbine tested in Orkney Islands has a rotor with 6 metres diameter and 16 blades. The platform was designed as two piles to raise the turbine to do the regular inspection and maintenance.
- (b) In 2009, this system was deployed in the first commercial scale in the Bay of Fundy, Canada. Apart from less blades (12 blades), there was no real observable change in the main part of the turbine. This configuration utilises a central cylinder in the middle of the rotor to fix the blades. This installation was subject to a failure, which occurred after 20 days of operation (Andrew et al, 2012). Due to the unexpectedly strong tidal flows, all the blades were destroyed, and the downtime was almost more than 1 year (Boslet, 2010). This accident revealed two problems: firstly, there is a lack of real-time ocean current velocity monitoring for the whole extracting area and secondly the cylinder in the middle, which connects every blade, did not provide the blades with a certain range of flap-wise deflection and made all the blades share the thrust. In this case the

failures were in part made worse because the OpenHydro system was unable to automatically take measures to prevent the failures. This was mainly due to the rotor blades operating without pitch control.

(c) Figure 2.13 shows a new model of the OpenHydro which was designed in 2012.

This has 10 blades with a more robust hub. The 16 m diameter increased the rated power up to 2 MW.

(d) Although there was no record of any severe failure for this structure, in 2015, the

structure of the turbine was eventually transformed to the one shown in Figure

2.13(d). The hub in the middle has been removed, which allows the tip of the

blade to undergo the flap-wise deflection. The turn-in tip of the blade minimised

the influence of the non-uniformly distributed loads caused by the difference

between the flow velocities in vertical positions. There are two new 2 MW

OpenHydro tidal turbine system which will be installed in the Bay of Fundy

(SWN, 2016).

2.2.3 AK1000 and AR1000

The 18-m diameter and 255 m² extracting area of the AR 1000 and AK1000 tidal turbine systems by Atlantis Resources Corporation means that they were the world's largest tidal turbines in 2010. The company's philosophy of design meant that the device worked in a similar manner to a wind turbine. This allowed the simplifying of its structure and associated details such as the direct drive PMG (needing no gearbox), the rotor-nacelle-tower structure and the use of fixed pitch blades. The reason for this approach was improving the reliability of the system. The first trials for the AK 1000

tidal turbine system were conducted in the waters off the Orkney in 2010. The double rotor configuration and the design of the relatively long chord length meant it was different from other usual tidal turbine systems. Figure 2.14 shows the picture of the assembled AK1000 turbine system.

Although a study by O'Doherty et al (2009) indicated that power generation increased with the use of a contra-rotating turbine, the influence of increased axial thrust is uncertain. In the second month of its operation, one of the blades was broken despite the conditions being within the rated flow velocity. This failure was found to be due to a manufacturing fault according to the later investigations (Elasha, 2014).



Figure 2.14 AK1000 Tidal turbine assembled on the land Source: Jupiter Hydro Inc.,2012

The next generation AR1000 turbine system was introduced in 2011. In fact, the early AR1000 was adapted from the AK1000 tidal turbine by removing one set of the blades. The single rotor and yaw drive means that the AR1000 can provide a good performance even in the slack period. After one year of the operation, AR1000 became the first

one to conduct the full-scaled tidal turbine experiments such drive train testing and accelerated lifecycle testing (Taaffe, 2016). The Figure 2.15 shows the installation of the AR1000 turbine.



Figure 2.15 Installation of the AR1000 tidal turbine Source: Jupiter Hydro Inc., 2012

2.2.4 HS300 and HS1000

ANDRITZ HYDRO Hammerfest developed the HS300 system in 1990s, it was installed as the first gird-connected tidal turbine in Norway in 2004. It was originally designed for 3 years field testing but was used until 2012 with a maintenance in 2009. Although the HS300 is a prototype scale structure the rotor diameter was nearly 20 m, providing a swept area of more than 300 m². This is bigger than many commercial tidal turbines (AHH, 2012). The conventional straight support structure has been changed to the inclined tower. As the main part of the substructure, this inclined tower has been fixed on the seabed by three ballast packages. This design reduces the blade-tower interaction in a certain range due to the larger tip clearance and also reduces the vibration in the flow direction caused by the hydraulic loads on surface of the

substructure. After the successful deployment of the HS300, the HS1000 was first installed in Orkney in 2011 to replace its predecessor. As the pre-commercial version of the HS series, this version has been subsequently deployed as the first turbine in the planned MeyGen Phase 1A tidal array. Figure 2.16 shows the general arrangement drawing for HS 1000 tidal turbine system.



Figure 2.16 Structure of the HS1000 tidal turbine system Source: McEwenet.al.2012

The HS1000 is a typical example of a simplified wind turbine structure both inside and out (McEwen et al,2012). All the components have been integrated into the nacelle as the wind turbine and the cable for transferring the electricity is placed outside the tower. This means that the whole substructure is independent to facilitate the convenience of installation, replacement and decommissioning. Moreover, the load bank is mounted on the bottom of the incline tower to dissipate the electricity for any unexpected failures of cables (SPR Ltd, 2010).

2.3 Numerical and Experimental Studies of TST

CFD is based on the application of the Navier-Stokes equations. It is a powerful tool that is used for visualising the flow motion and assessing its influence on objects by

using applied mathematics, physics within the associated software (Shah et al, 2013). This cost-effective and time-saving method has been used to provide reliable numerical analysis for TST performance in recent years. It uses information of a full-scaled or scaled TST to create a 3D mathematical model on a grid. Various flow conditions are then applied on the model to investigate the specific problems. The results of CFD modelling conducted by Cardiff Marine Energy Research Group (CMERG) are presented and reviewed in the following sections to illustrate the nature and benefits of this approach. The main aspects of CFD were presented in work published by Robinson and Byrne (2008) which summarised the basic considerations for modelling a TST, as shown in Figure 2.17.

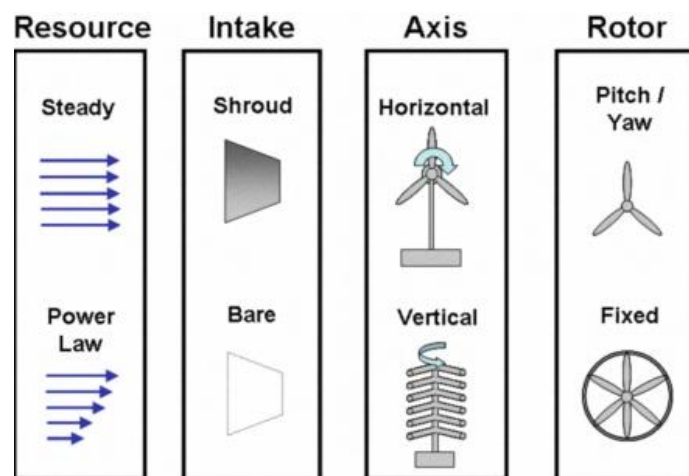


Figure 2.17 Aspects to modelling a TST. Source: Robinson and Byrne, 2008

Apart from the uniform flow condition and profiled flow, the blockage conditions are also studied as a very important scenario. The blockage conditions are inevitable in practice and classified as two main categories:

1. the blockage from another TST system upstream.

2. the blockage from the tower when the flow direction is reversed.

It was recognised that a TST will experience more interferences in wall bounded flow than in free-stream conditions (Glauert, 1933). However, the OpenHydro TST which has a fixed blade and shrouded structure is still competitive in the current tidal energy market.

The comparisons between different pitch angle are often used to study the performance of the turbine operated in various flow and blockage conditions.

A consideration of the structural-based dynamic behaviour of a TST blade is presented as the theoretical basis of the experiments in following chapters. Other mathematical modelling work related to the blade behaviour and turbine performance is also summarised. This is then used to consider the influence of the Blade-Tower (B-T) interaction on HATT performance.

2.3.1 Scaled Flume and Wind Tunnel Testing for Scaled TST

While the field testing of a full-scaled TST at a specific location can provide valuable information for its design iteration, the research of improving the turbine performance can benefit from being undertaken within a relatively ideal operating environment. This is because of the many design parameters are involved. In the open channel, the flow conditions are affected by channel shape, volume, gradient and the friction created between the moving water and the elements such as rocks on the bottom. The common application of testing in a water flume is used to not only validate the CFD results but also to transfer the proposed technique into the full-scaled device. Figure 2.18 shows

the general setup for the water flume test conducted by CMERG researchers (Allmark 2017) at Liverpool university. The water flume was configured and controlled to provide plug flow conditions (constant flow with water depth) and an average axial flow velocity of 0.94 ms^{-1} (Allmark et al, 2013). A scaled HATT was supported from above, being suspended from a horizontal tower. In operation, the cables were tied together with the support structure and connected to the controller and the PC. The support structure was instrumented with a force block measuring the total thrust loading.

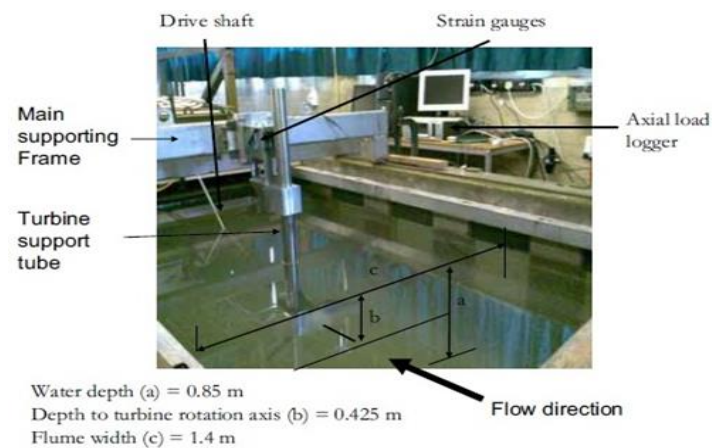


Figure 2.18 General water flume test arrangement. Source: Allmark, 2017

The $1/20^{\text{th}}$ scaled turbine used in test was designed by CMERG and the group have developed three generations of small-scale TST models in recent years for validating the information from mathematical modelling activities. The TST model has three 0.5m- diameter blades and each blade pitch angle was adjustable. More details can be found in a related paper (Mason-Jones, 2010). Figure 2.19 shows the configuration of the $1/20^{\text{th}}$ scaled TST.

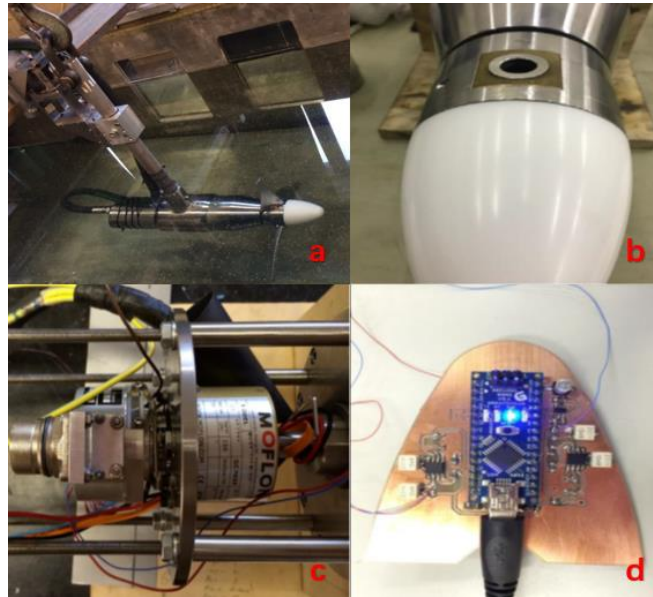


Figure 2.19 Configurations of the scaled TST model. Source: Allmark, 2017

In this configuration, a) shows the scaled TST in the water flume after installation; b) shows the adjustable circular hole on the blade housing to install the blade; c) shows the USB slip ring mounted at back of turbine for data communication and instrumentation power; d) is the nose cone circuitry installed inside the hub for signal conditioning and data acquisition.

According to the CFD modelling, the optimum blade pitch angle had been determined to be 6° . In this test, one of the blades was deliberately adjusted to a pitch angle of 15° to simulate a general blade fault. The comparisons of both the levels of generated power and axial thrust between the optimal and offset group can introduce unbalanced blade contributions. However, based on the actual observation, two potential influencing factors must be considered:

1. As the vibration of the entire structure can be visibly observed during the test, the accuracy of the data from force block was inevitably affected by the vibration

although the obtained axial thrust signal showed that the faulty blade can be detected by the spectrograms analysis.

2. Based on above, it is uncertain whether the influence of the blade pitch angle is structural-based or hydrodynamic-based for this case due to its scaled size. The total thrust signal in the real TSTs may not have enough sensitivity for the detection of small pitch angle offset or the early effect arising due to damaged blades. Actual information about the vibration and/or thrust analysis of the full-scaled TST is very limited in the public domain, which means this uncertainty cannot currently be considered by the comparison between the scaled and full-size TST.
3. The configuration of the setup led to a certain lack of synchronisation of the data captured from differing sources. This limited the comprehensive understanding of the influence of the wrongly pitched blade on the turbine characteristics.

It should be noted that flume-based testing is time consuming and expensive. There would be considerable benefit to be gained by transferring the aims of these tests to a wind tunnel environment which would allow for lower cost, quicker and easier experimentation.

2.3.2 Structural-based Analysis of TST

A small model of a 3-bladed turbine is shown in Figure 2.20. This was used for demonstrating the deformation of the TST's blade. The components u , v , w and ϕ respectively represent the longitudinal, edge-wise, flap-wise deflections of the blade

and torsional direction. For the faulty blade, these components will be different from those associated with the optimal or healthy blade due to the changing properties.

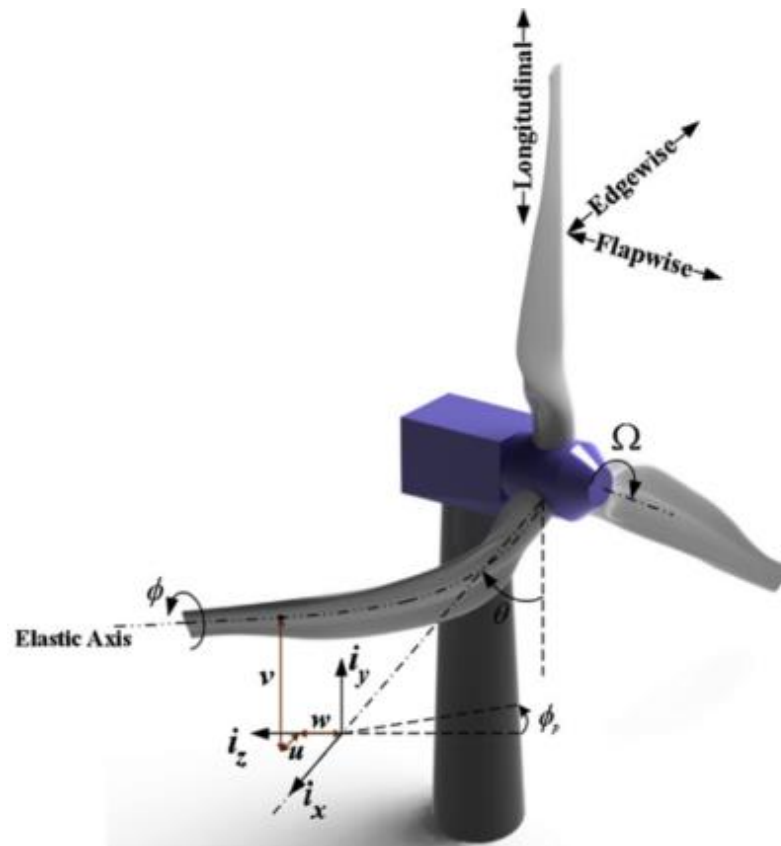


Figure 2.20 Schematic view of blade deformation. Source: Rezaei et al, 2015

In the same way as has been considered for a wind turbine blade, a blade of a TST can be simplified to a cantilevered beam AB for static analysis as shown in Figure 2.21 (Tartibu and Kilfoil, 2012 and Hansen et al, 2006). The end A of the beam is fixed to the wall as the blade is ideally connected to the hub. The flow pressure is considered as being a uniformly distributed hydrodynamic load (UDHL) q ; The symbols d and θ respectively means the tip deflection and the angle of rotation at end B.

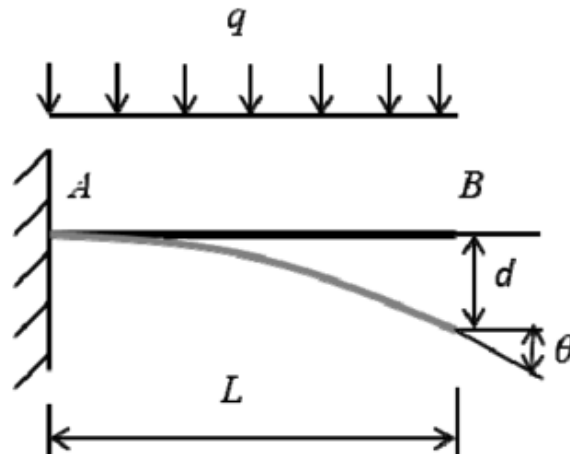


Figure 2.21 Tip deflection and cantilever beam with UDHL. Source: Tartibu and Kilfoil, 2012

The relationship between tip deflection d and cantilever beam can be given by:

$$d = \frac{qL^4}{8EI} \quad (3.10)$$

And, the angle of rotation at B can be calculated by:

$$\theta = \frac{qL^3}{6EI} \quad (3.11)$$

Where EI is bending stiffness and L is the length of cantilever. With the reduction of the blade stiffness, the tip deflection d increases. After derivation, the relationship between tip deflection d and the angle of rotation θ in this case can be expressed as:

$$d = \frac{3}{4} \theta L \quad (3.12)$$

For analysing the entire TST system, the tower and the main shaft can be simplified as a cantilevered beam with different properties of the material. With the UDHL, two scenarios are demonstrated in Figure 2.22. q_0 is the uniformly distributed flow pressure.

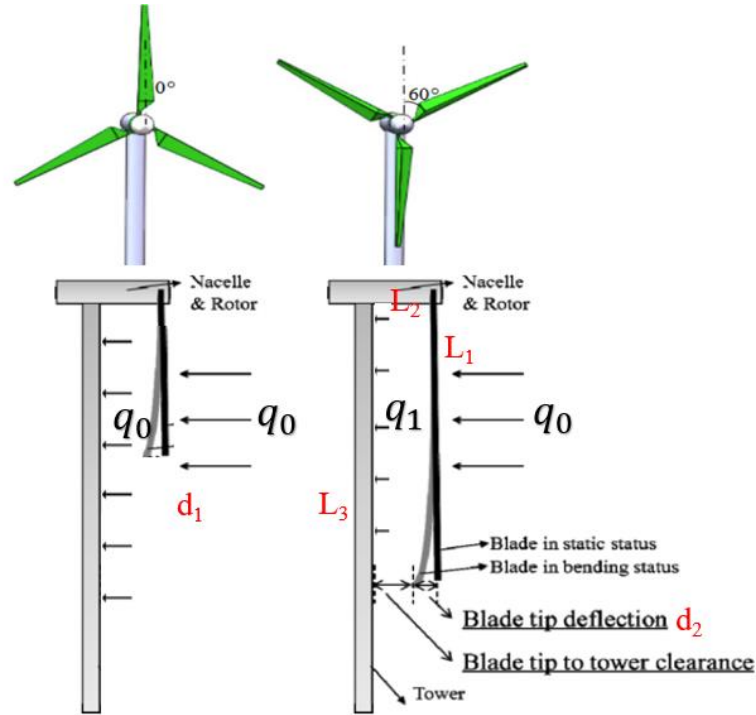


Figure 2.22 Flap-wise tip deflection of the turbine blade in different azimuth positions

Without the blade in front, the load applied on the tower or on the blade should be constant. Assuming that: L_1 is the blade length, L_2 is the length of the shaft between the blade and tower, L_3 is the height of the tower. The d_1 can be expressed as:

$$d = \frac{3}{4} \theta L \quad (3.13)$$

With the assumption that q_1 on the tower remains to be the steady uniform loads, the resultant tip deflection d_2 is mainly dependant on the difference between q_1 and q_0 . Therefore, for a large wind turbine or TST, the tower pressure distribution within the swept area is very important for analysing the blade deflection and the vibration of the entire structure (Zhou, 2012). In real life however, the tower of the TST will have much higher stiffness than the blade due to larger size and material properties of the former. Therefore, the shaft and blade are more sensitive to deformation or vibration.

This simplification of the TST blade is useful for understanding the small-scale

experiment which is not related with the blade profile. However, the actual TST's blade has multiple aerofoil sections, chord lengths and angles of twist, which means the loads on the blade are complicated. As an illustration of this the blade of TST can be considered as three regions according to the associated hydrodynamic and structural function as shown in Figure 2.23. The resistance of the all sections of the blade under the extreme loading during operation must be considered in blade design (Ahlstrom, 2006).

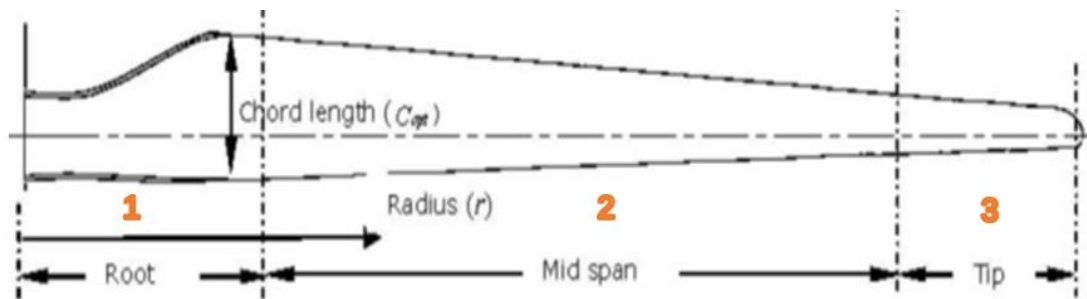


Figure 2.23 A typical blade region classification.

Section 1: the blade root is the transition part between the root end and the first aerofoil profile. Although this part has the lowest relative flow velocity due to the small rotor radius compared to the other two, it carries the highest hydrodynamic loads. This is also the main reason why the aerofoil profiles close to the root are excessively thick. In addition, the hydrodynamic efficiency in in this region is relative low;

Section 2: the mid span is the main part that is used for extracting the energy from the tidal stream. As such the lift to drag ratio (L/D) for layer in this area is maximised;

Section 33; the blade tip is designed to reduce noise and cavitation that can occur due to it having the highest TSR along the blade.

2.3.3 Flow Profile and ADCP Measurement Techniques

A report (Fraenkel 2011) showed that 75% tidal power is in the top 50% of the sea and a higher velocity shear is present for the bottom 25% of the sea. As shown in Figure 2.24, the flow profile close to the seabed has a much higher vertical shear than those located in the upper 50% of the water column. For the practical operation of the TST, the rotor blades operate with the depth-wise velocity profiles instead of UDHL. This means that the load on each blade varies with its position within each rotation. If the flow profile changes significantly within the swept area, the turbine performance would be affected (Fung, 2014). Two of the main reasons for a flow profile change within the swept area of the TST are;

- 1) the operating depth of the TST will vary with the time due to changing sea levels during tidal movement.
- 2) the transient turbulence plays a crucial role on changing the flow direction and speed in both horizontal and vertical directions.

However, once again it must be stated that much of the data acquired from full-scaled TST project sites is typically limited to leading companies (Mason-Jones et al, 2011).

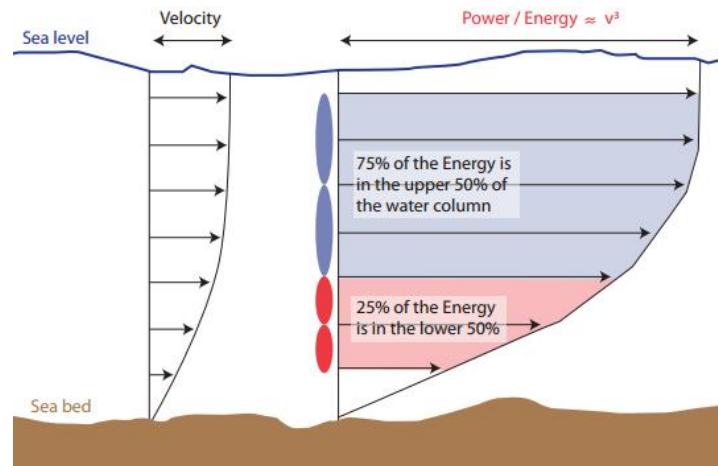


Figure 2.24 Velocity profile and power distribution through water column. Source:

Fraenkel, 2011

In the early stage of the development of the TST, depth-averaged or simplified velocity profiles were used when modelling the flow condition (Lewis et al, 2016). A $1/7^{\text{th}}$ power law is typically accepted by the wind industry and emerging tidal industry and expressed as:

$$\frac{U}{U_r} = \left(\frac{Z}{Z_r}\right)^\alpha \quad (3.14)$$

Where U is the flow speed at the height Z , U_r is the known speed at the height Z_r , and exponent α is empirically derived as $1/7$, or 0.143 .

In the practical tidal turbine applications, the Acoustic Doppler Current Profiler (ADCP) is the most commonly used device to measure the current velocities over a depth range. Although its primary usage is for oceanography (Emery et al, 2001), ADCP is also used to continuously measure the flow profile after improving its processing methods. Similar to SONAR, the ADCP approach uses a Doppler shift to remotely but accurately measure the flow profile. Figure 2.25 shows the locations

typical for the ADCP in operation.

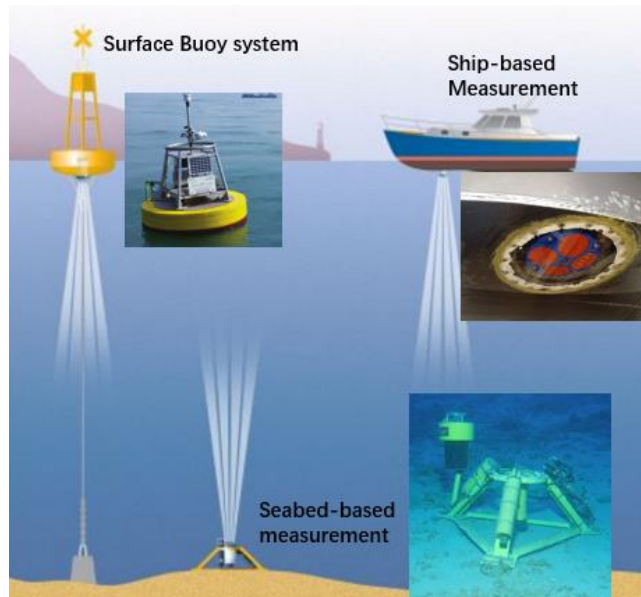


Figure 2.25 Schematic diagram of the ADCPs in operation

A typical case examining the flow profile using an ADCP survey was conducted (Epler et al (2010) and the specifications of the shipboard ADCP deployed are shown in Table 2.2. The ADCP is powered by the ship and the error caused by the movement of the ship was eliminated by a GPS navigation system.

Table 2-2 Shipboard ADCP configuration. Source: Epler et al, 2010

Teledyne RDI Workhorse Monitor	
Acoustic Frequency	307.2 kHz
Time per Ping	0.5 sec
Time between Pings	3 - 4 sec
Vertical Bin Size	1.0 m
Pings / Ensemble	1
Transducer Depth	1.18 m
Blanking Distance	2.0 m

The estimated average flow profile is shown as blue curve in Figure 2.26. Each grey point represents the speed data at a corresponding depth. The red box shows a 5m vertical average region. The averaged velocity close to the seabed is seen to fluctuate

and will thus not be a good source of reference data.

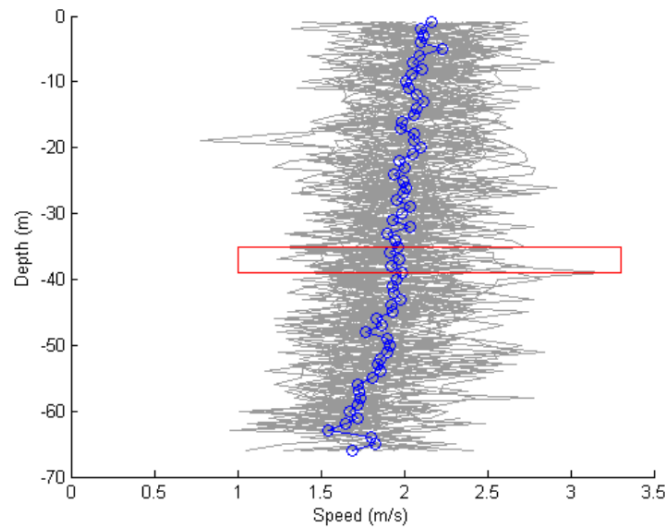


Figure 2.26 Estimated velocity profile in vertical direction. Source: Epler et al (2010)

Although ADCP is reliable for ensuring that the current at the selected site is strong enough for power generation before project installation, the performance of this instrument for the long-term real-time monitoring work still has much room for improvement. This can be observed in relation to the blade failure of the Open Hydro tidal turbine which occurred in the US in 2009 (Andrew et al, 2012). This and other similar reported failures (Liu et al 2012) reflected that there was a certain technical defect in the system. This could be associated with both the rotor brake alarm and water flow monitoring. This research suggested that the presence of random strong ocean turbulence approaching the rotor blade cannot be precisely located or found using ADCP. The unexpected early blade fatigue which repeatedly occurred in regard to the AK1000 HATT, which was widely reported (BBC 2015), was attributed to the lack of the experimental data for long-term field monitoring of blade loads (Milne et al, 2015). It was also considered that there was a large discrepancy between the actual blade load

distribution and the measured flow profile.

A further limitation on ADCP deployment is related to the energy supply problem for the floating ADCP. This and the influence of the harsh marine environment on any seabed-based ADCP restricts the capability of a deployed device to obtain reliable data of flow profile in the long term. Figure 2.27 shows the marine growth on the seabed-based ADCP after two years of operation.



Figure 2.27 Changes of seabed-based ADCP after two years of operation. Source:

Houde, 2012

Based upon the consideration of the above issues and the advantages and disadvantages of ADCP given by the Woods Hole Oceanographic Institute (WHOI, 2009), the limitations of seabed-mounted ADCP for condition monitoring functions applied to TST can be summarised as:

1. Due to its working principle, the performance of ADCP can be affected by the reduction in particle densities.
2. High frequency single repeats can consume huge amounts of power, which increases both the transmission load and cost.

3. The regular and frequent maintenance is not cost-effective and achievable due to the deep-water location associated with TST deployment.
4. The long-term performance or measurement accuracy cannot be guaranteed.

Taking this assessment forward it is clear that an alternative to ADCP would be very beneficial to the monitoring and management of deployed TST devices.

2.3.4 Blade-Tower Interaction

Blade-Tower (B-T) interactions have been previously considered in respect to the operation of wind turbines. There are two types of B-T interactions, depending on the flow direction (Hansen et al, 2006). For application to a tidal turbine, these could be called downstream and upstream. The B-T interactions are caused by the complex flows between the blade and tower which can result in the unstable and unexpected aerodynamic performance of the turbine. Therefore, extensive work has been conducted to predict aerodynamic performance: Duque et al. were the first to perform the CFD modelling based calculation of a downwind wind turbine (Duque et al. 1999). Further work (Back et al 2001) indicated that B-T interactions would affect fatigue loads, particularly at relatively low wind speeds. To date most reported studies focus on the downwind interactions on the wind turbine as the influence of the blocked tower on the rotational speed and thrust is significant compared to the upwind turbine (Chattot, 2006). As shown in Figure 2.28 the downwind B-T interactions are often defined in terms of a tower shadowing effect (Gan et al, 2017).

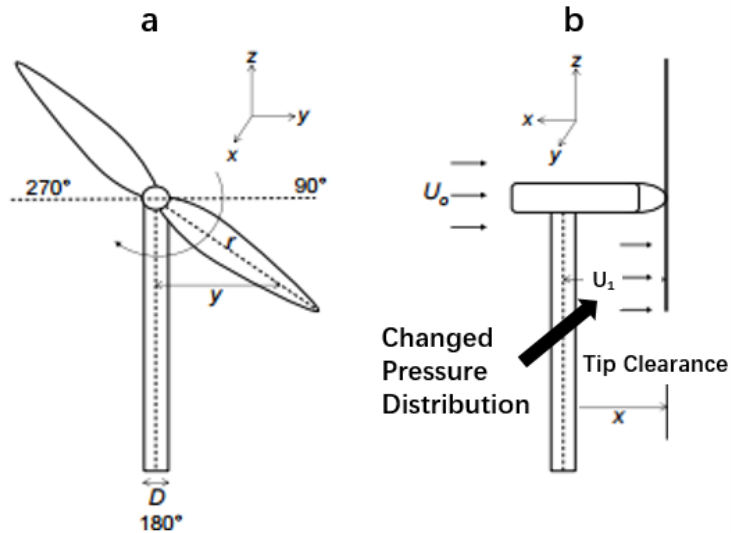


Figure 2.28 Schematic diagram of downwind B-T interactions. Source: Gan et al,

2017

Figure 2.28(a) shows that there are no tower shadowing effects when the main part of the blade does not overlap the tower, from the axial angle of observation. Figure 2.28(b) shows the suddenly changed pressure distribution associated with the blade being at the 180° azimuth angle. Without the consideration of the tower deflection or vibration, the pressure on the tower surface is assumed to be constant during the operation. Modelling conducted by CMERG researchers (Doherty et al 2009) indicated that the downstream flow condition results in the simulated TST experiencing peaks of the axial bending moment 10 times greater than the average moment for the upstream arrangement. Tip clearance is the distance between the blade tip and the tower surface and it can show the degree of the blade deflection under different conditions. In addition, it can be used as an indicator to show if the blade is deflected under a certain wind condition.

The influence of the downwind or downstream B-T interactions are not only on the

turbine performance but the structural stability. Proof of this has been provided with the comparisons of the performance and unsteady loads between upwind and downwind WTs (Frau et al 2015).

Figure 2.29 shows the fluctuation of the power coefficient caused by upwind and downwind B-T interactions.

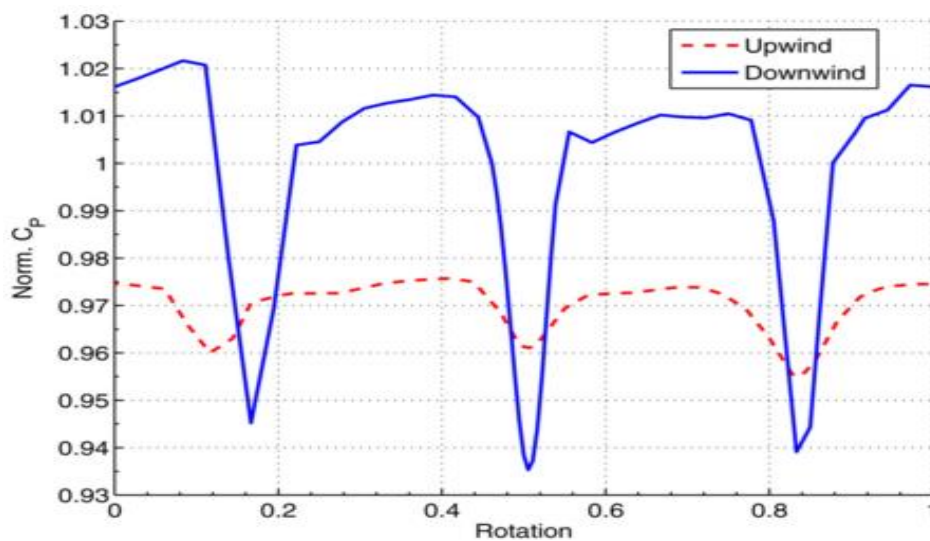


Figure 2.29 Normalized power coefficient over one revolution. Source: Frau et al,

2015

The power coefficient drops arising in each rotation for each blade of the downwind turbine can be observed in Figure 2.29. This behaviour can be related to turbine operation as depicted by the illustrations of Figure 2.28. Although this drop can be observed to a lesser degree in the upwind turbine it cannot be ignored. With the assumption that there is no deflection of the tower, the flow pressure applied on the surface of the blade should not be affected by the tower behind the blade. The comparison of flap-wise blade moment, shown in Figure 2.30, can be used to explain its direct consequences. Specifically, the variation of the flap-wise blade deflection

results in an unsteady angle of attack, which is closely related with power extraction. In addition, the thrust drop of the upwind turbine means that the blade continues to vibrate in the flap-wise direction. However, in the case of the upwind turbine, the blade bending moment remains low within a short period after the tower passage and then rise slowly until the next passage. This phenomenon and the associated turbine behaviour has been explored (Graham et al 2001) to show that, with the increase in deployed wind turbine diameters over time, the loss performance due to upwind interactions have become increasing worthy of consideration.

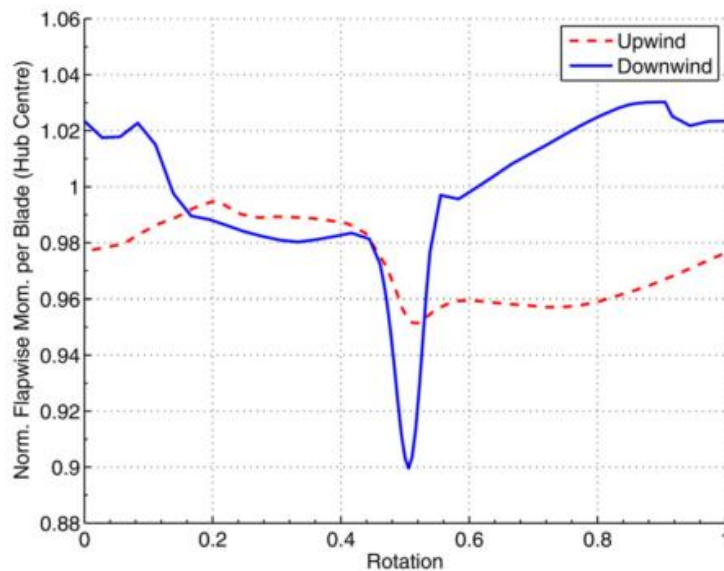


Figure 2.30 Evolution of one blade flap-wise moment over one rotor revolution.

Source: Frau et al, 2015

A nonlinear vortex correction method (NVCM) has been developed (Kim et al 2010) and used to perform a numerical study of a two-bladed wind turbine with various tower radius operated in different flow conditions. Figure 2.31 shows the wake collisions of the simulated wind turbine. Each rotation is divided in to 60 steps and each step is 6°.

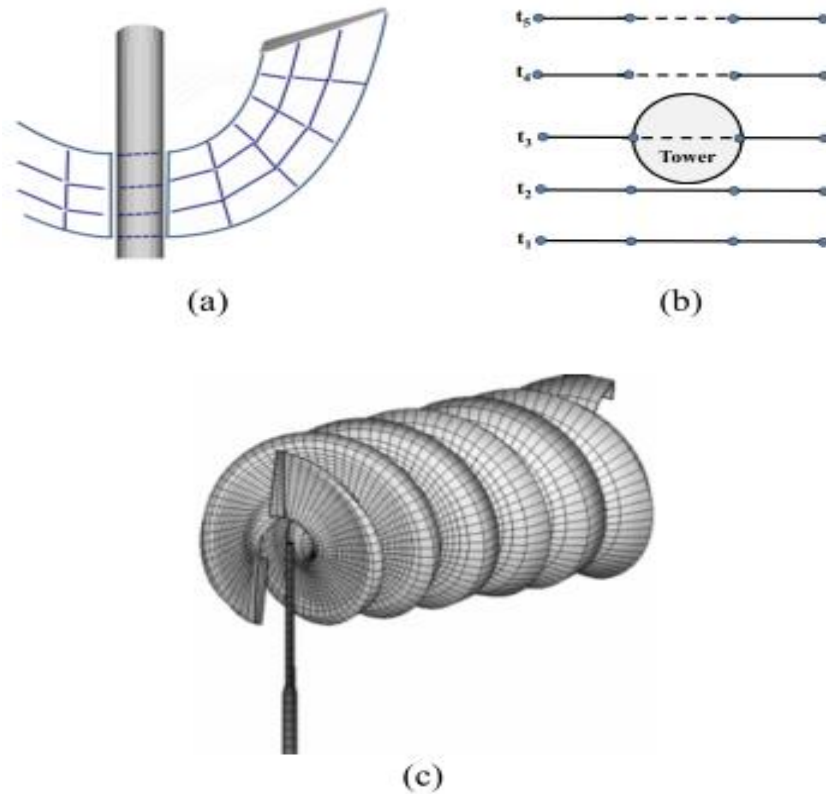


Figure 2.31 Simulated vortex lattices and wake panels. Source: Kim et al, 2011

Figure 2.31(a) and (b) respectively show the front view and top view of wake collision with tower. Figure 2.31(c) shows the whole set of wakes generated by the blade rotation. The results indicate that the difference of shaft torque between the configuration with and without the tower is not significant under steady uniform wind condition. This is because the relatively small chord width of the blade (compared to the tower radius) makes the B-T interactions occur in an instant and represent a very small portion of the averaging value. Figure 2.32 shows the normal force variation in two positions of the blade with different operating conditions. R is the blade radius and r is the distance from the blade root.

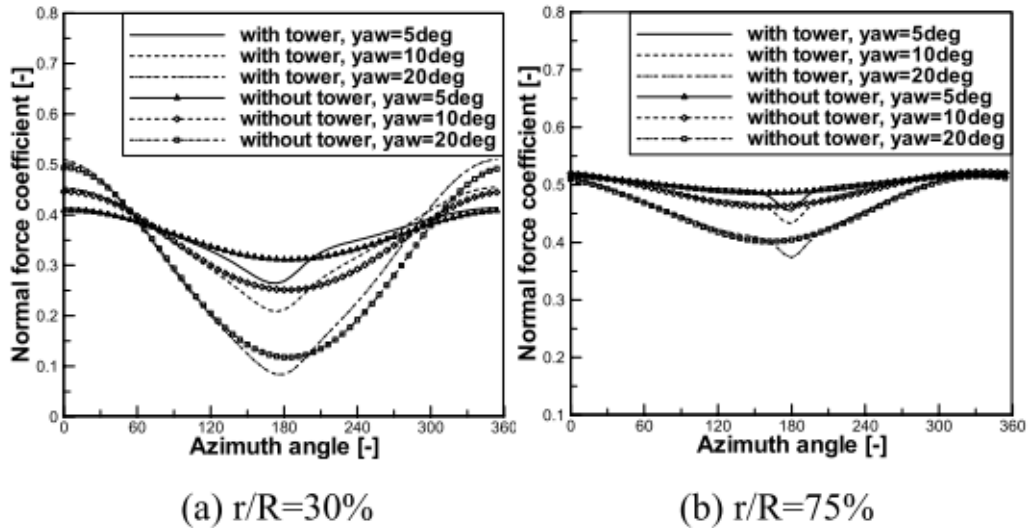


Figure 2.32 Normal force versus azimuth angle in various yaw errors at 5 m/s. Source:

Kim et al, 2011

The blade used in this modelling is from an NREL Phase VI turbine (Zahle et al, 2009), in which the chord length and r/R are inversely proportional as is normal for a wind turbine blade. Without the tower, the fluctuation caused by the yaw error at r/R is larger than that at r/R due to the larger chord length. With the tower, it is found that there is a lower than normal force caused by B-T interaction for each group. However, this change is difficult to quantify with the increasing yaw error. In addition, the pressure on the surface of the tower is hard to predict even for constant wind speeds due to yaw error.

Another research group (Wang et al 2012) performed a simulation to investigate the pressure variation on the tower during the blade passage. Without the yaw error, the obvious cyclic pressure drop exists within the blade swept area. For example, when the turbine operates in a 5ms^{-1} average wind speed, the pressure at the parts close to the middle of the blade can drop below zero. The comparisons are presented in Figure 2.33.

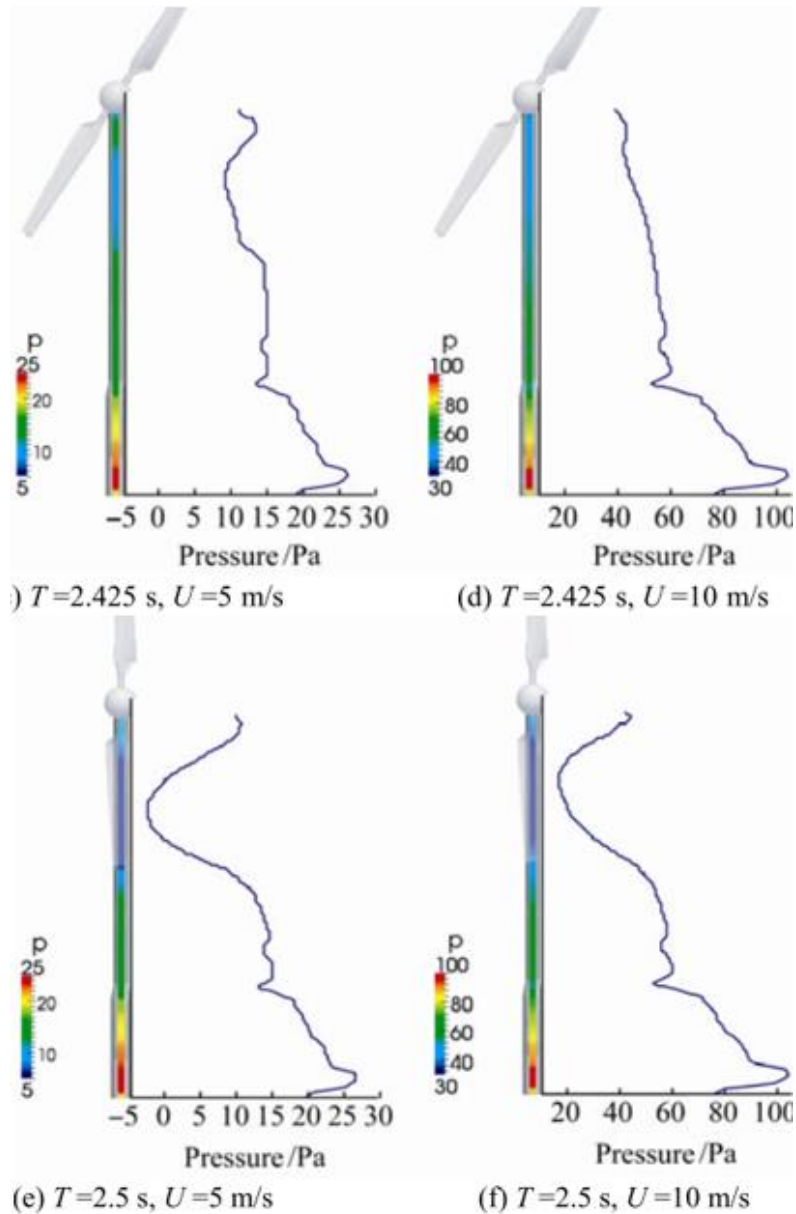


Figure 2.33 Tower pressure distribution for 5 and 10 m/s wind speed. Source: Wang et al, 2012.

Based on the results in Figure 2.33, it can be observed that the geometry (or condition) of the turbine blade plays a crucial role in affecting the pressure distribution on the tower. It is interesting at this point to speculate whether the inverse relationship exists; can the pressure distribution be a source of information in regard to blade condition? This was not considered in the reported research but it may be seen that the failures of

TST blade which are related to changes of geometry can be detected by comparing the historical pressure distribution from reference blade with current blade condition.

Other research investigated how the surface roughness can be seen to be another factor for the wake after the blade. Figure 2.34 shows the photos of Race Rock tidal turbine and the prototype TST of the Verdant Power Company after deployment.



Figure 2.34 Examples of the faulty tidal turbine system. Sources: Elasha et al, 2014 and Zhou et al, 2016.

The build-up of micro-algae on the turbine blades, shown in Figure 2.34 (a), changes the surface roughness. This lead to the loss performance of the turbine which could be related to this degrading in surface conditions. This problem was not found until a few months of reduction in the power generation. It is of great interest to note that, although the system was only a prototype and thus its performance could not be anticipated, the broken blade tip in Figure 2.34 (b) was not detected at first as there was no significant power reduction for this case.

The question that arises here is could there have been a more effective monitoring approach. Since this would depend upon real-time monitoring of the blade status it is

interesting to speculate whether the B-T interactions could be used a breakthrough for this. Due to the harsh and complicated marine environment, there are no reported physical experiments that investigate such phenomena on TST in detail.

2.4 Experience in Blade Health Monitoring (BHM) for Wind Turbine

As the technology applied to TST can be said to be in its infancy, the development and research of the corresponding CM systems can potentially provide much guidance and information on the operation of a TST which in turn can be used for the design iteration of the turbine (Allmark, 2016). Much of the technology developed and applied to support the evolution of a wind turbine and its associated CMs can be directly transferred to tidal turbines. However, as mentioned in Chapter 1, the characteristics of the tidal turbine blade are very different to that of wind turbine in terms of material, size, geometry and accessibility due to the harsh operating environments. Given that the operation and maintenance (O&M) cost of the TST blade is higher than that of WT blade, any unscheduled or reactive maintenance should be avoided as much as possible. It is however helpful at this point to consider a summary of the state-of-art monitoring techniques for WT's blades. This is necessary to establish an ideal structural health monitoring (SHM) system for a TST blade.

One survey (Ribrant and Bertling, 2007) suggests that rotor blades contribute 13.7% of reported wind turbine failures from 1997 to 2005, ahead of gearbox failures (9.8%). According to the information from a second report (Campbell, 2015), there are some 3,800 out of 700,000 WTs in operation that reportedly failed due to the rotor blades in 2015 and the blade failures are primary cause (40%) of insurance claims in the

American onshore wind market. Although wind power has been commercialized for a long time they still fail and the economic losses and downtime caused by the blade failures in particular cannot be ignored. The most effective approach is to deploy a BHM system to secure the successful wind power generation (Yang et al, 2017). There are three issues needs to be considered for establishing the ideal BHM system:

1. The ability to identify the changes or detecting incipient faults on the blade is critical for a specific BHM system. If the incipient faults could be detected earlier and dealt with before they become catastrophic failures, many unnecessary scheduled or unscheduled maintenance can be reduced (Kabir et al, 2015).
2. The trend in wind turbines is for their blades to become larger, longer and heavier over the recent decades. The feasibility of applying the previous generation of BHM systems to the up-to-date WT system is uncertain. In addition, the lighter and stronger requirements for fiberglass composite material also poses a greater challenge for the compatibility of the existing BHM system (Feng et al, 2010).
3. As the BHM system provides permanent protection for the turbine blade, a cost-effective monitoring system is needed with the considerations of the capital cost, operational cost and reliability (Carroll et al, 2016).

Within the literature, three major failures modes of WT blade have been summarised by Yang (2013) as:

- 1) the failure of adhesive joints

- 2) the cleavage (pulling apart of the composite fibers) of the load carrying laminates and
- 3) the damage in laminate involving fiber breakage.

For detecting these failures, many non-destructive testing (NDT) techniques with different sensors, operational principles and installation locations have been developed and deployed.

In order to place into context, the approaches develop later in this thesis the capabilities, benefits and drawbacks of each BHM system are reviewed and the possibility and limitations of transferring these techniques to TSTs is also discussed in the following.

2.4.1 Acoustic Emission (AE) Monitoring

AE technology refers methods deployed to detect the blade changes such as cracking, irreversible deformation, delamination and collision. This is achieved by analyzing the transient elastic waves produced by a sudden redistribution of stress at specific location (Balageas, 2006). Unlike most other NDT techniques, AE only receives the acoustic signal released by the object if the changes are adequate larger enough to trigger acoustic emissions. Based on its working principle, the reliability of AE monitoring is prone to be affected by background noise.

Another important attribute of AE technology is to distinguish between the developing and resident defects to ensure that only the former will be highlighted (Joosse et al, 2002). Other researchers (Bouzid et al 2014) conducted a field test by using the wireless AE units on a 300W wind turbine installed at Newcastle University

and localized the fault by extracting the features from aliased AE signals. Figure 2.35 shows the configuration of the models.

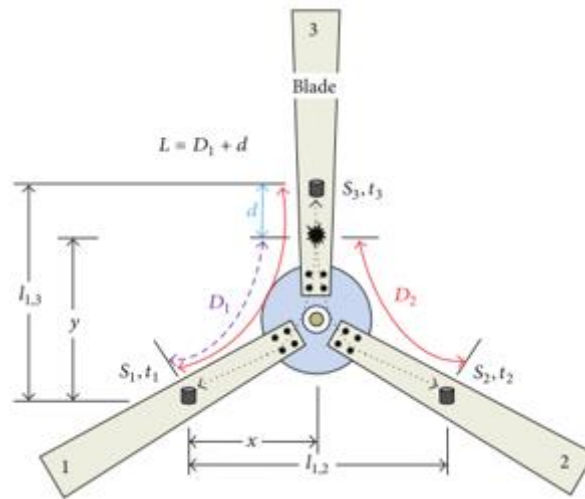


Figure 2.35 Proposed configuration of acoustic wireless units. Source: Bouzid et al, 2002

In this configuration, the AE signals generated propagated in constrained paths along each of the blades and the signal captured from the rotating blades was sent to the remote-control unit through a wireless medium. With the increase in size of the wind turbine blades, a considerable number of AE sensors deployed along the blade is required to achieve full blade coverage (Ruan et al, 2014).

2.4.2 Infrared Thermography (IRT)

IRT, also called thermal imaging, involves visualizing the surface temperature of the object by representing it as an image. Since all objects emit the electromagnetic radiation that is related to its temperature, any faults on the blade caused by the degeneration and cracks can potentially be associated with a temperature change (Yang et al, 2013). The IR-camera is the only device needed for this method and is often

located on the bottom of the turbine for inspecting all the three rotating blades. Therefore, the blade defects near the camera are particularly easy to detect (Hameeda et al, 2007). Figure 2.36 shows an example of the thermal photographs of the WT blades.

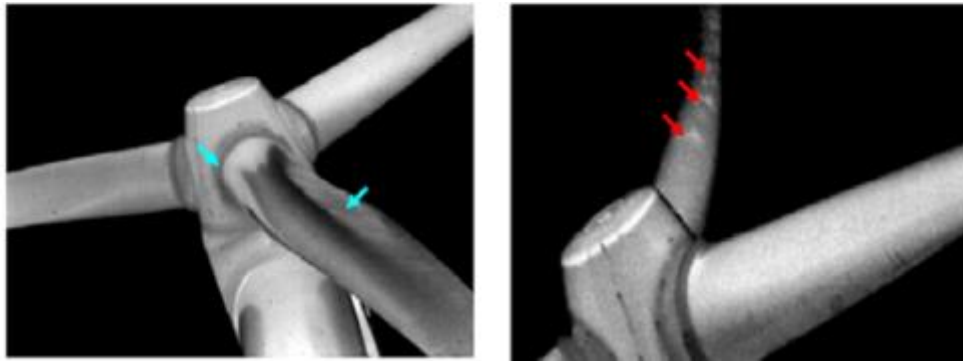


Figure 2.36 Thermal image of the rotating blades. Source: Meinschmidt, 2006.

The bright areas in left photograph, which are warmer than the dark areas, indicate the higher temperature caused by the extra mechanical loading (blue arrows). The bright areas in right photograph shows the hot spots due to the friction of micro cracks (Meinschmidt, 2006). However, a feasibility study (Bodil et al, 2001) suggested that IRT is not capable of detecting the early fault as this associated temperature change develops slowly. In addition, the cooling capacity of the seawater will also affect the imaging process.

2.4.3 Optical-Based Strain Measurements

It has been shown that optical fiber sensors are capable of measuring temperatures and/or strains at thousands of points along a single fiber (Bao and Chen, 2012). As such a turbine blade can be embedded or mounted with a network of sensors to enable the health monitoring with high resolution. As the optical fiber transmits signals using pulses of light, it is lightweight, slim and immune to electromagnetic interference (EMI)

which can reduce the speed of transmission (Rogers, 1999). A fatigue test conducted by researchers (Pedrazzani et al 2012) suggested that fiber optic sensors technique can be used to accurately locate the defect before half the cycles to failure have been completed. Another dynamic strain tests by using small-scaled model has been conducted (Coscetta et al, 2017), and further proved its feasibility in full scale WTs. Figure 2.37 shows the optical fiber configured with temperature sensor and strain sensor.

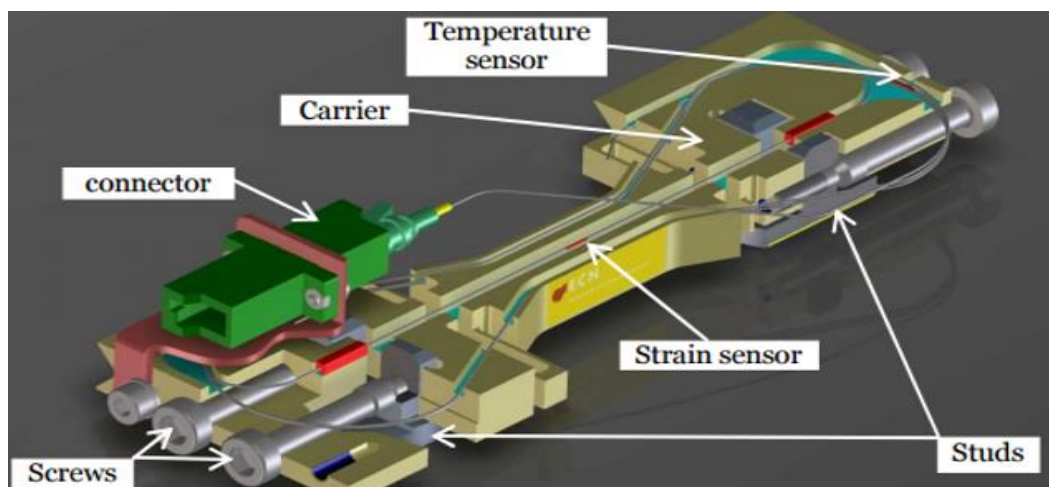


Figure 2.37 Schematic of fiber optic sensors

The fiber has a very high strain limit which means it can survive within the life time of the turbine system. However, OFM is complicated and its cost is expensive in practical applications compared with other BHM techniques (Guemes et al, 2010).

2.4.4 Laser-based Tip Deflection Measurement

The use of a distance laser device, installed on the WT, has been suggested to detect the changes in stiffness of the blade (Timmerman, 2009). This was achieved by measuring the amplitude of the deflection at the tip of each blade when the blade crosses the laser beam. It must be noted that the comparison between the newly measured deflection and the recorded “normal” deflection should be done when the system is

operating under the same operating conditions (i.e. wind speed, rotational speed and pitch angle) (Rolfes et al, 2014). Figure 2.38 shows the added devices and their mounted position on the WT.

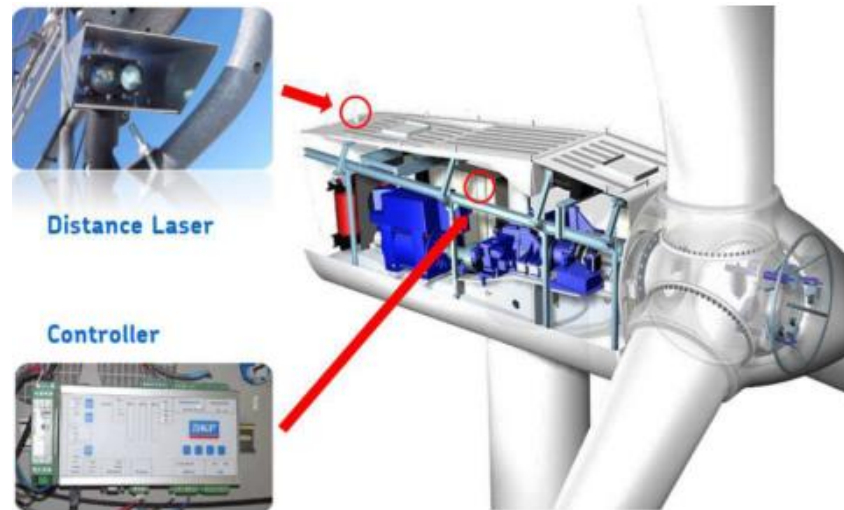


Figure 2.38 Schematic diagram of the laser-based tip deflection measurement

A lab experiment (Mankowski and Wang, 2016) proved that the edge-wise deflection of the blade can be also obtained by the use of a similar laser measurement, which means the pitch angle offset can also be detected. However, this has not yet been implemented on a full-scale WT.

2.4.5 Feasibility Assessment

Based on the consideration of the state of the art in WT blade monitoring presented above, the following considerations and conclusions associated with the application of these to TST can be made:

A reliable BHM technique has not yet been achieved. This assertion is based on the failure rate reported in regard to current WT operations. There is no standard technique which may be applied for WTs with different rotor diameters and configurations.

Therefore, it can be asserted that the sector is some way away from establishing the commercially viable BHM system for TST.

As mentioned above, AE techniques and systems are prone to be affected by the presence of external noise. During the operation of TST, the pressure variations and bubbles caused by cavitation, noise from the activities of marine organisms and the possible collision between the sea-bourn particles (sand and small stones) and the blade are inevitable, which means reliability of AE cannot be guaranteed under the sea.

Infrared thermography technique is the most intuitive method for monitoring the blade status as it doesn't need any signal processing. However, consideration of the physical properties of sea water suggest that an infrared camera cannot be used under the sea and this technique is not applicable for TST. As the same reason, the implementation of the laser-based tip deflection measurement is also not feasible.

The major obstacle for the implementation of optical-fiber sensors is their high costs. In addition, the performance of the strain gauge under impact and fatigue loads is another problem (Yang et al, 2014). However, a report shows that the strain gauge is capable of detecting mammal collisions with TST blade (Jha, 2016).

Taken overall it can be asserted that existing WT blade condition monitoring is evolving and yet to be fully commissioned. The added complications of fully immersed and remotely located TST devices must be addressed if viable CM systems are to be developed.

3. An Experiment-based Investigation on Dynamic Behaviour of the Small-scaled Turbine Structure

This Chapter introduces the preliminary understanding of the dynamic behaviours of TST. Two test rigs were designed to study the influences of structure-based and aerodynamic factors on the models, Specifically the vibration of the model and rotational speed of the rotor are analysed.

3.1 Introduction

For a TST structure, the hydrodynamic subsystem and mechanical subsystem contribute the most vibration. Therefore, the vibration source of the TST device can be classified and described as:

- The discussion about the hydrodynamic are presented in Section 2.3.2 (Chapter 2). The pressure distribution on the tower is affected by the blade passage and the loads on the blade vary with the azimuth angle if a flow profile is not steady and uniform.
- The rotor blades can be seen as a rotary disc. With the assumption that the rotational speed is constant, if the geometric centreline of the rotary disc didn't coincide with the mass centreline during the operation, there is vibration signal at rotational frequency will be produced. Note that the static unbalance of the rotor blade could results from mismatched weight distribution of the individual blades in manufacturing procedure.
- Assume that the flow profile is ideal steady uniform and rotor blades are

perfectly balanced, the extra bending moment caused by the B-T interactions can also result in an instant unbalance, which was discussed in Chapter 2.

As Figure 3.1 shows, two operating conditions are considered for vibration analysis of the TST structure.

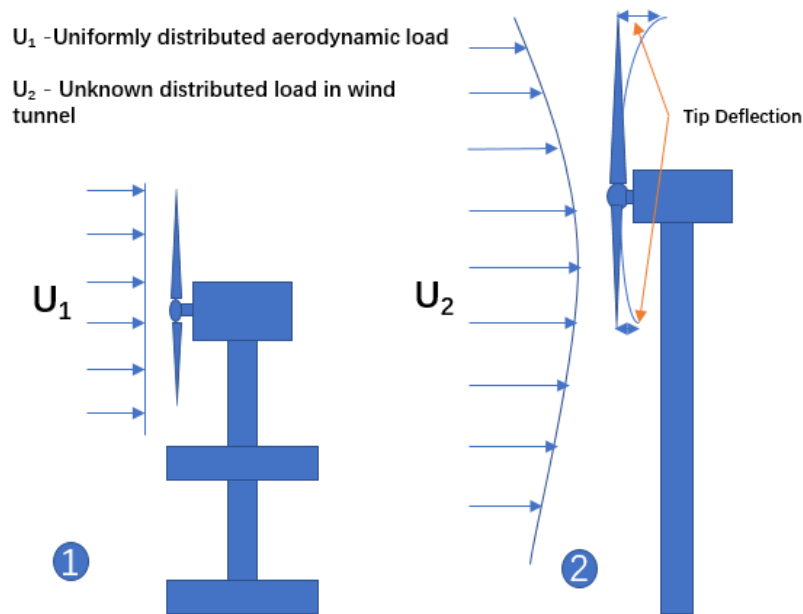


Figure 3.1 Schematic diagrams of two test rigs

1. With the steady and uniform flow profile and unchanging blade, the loads on the blade rotor can be seen as the steady input and the horizontal vibration solely resulting from the fluctuating total thrust can be minimised. In addition, the cyclic pressure variation on the surface of the tower, caused by the blade passage, can be highlighted and its impact on the vibration would be clearer.
2. The settings of the unknown wind velocity profile and deformable blade are closer to the real conditions of the WT or TST. With the ever-changing tip deflection, the thrust on each blade is fluctuated, which could lead to the vibration of the entire structure.

Both setups aim to provide valuable information and good references for developing the blade health monitoring (BHM) technique by analysing dynamic behaviour of the TST structure for each condition.

3.2 Experiment 1

As mentioned in Section 3.1, the blade must be set to be a rigid body to prevent the deflection by the wind, which can be simplified by the use of the metallic material of the small-scale model. A smaller wind tunnel is also needed to realise the relatively steady and uniform wind profile. Therefore, any vibration caused by the structural imbalance would be highlighted and the frequency domain analysis can be applicable to it.

3.2.1 Experimental Setup

Wind Tunnel

The experiment was conducted in a lab-scaled Armfield C2 subsonic wind tunnel which is equipped with a four-bladed fan driven by an electric motor with 2800 RPM maximum rated rotational speed. The tunnel comprises a fibreglass contraction and diffuser sections with a transparent parallel 30cm by 30cm test section. The honeycomb flow straightener is mounted within the contraction cone in the tunnel inlet. The wind speed is controlled by a voltage regulating device and increases as the input voltage increases. Figure 3.2 shows the photo of the wind tunnel described.

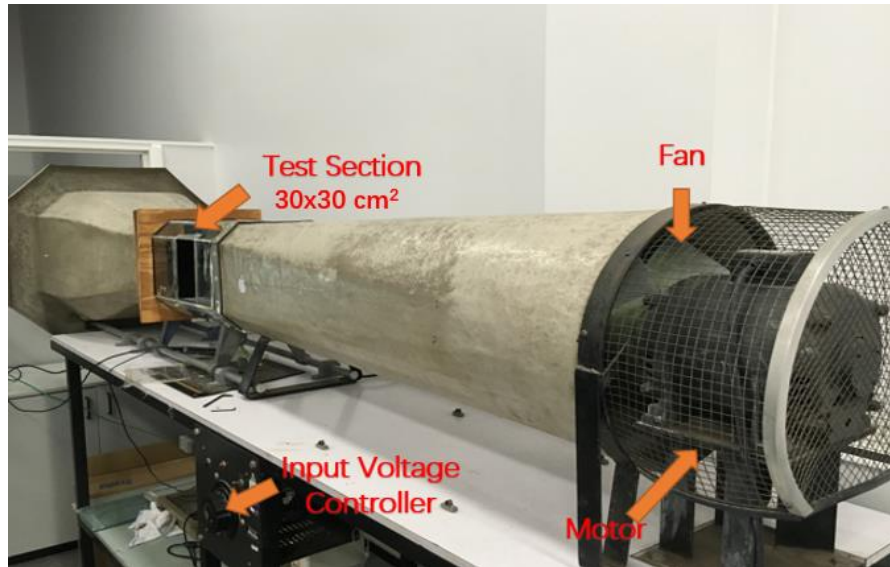


Figure 3.2 Armfield C2 subsonic wind tunnel

The results of the wind speed showed that the wind speed at the different points along the vertical or horizontal line on the cross-section is different with others. In that test, a pitot static tube supported by an adjustable metal bar was used to capture the airflow at a specific position and the other end of it was connected to an inclined manometer for pressure measurement. The manometer operates based on the Venturi principle and the point wind speed can be calculated as:

$$U = \sqrt{\frac{2 * \Delta P}{\rho_a}} \quad (3.1)$$

Where:

ρ_a is the density of air (kg/m^3).

U is the wind speed (m/s).

ΔP is the measured pressure difference (N/M^2). By using the inclined manometer, it can be calculated as

$$\Delta P = \rho_f * g * L * \sin\theta = h * \rho * g \quad (3.2)$$

Where,

ρ_f is the density of the manometer fluid (kg/m^3).

g is acceleration due to gravity (9.81 m/s^2).

L is length of the inclined tube.

θ is the horizontal contained angle.

The tube was successively placed at five positions along the vertical direction from 5 to 25 cm in height and the data was recorded with different voltage settings of the fan.

Figure 3.3 shows the results for these tests with the centre line of the test section shown.

Each point was the averaged value of the five repeated measured static results.

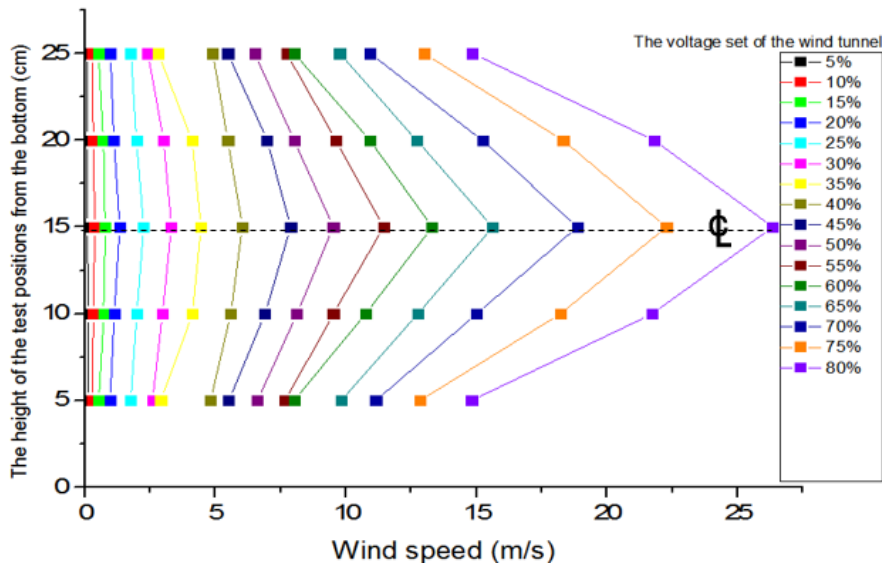


Figure 3.3 Measured point wind speed along the vertical direction in the wind tunnel

As Figure 3.3 shows, the highest wind speed in the cross-section was measured at the centre point and the difference between the middle and top (or bottom) increases with the input voltage of the wind tunnel.

Small Wind Tunnel Structure

A small wind tunnel structure, installed inside the big wind tunnel, was designed to enable vibration testing of the small motor structure. Its test section has 8x8 cm cross-sectional area and length of 30 cm. It is in the middle of the cross-section of the big wind tunnel and the wind generated by the fan is compressed into the small tunnel. There is another flow straightener mounted in the inlet of the small tunnel to reduce the turbulence. Figure 3.4 demonstrates the design of the small wind tunnel test rig.

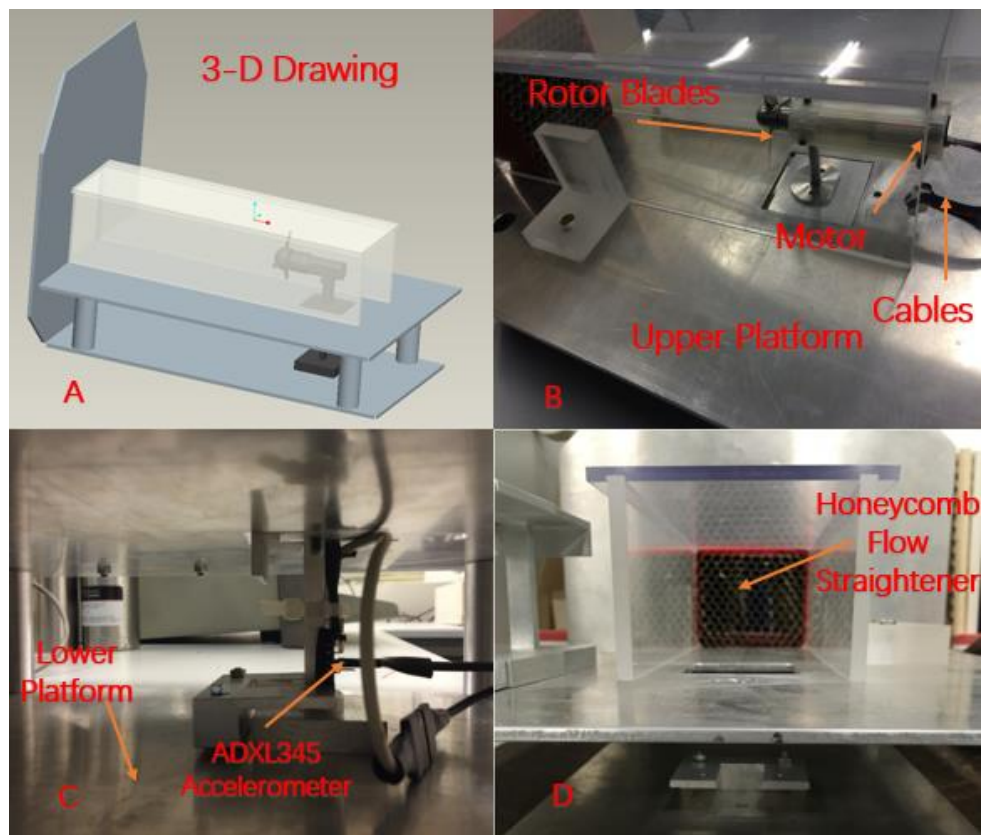


Figure 3.4 Overview of the small wind tunnel test rig. A) shows pro/e 3-D design, B) shows upper platform with small motor structure, C) shows location of the accelerometer. D) shows the rear view of the tunnel without motor structure.

The transparent cover can be easily removed to replace the blade rotor. Before

installing the motor structure, another wind speed test was conducted inside this small tunnel as the wind is compressed into the small tunnel and gained higher velocity with the same input voltage. By using the same inclined manometer, the tube was placed in different random positions within the cross-section of the small wind tunnel to measure the pressure. The readings of the device showed that the aerodynamic forces are nearly evenly distributed within the test area. Therefore, the average wind speeds with different voltage settings from 5% to 80% are accumulated and plotted in Figure 3.5.

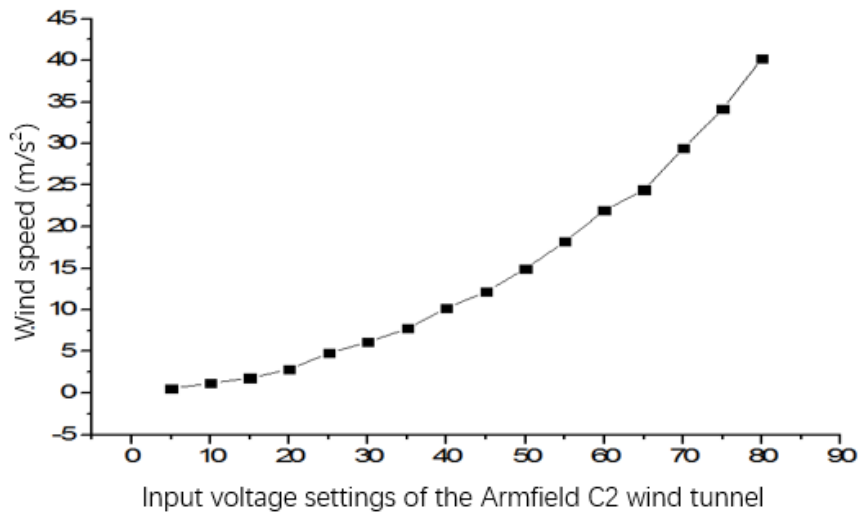


Figure 3.5 Wind speeds in the small wind tunnel with different input voltage settings

Small Rotor Structure

A 3-bladed rotor structure was used in experiment to convert the wind energy into the blade rotation. The diameter of the rotor is 50mm and there is a bearing installed inside the nacelle. The rotor structure was in good condition that the three blades were finely manufactured with same geometric features. The back end of the shaft has the screw thread to connect the encoder for rotational speed monitoring. After a series of tests, one of the rotor blades was intentionally made to be slightly bent for modelling

the faulty blade. Figure 3.6 shows the change of rotor structure before and after the test.

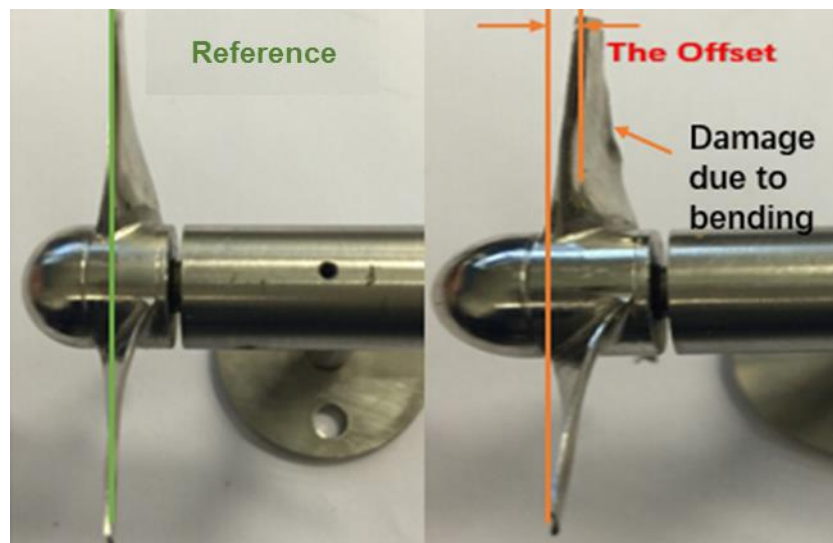


Figure 3.6 Reference and deliberately made faulty blade.

The structure was installed on an aluminium support structure which has two panels. The upper panel was used to block the gap on the upper panel of the small wind tunnel structure and the lower one was bolted with the bottom.

Data Acquisition Device

The NI myRIO-1900 was selected to be the data acquisition device. An H-Bridge Driver (PmodHB5) from the NI myRIO Mechatronics Kit was used to brake the rotor by generating the opposite torque with required duty cycle of the PWM signal. The NI LabVIEW, as the operating platform to control the myRIO, was programmed in the PC.

Figure 3.7 shows the physical connections of these hardware.

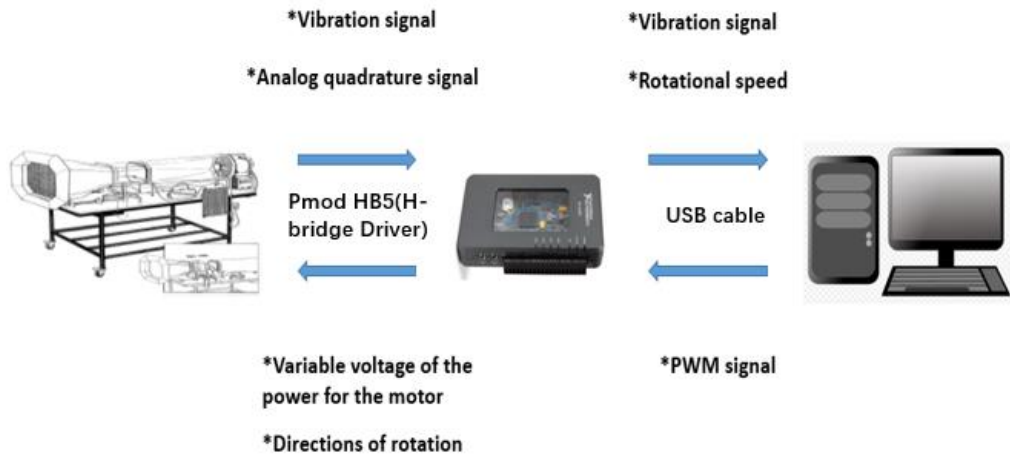


Figure 3.7 Schematic diagram of the hardware connections

The PmodHB5 was connected to the MXP Connector of the myRIO and offers the H-bridge circuit to drive the motor in either direction. Meanwhile, it receives the pulse waves from the rotary encoder and transfers them to myRIO. Figure 3.8 shows the block diagram of the PmodHB5. The quadrature signal was generated by the encoder and interpreted to the rotational speed by the program.

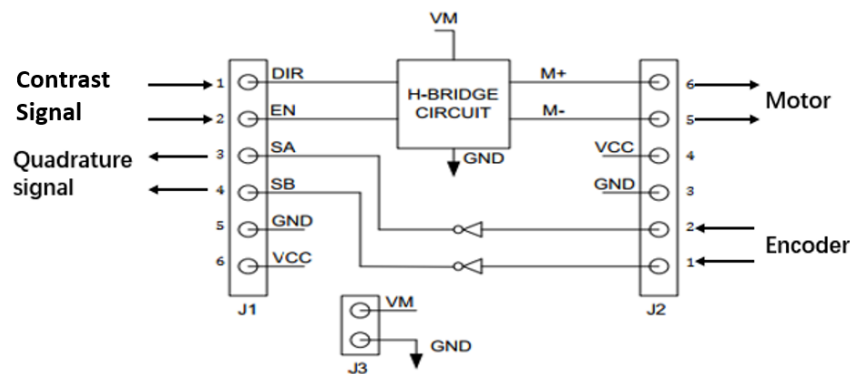


Figure 3.8 PmodHB5 block diagram

LabVIEW Programming

The programs for this test rig was made in the PC but operated in the myRIO. Unlike the myDAQ, the myRIO cannot directly set the file path to record the data and needs the 'Variable' block to associate two programs which respectively run in the PC and

myRIO. The Main program is shown in Figure 3.9 with annotations 1-8.

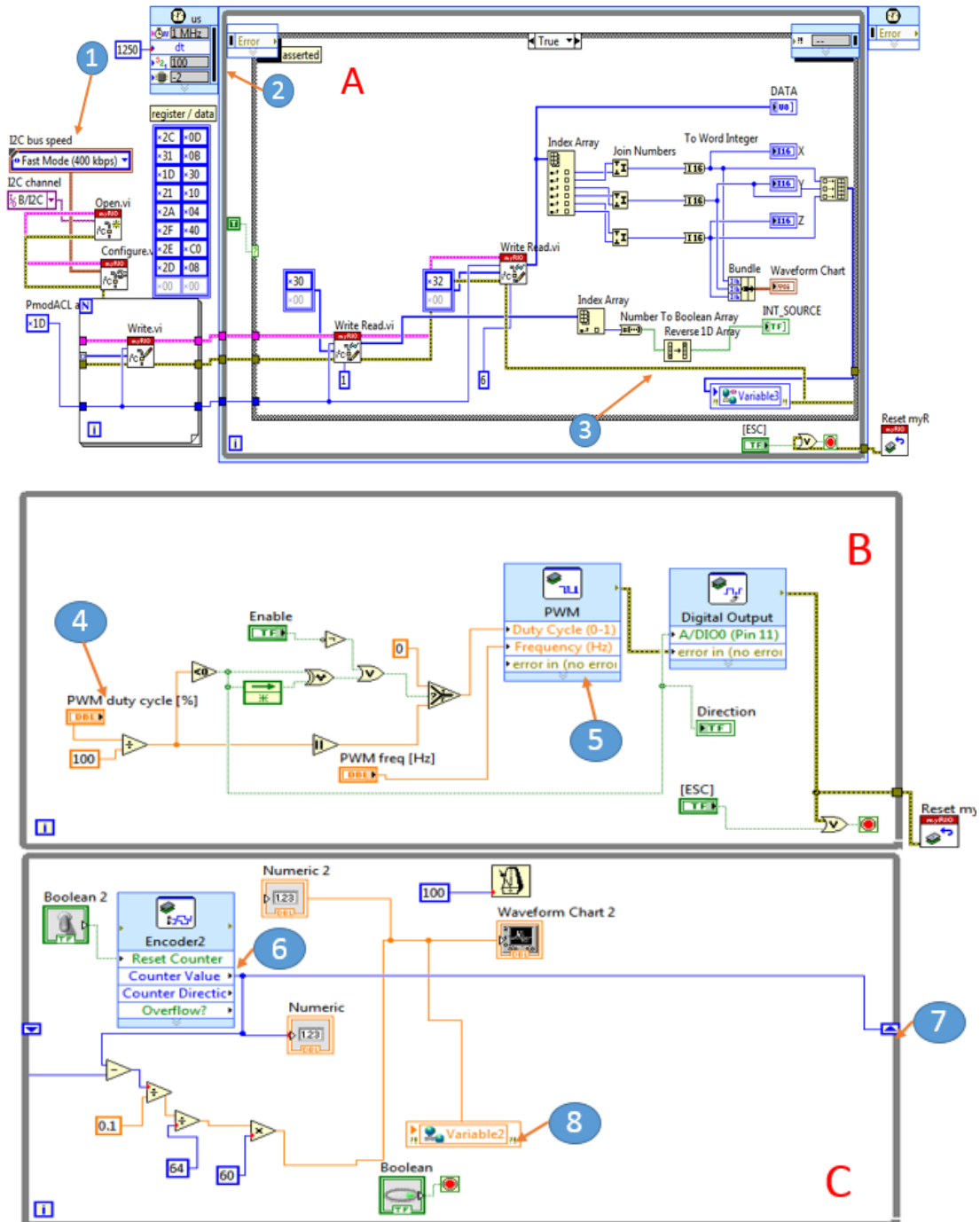


Figure 3.9 Block diagram of the Main program. A) Timed Loop for reading and recording the 3-axis vibration signal, B) While Loop for generating the PWM signal by setting the duty cycle, C) While Loop for calculating the instant rotational speed.

1. Setting mode of the I2C bus speed: Standard (100 kHz) or Fast (400 kHz). It was

Standard in experiment and the Bandwidth was set to 800 Hz in register table by hexadecimal rate code.

2. The Timed Loop setting box is used to set the display frequency of the data shown in the Waveform Chart on the front panel.
3. The 'Variable' block was created inside the Timed Loop and therefore the sampling rate of the data recorded is also set by this box. The six bytes were formatted into three 16-bit integers and then bundled into 'Variable' block.
4. The duty cycle was manually set to produce the corresponding input voltage for the motor. Note that the duty cycle can be set to negative number for the functions to generate the logical signal.
5. PWM generation block. The output pin was set in the block in advance. The 'Digital Output' acquired the logical signal calculated and transferred it to the H-bridge to control the direction of motor rotation.
6. The 'Encoder 2' block transfers the received quadrature signals and outputs the incremental value of the count up pulse.
7. The Shift Register passes values between loop iterations. The while loop calculates the difference between two adjacent numbers and get the instant rotational speed based on the circulation time set in advance.
8. The 'Variable2' block transfers the instant rotational speed to another VI program in the PC. The user can choose that when to start to record the program or how long the recording procedure lasts.

A LabVIEW-based FFT program was developed to help the user initially observe the

time domain and frequency domain of the 3-axis vibration signal. Figure 3.10 shows the front panel of the FFT LabVIEW program with annotations 1-4.

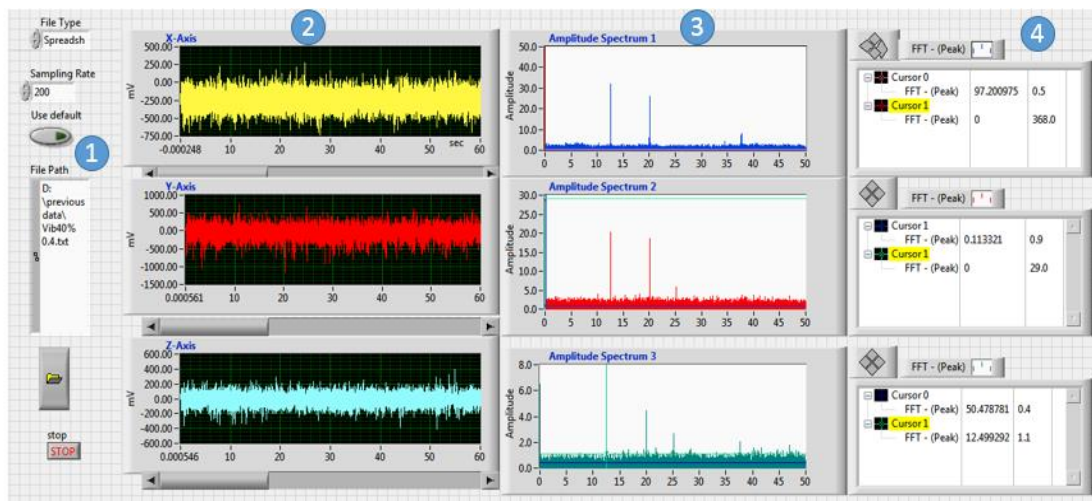


Figure 3.10 FFT LabVIEW program for the 3-Axis vibration data.

1. Set the format and path of the data file and sampling rate of the signal.
2. The waveform graph with scalable axis.
3. Frequency spectrum map of the corresponding signal.
4. Cursor indicator that find the peak amplitude at specific frequency component.

The co-ordinate system to classify the direction of the vibration is shown in Figure 3.11.

X axis is the flow direction, Y axis is the side direction and Z axis is the vertical direction.

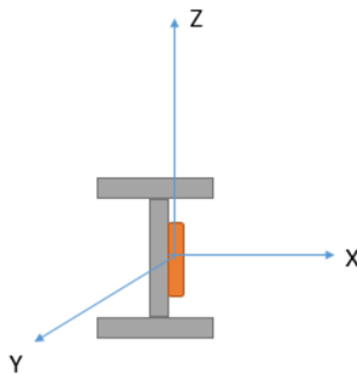


Figure 3.11 Coordinate system of the vibration signal

The Logging program, as Figure 3.12 shown, is used to synchronously record the rotational speed and vibration signal.

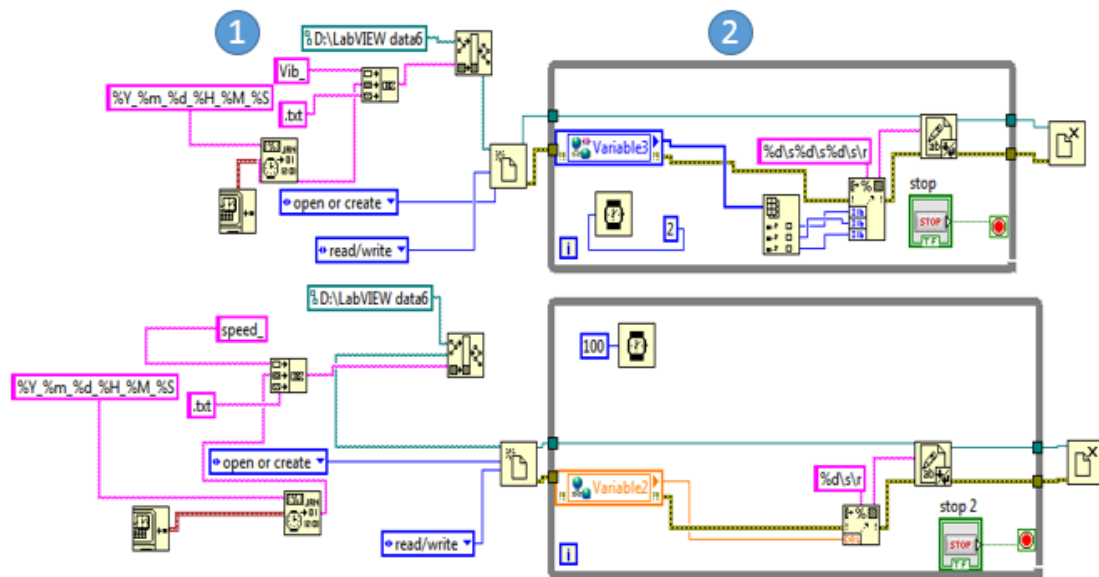


Figure 3.12 Data logging program in the PC

1. File naming and saving paths setting.
2. The While Loops for receiving the data from the Main program.

3.2.2 Experimental Procedure

The input voltage was set from 20% to 60% as the level of vibration caused by the higher wind speeds might damage the structure and the lower wind speeds were not enough to drive the motor. Using the established Nyquist criterion the sampling rate of both the vibration signal and rotational speed are set to be 200 Hz as the rotational speeds were not more than 1000 RPM. Each test was 90 seconds. The tests were divided into four groups:

1. Reference blade only driven by the wind with speed control (Marked as RBW).
2. Reference blade only driven by the motor (RBM).

3. Bent blade only driven by the wind with speed control (BBW).
4. Bent blade only driven by the motor (BBM).

For group 1 and 3, the motor was controlled to generate reverse torque against the torque driven by the wind. And, as the group 2 and 4 were operated without wind, the motor was driven to rotate the same direction as the group 1 and 3. Note that there is no feedback for the speed control. Table 3.1 shows the specific wind speed setting and the duty cycle sets for speed control.

Table 3-1 Wind speed and duty cycle settings for Experiment 1.

Groups	Wind Speed	Increments	Duty Cycle	Increments
No.1 & No.3 (RBW and BBW)	20% to 60%	1%	-0.1 to -1	0.05
No.2 & No.4(RBM and BBM)	None	None	0.1 to 1	0.05

*Note that the negative values of duty cycle represent the opposite direction of rotation

3.2.3 Results & Analysis

Figure 3.13 shows the average rotational speed comparisons between the optimal and the offset blade from 20% to 60% wind speed settings (Without speed control, duty cycle is 0). With the increase in wind speed, this difference increases as expected due to unequal thrust on the bent blade.

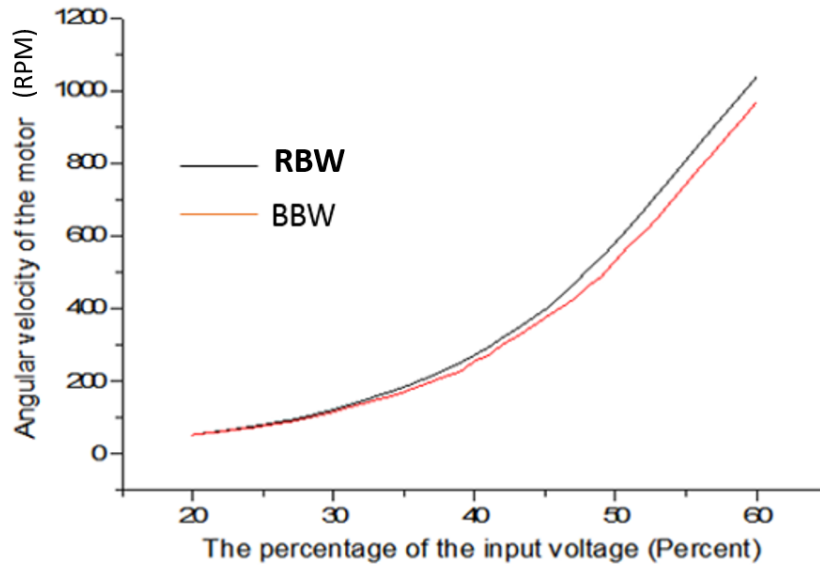


Figure 3.13 Rotational speed of the two rotors in different wind speed (without speed control).

For analysing the entire reference groups, there are two things which need to be considered:

1. It is inevitable that there is slight unbalance in the reference rotor blades. As this influence can be reduced by lower the rotational speed, the groups of data which has the lower rotational speed should be selected for analysis.
2. The direction which is more sensitive for the abnormal vibration caused by the offset blade is unknown before the test. Therefore, the vibration in 3 directions were plotted together for better analysis.

The Z direction (Vertical) is least sensitive direction for vibration due to the installation method for the rotor blade structure. In addition, the vibration in Y axis solely resultants from the wind pressure is not the object of this study. Therefore, the vibration signal in X axis is only one to be analysed.

Figure 3.14 shows three examples of the frequency spectrums of RBM operated with 0.3, 0.5 and 0.7 duty cycle. The fundamental frequency can be observed that coincides with the rotational frequency (ω) which was calculated from the recorded data for corresponding settings. The rotational speed for 0.3, 0.5 and 0.7 duty cycle settings are respectively 240(ω_1), 402 (ω_2)and 551(ω_3) RPM.

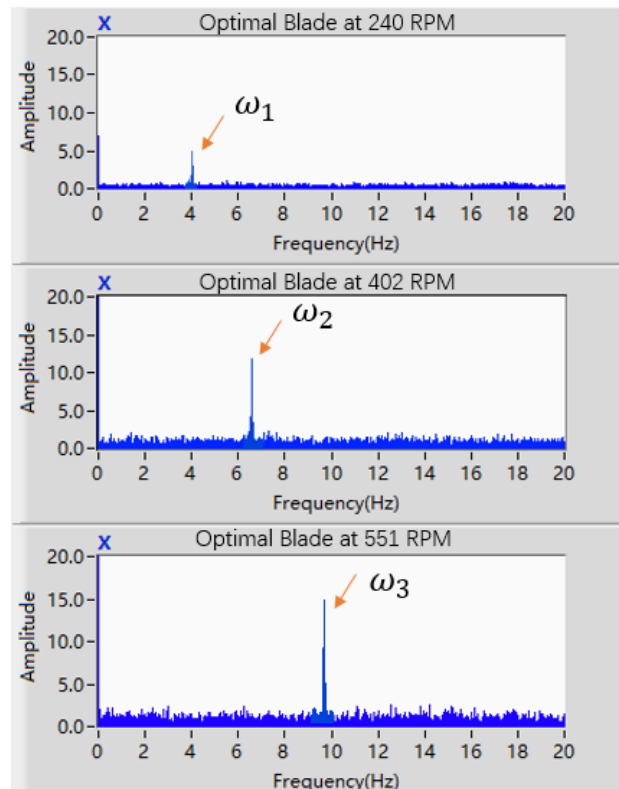


Figure 3.14 Amplitude spectrums of the OBM with 0.3, 0.5 and 0.7 duty cycle.

The range of amplitude and frequency of each spectrum was respectively zoomed to 0 to 20 for better viewing. Without wind, the vibration of the structure is only caused by the blade rotation. This indicates that influence of the imbalance of the reference rotor blade is proportional to the square of the rotational speed, which can be expressed as the following equation:

$$F_{unbalance} = m * r * \omega^2 \tag{3.3}$$

Where $F_{unbalance}$ is the unbalance force generated by the blade rotation, m is the mass of the rotor, r is the distance between the geometric centreline of the rotation axis and ω is the angular velocity.

The data from OBW and BBW with the rotational speed lower than 240 RPM were selected to do further analysis as the impact of the inherent rotor imbalance are relatively minimum.

Figure 3.15 shows the amplitude spectrums of the vibration in X axis of reference structure. With speed control, the rotor operated at 240 RPM in three wind speed settings: 0, 40% and 60%. The fundamental frequency in each spectrum is equal to the rotational frequency as expected. When the model operated at the wind with speed control, the amplitude arises at the second and third harmonics and increases with the wind speed. This is because the wake behind the rotating blade will generate the pressure variation on the tower surface.

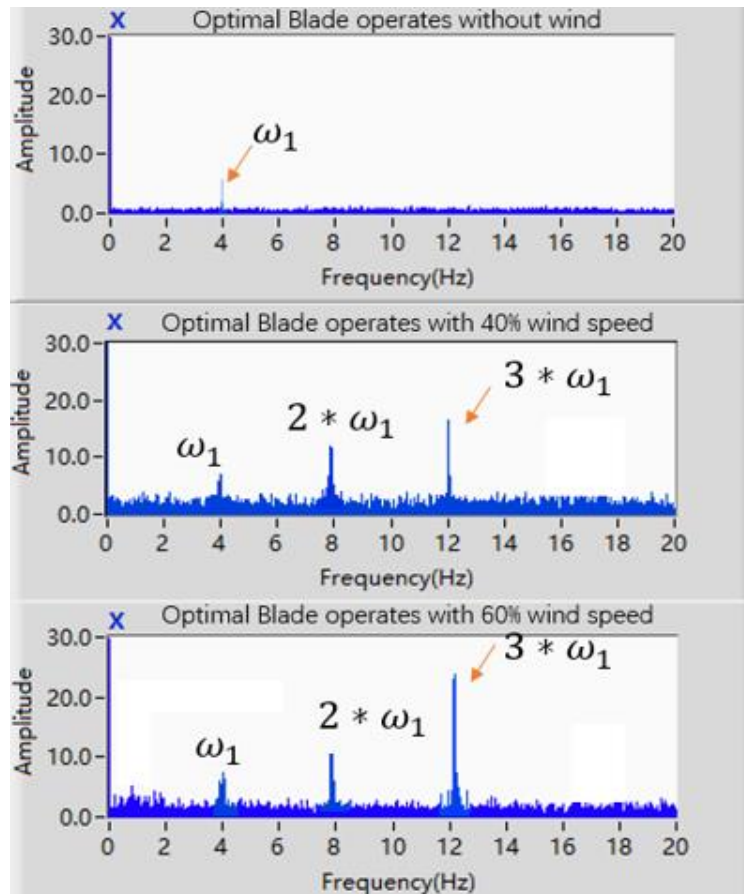


Figure 3.15 Amplitude spectrums of the reference blade operated at 240 RPM with different wind speeds

Figure 3.16 shows the amplitude spectrums of the vibration under faulty condition with same rotational speed in different wind speed (Speed Control). Without wind, the peak amplitude in the spectrum for the case of offset blade is at ω_1 as expected. Also, when the wind force is applied to the structure, the amplitude at ω_1 increases with the flow velocity, as the thrust fluctuation increased at the offset blade. However, the presence of the even harmonics could be explained as the influence of the blade passage. The pressure variation on the surface of the blade is more like a square wave rather than the sine wave, which means the result will not be like the pure imbalance vibration signal.

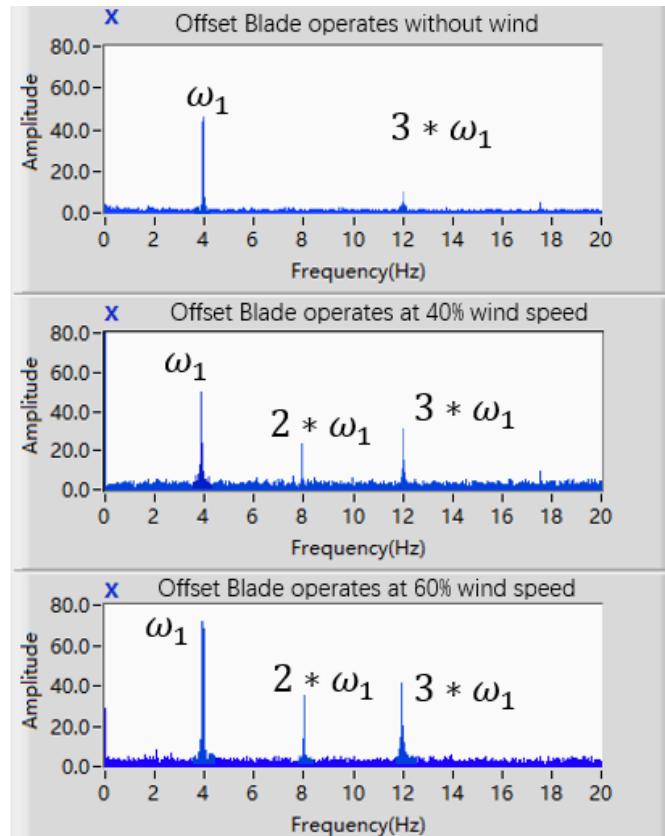


Figure 3.16 Amplitude spectrums of the offset blade operated at 240 RPM with different wind speeds

3.2.4 Summary for Experiment 1

By maintaining the rotational speed at a relatively low level, the vibration caused by the inherent rotor imbalance for reference structure can be minimised. This could help to clearly understand the influence of the aerodynamics on the structure via the comparisons between the test groups with and without wind. The thrust fluctuation on the offset blade was also observed.

In this case, the blade was assumed as a rigid body and not deformed by the wind force. With the fixed rotational speed and rigid blade, the presence of the second harmonics then can be attribute to the blade passage: As the blade moves in front of the

tower, the wind pressure on the tower will decrease instantly after blade passage. Therefore, the vibration caused by the pressure variation on the tower should also contribute to the amplitude at frequency ω_1 . However, due to the dominant influence of the total wind load variation on the rotor, the frequency domain analysis of the vibration signal can only prove the existence and influence of the blade passage but cannot further explore its characteristics.

3.3 Experiment 2

The experiment was conducted with a HAWT model which has the structural features that are more similar to the practical WT compared to the model in Experiment 1:

1. The blade could perform flap-wise deflection according to the wind speed (or force) and the potential edge-wise deflection could also exist with an unknown extent during the experiment.
2. The rotatable support base enables the swept area of the model faces to wind direction with different angles for modelling the yaw error scenarios.
3. The wind loads in the swept area are not evenly distributed, which causes the unpredictable vibration for the whole structure.

The experiment was designed to further study the blade-tower interaction in more realistic conditions.

3.3.1 Experimental Setup

3-D printed stanchion

The rotor blade used in this test (with 26 cm diameter) was taken from the small-scale model of direct-driven wind turbine made by National Grid, China. For preventing

interferences from many of other factors caused by, for example, parts used for connection., this structure was designed as symmetrical parts which are printed by 3-D printer. The accelerometer is adhered on the back of the nacelle. Figure 3.17 shows the photos of the cross-section view of the stanchion (without the cables) and the blade.

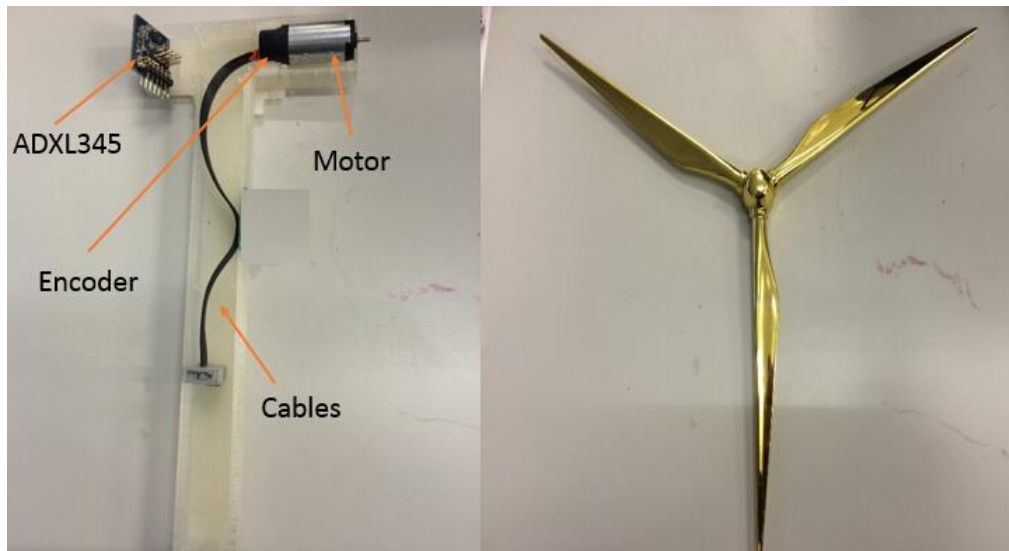


Figure 3.17 Cross-section of the stanchion and the blade part.

The low cost of the 3D printer's material makes all parts are convenient to be changed and thereby the details of this structure can be optimised frequently in the design phase.

Configuration of the Testing Rig

Figure 3.18 shows the photo of the entire test rig mounted inside the Armfield C2 subsonic wind tunnel. The stanchion passes through the bottom end of the tunnel and the base section was fixed on the horizontal platform. Unlike the previous test rig, the base of the structure is bolted on the platform of the wind tunnel bench. Thus, the vibration from the rotating fan is significantly reduced due to no physical contact between the test rig and the inner wall of the tunnel.



Figure 3.18 Final assembly of the testing rig

Other setups such as the programs and hardware are same as Experiment 1.

3.3.2 Experimental Procedure

After a series of tests, the experiments were conducted in the range of wind speed from 10% to 40% to avoid damage to the plastic blades. Powering the motor to rotate in the direction against wind flow for speed control. Table 3.2 shows the increments of the variables for each test. The sampling rate of the vibration signal is 500 Hz.

Table 3-2 Wind speed and duty cycle settings for Experiment 2.

Wind Speed	Increments	Duty Cycle	Increments
10% to 40%	5%	0 to 1	0.05

The average rotational speed of the model WT with the speed is shown in Figure 3.19. With the increase of duty cycle, the rotational speed gradually decreased.

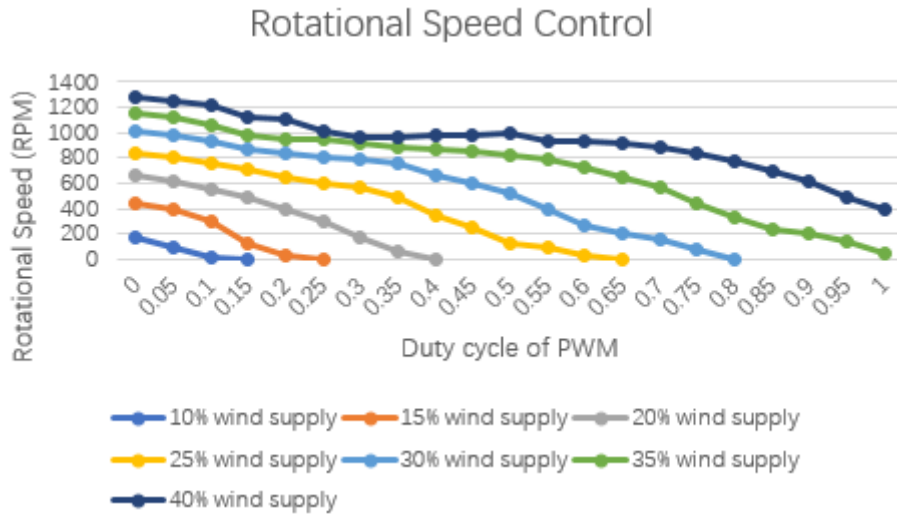


Figure 3.19 Results of the rotational speed in normal operation

The tests are classified into 4 groups: 1, Reference blade. 2, Offset blade. 3, Offset blade with yaw error 3°. 4, Offset blade with yaw error 5°. 5, Offset blade with yaw error 10°. In the groups of 2, 3, 4 and 5, the blade was attached by a tape on the surface to make the reference rotor become imbalanced. The reason for using tape is that the offset blade can be restored to normal for the later experiment.

3.3.3 Results & Analysis

The 405 experimental datasets were finally obtained. After initial observation via the LabVIEW program, some representative datasets were plotted by MATLAB for better viewing and analysis.

The vibration data from testing of the reference blade and offset blade conducted at 40% wind speed and 1 duty cycle (Maximum brake setting) are shown in Figure 3.20 and Figure 3.21 respectively. The length of data segments was chosen to 2 seconds. The signal segments between the two red grid lines represent the contribution of the vibration from one revolution.

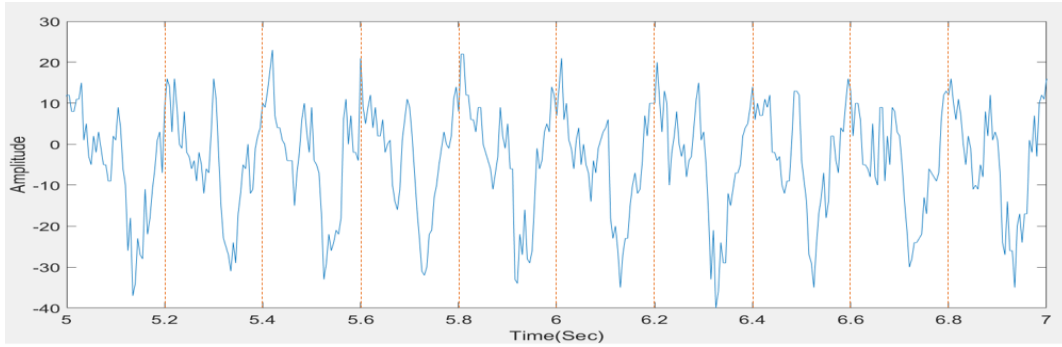


Figure 3.20 Vibration data for reference blade at 40% wind speed and 1 duty cycle

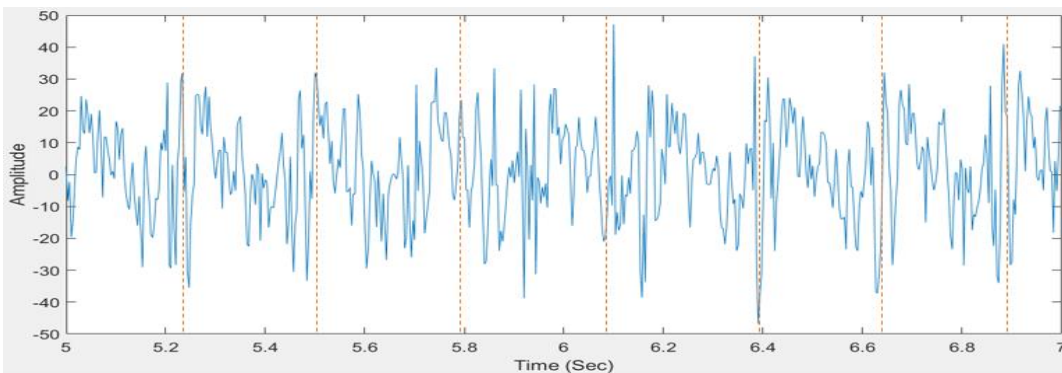


Figure 3.21 Vibration data for offset blade at 40% wind speed and 1 duty cycle

As the rotor imbalance reduced the rotational speed of the model, the reference model rotated faster and the vibration data shown in Figure 3.21 for the offset blade fluctuates far more frequently. The differences between two sets in time series can be readily observed. However, as the vibration data was not synchronised with blade position, it is difficult to explain how each blade passage affects the vibration during one rotation.

Figure 3.22 shows a composite waterfall spectrum plot, for the 21 optimum blade tests with different duty cycle settings. With the increase of duty cycle, the rotational speed decreases at the same wind speed.

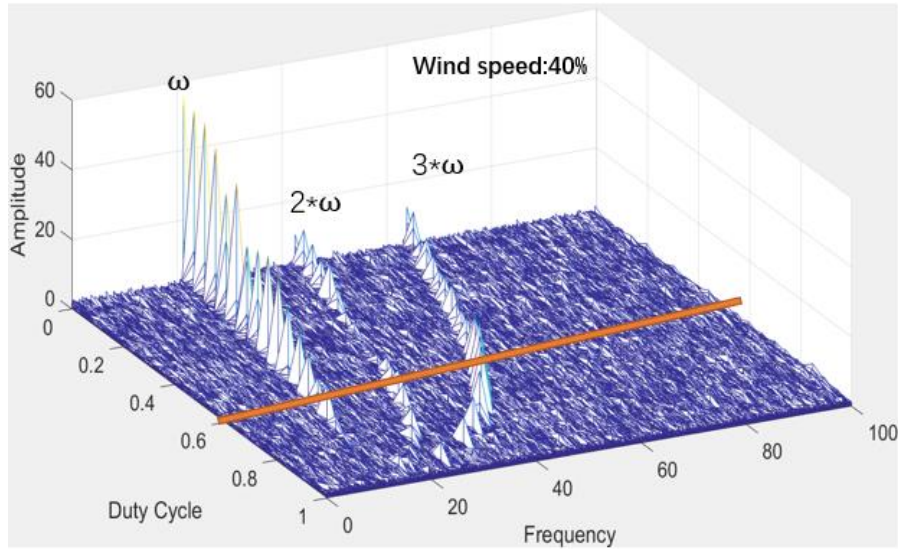


Figure 3.22 Waterfall amplitudes frequency spectrum for 21 optimum blades tests

The rotational frequency (ω) was readily detectable, from the total horizontal vibration signals, and strongly correlated with the angular velocity of each setting. However, the rotor imbalance for reference blade dominates the axial vibration when the duty cycle is lower than 0.6. To prevent the inference from the inherent imbalance of the reference blades, the datasets used for analysis were selected from the groups that the rotational speed is lower than 600 RPM.

Figure 3.23 shows the comparative results obtained for 10 of the datasets at 40% wind speed.

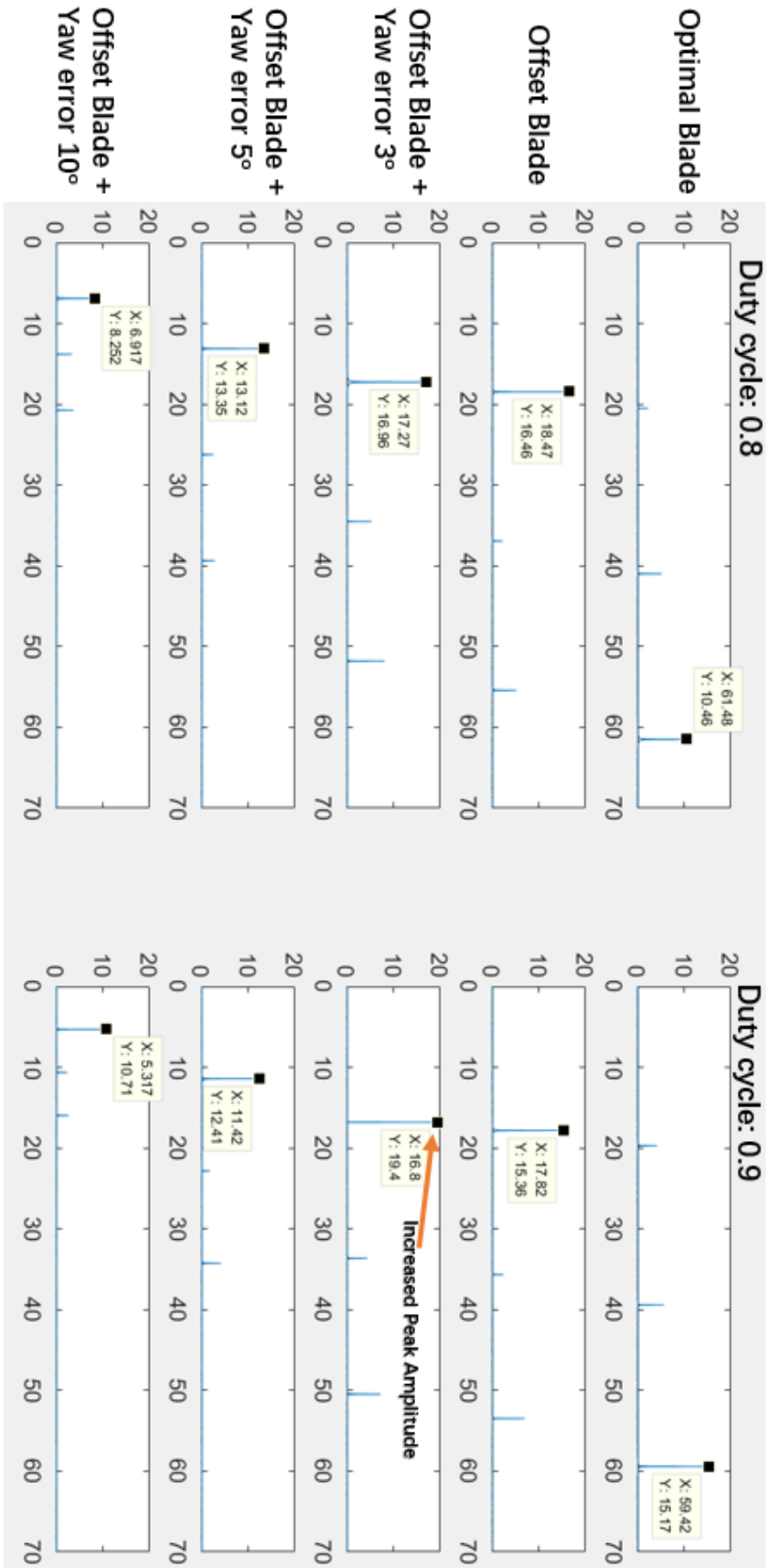


Figure 3.23 Comparison of amplitude frequency spectrum results.

As expected, the peak amplitude of the vibration of the offset blade is at the rotational frequency which also decreases with the increase of the yaw error degree. With speed control, the peak amplitude at the rotational frequency for each setting decreases as the increases of duty cycle except the datasets from 3° yaw error (The cross section of the tower is square and this structure with yaw error could generate much more vibration than the optimal one. In this test, it is 3°). As discussed in Section 3.1, the discrepancy of the thrust on the offset blade can contribute the amplitude at the rotational frequency. However, with the yaw error, this discrepancy should be reduced as the change of the angle of attack. Known that the biggest total thrust can be obtained when there is no yaw error and any difference of the thrust caused by the offset blade should be maximum as well. Therefore, the marked peak amplitude in Figure 3.23 can only be explained as the vibration caused by the distinct pressure variation of the offset blade passage. The results of the 3° yaw error can not be prevented as the tower cannot be printed to a perfect cylinder.

3.3.3 Summary for Experiment 2

A waterfall amplitudes frequency spectrum for reference blade can be used to detect the influence of the inherent rotor imbalance which increases with the rotational speed. Then, the vibration-based analysis can be used to identify the deliberately made faulty blade at the 40% wind speed. At the 3° yaw error, the pressure variation on the tower caused by the faulty blade passage coincidentally contribute the most amplitude among the different parameters, which draws a special attention on the corresponding influence of the hydrodynamic subsystem. However, the information of the vibration-based

monitoring system cannot be used to find the influence trends of the blade passage.

Therefore, measuring the dynamic pressure variation on the tower during the blade rotation could be the most intuitive way to start this study.

4. An Innovative Method of Flow Pressure Profile Measurement and Blade Status Monitoring

This Chapter introduces the blade monitoring method that utilises blade-structure interactions. In particular, the dynamic variations of pressure measured on the front face of the support pillar are tested and analysed. Water flow around between working blades and the pillar will be influenced by some factors including rotational speed, flow velocity, blade conditions and tip clearances. The expectation of deteriorated blade condition changing the measured forces was investigated via experimental testing in a wind tunnel. The chapter includes some preliminary test rig designs and evaluations. The details of the developed test rig are then introduced and the results and analysis are presented.

4.1 Introduction

Based on the consideration of the Blade-Tower interactions reported in Chapter 2 this work was set up to meet two purposes and the wind tunnel test rig design accommodated an array of structure mounted sensors which were to be used to (1) estimate local flow conditions and (2) to utilise the blade-structure interactions to support the wider monitoring regime for developing progressive blade faults. The former is an important consideration as commercially deployed TSTs will operate in ever-changing flow directions, velocities and with varying velocity vs depth flow profiles. It was hoped that condition specific adaptations could be applied to any condition monitoring algorithms. Ideally, the developed methods would be designed to be relatively sensitive to the

prevalent flow conditions.

This experiment aims to use the flow pressure measurement to take the place of the conventional methods of blade health monitoring such as the measurement of the thrust, vibration and laser-based tip deflection. These approaches may be said to be mature in the field of the wind turbine industry but cannot directly applied on the tidal turbine due to the harsh underwater environment. To support this investigation the wind tunnel was adopted for conducting the experiment. A variety of low pressure sensors were considered and evaluated. As a result the PAW sensors were selected based upon their overall performance and on parameters including good durability and sensitivity for operation in a wind tunnel.

4.2 Preliminary Test

The feasibility and performance of the PAW sensors were tested. The PAW sensors details appear in the following section. A stanchion with four holes was designed and manufactured to support four PAW sensors in different heights in the central section of the Armfield C2 subsonic wind tunnel. For convenience, 3-D printing technologies were used in manufacture of prototype stanchions. Design development work was undertaken within the SolidWorks design software. Finished parts were then processed using file conversions to produce stanchions to appropriate dimension tolerance. The pictures of the test rig installed within the wind tunnel are shown in Figure 4.1. Figure 4.1(a) shows a side view of the general arrangement. Figure 4.2(b) shows a plan view and Figure 4.1(c) shows a front view from within the wind tunnel. The 3D-printed stanchion was vertically mounted on the base and thus the embedded PAW sensors can

face airflow properly.

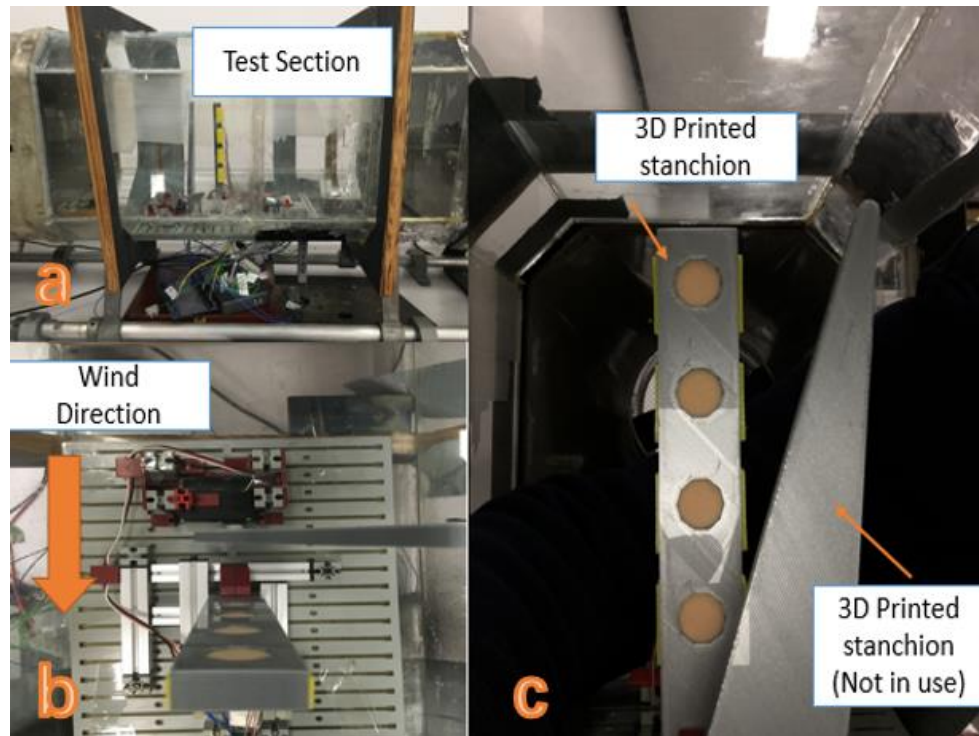


Figure 4.1 Test rig of the preliminary test.

4.2.1 PAW sensors

Traditional methods used to measure pressure distributions in wind tunnels are with multi-tube manometers or pressure-sensitive paint (PSP) installed in the test section (Arifuzzaman and Mashud, 2012). For data logging, however, in this application the dynamic effects on the large stanchion, with minimal flow disturbance, was required.

The PAW sensors, shown in Figure 4.2, consist of a cylindrical urethane sponge and two LED light sensors. Its working principle is a combination of piezoelectric and optical methods. The light sensors are used to detect how much the sponge is compressed by the external force and then this volume variation is converted to an analog output. Rapid deformation of the sponge is attainable and thus the dynamic response of the PAW sensor is sufficient for the application.

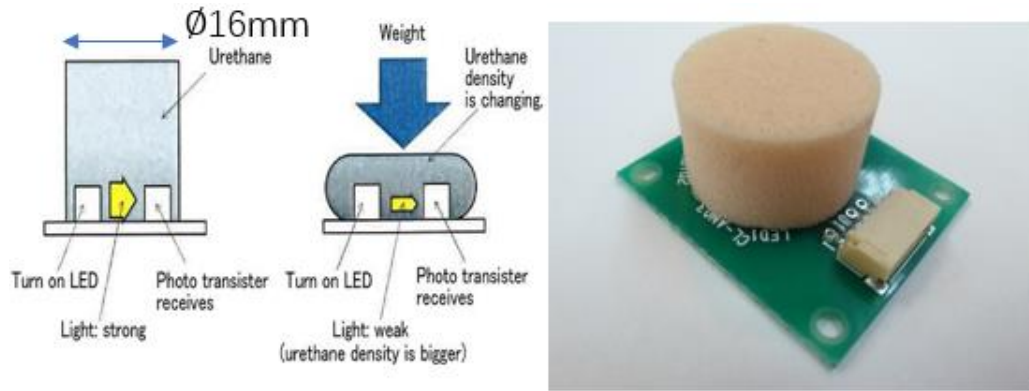


Figure 4.2 Schematic diagram and picture of the PAW sensor. Source: RT Corporation, 2013.

To provide initial estimation of the pressure levels to be sensed, the following simple approaches were used: The wind pressure P can be calculated by equation 4.1.

$$P = 0.5 * \rho_{air} * U^2 * C_d \quad (4.1)$$

Where,

ρ_{air} , the air density is 1.225 kg/m^3 according to the environmental parameters in the laboratory

U is the air speed in the wind tunnel

C_d , the drag coefficient which is equal to 2

From prior wind tunnel tests, the wind speed in the test section is known to be controllable between 0 and 23 m/s, which is equivalent to wind pressures in the range 0 to 372.2 N/m^2 on the given testing area value has. These estimations were used in a calibration process. The PAW sensors were respectively calibrated by using lab weights from 0 to 7.5 g, with 0.1 g increment. In the calibration, a 0.15 g round gasket with same face area was used to ensure that the sponge was evenly compressed. When PAW sensors were later used in a wind tunnel, a thin round foil disc was attached on the

sensor surface to prevent any potential error caused by the small pores of the sponge.

4.2.2 Method for Preliminary Test

By using the same stanchion, the probe of the inclined tube manometer was fixed to measure the wind pressure at the same locations. The difference of the results between PAW sensor and inclined tube manometer would be considered as the criteria for judging the performance of the sensor and the design of the test rig. Based on the working principle of this sensor, the pressed part of the sponge would extend radially and the hole needs the appropriate space to match with it. For a certain wind speed, the too small space would limit the sponge to be pressed and the overmuch one could make the unnecessary turbulence in it. Therefore, several stanchions with different size of the holes are made by the 3-D printer as Table 4.1 shown.

Table 4-1 Dimensions of the round holes

No. of the stanchion	Diameter of the hole (mm)
1	16.2
2	16.3
3	16.4
4	16.5
5	16.6

Each hole in every stanchion was initially designed as 16.5 mm in SolidWorks and then manually modified. Due to the working principle of inclined manometer and PAW sensors, the external factors such as temperature and lighting conditions could affect the accuracy of the experimental results. Therefore, each set of the pre-tests and the following experiments were conducted under the normal laboratory lighting with the

temperature between 10 and 12 °C.

4.2.3 Results

The results of this measurement are logged into the PC by myRIO. Figure 4.3 shows that comparisons of the measured wind speed in 40%, 50% and 60% input voltage of the wind tunnel. Each curve consists of four values from the sensors at different positions with same wind speed and the sensors are marked as PAW1-4 from the top to the bottom (25, 20, 15 and 10 cm). It is necessary to simultaneously test all the sensors due to the possible difference of the compressibility for each cylindrical sponge. The reason that the towers used in preliminary test and later experiments were different was related to the capabilities of the 3-D printer which could not print a tower longer than 20 cm.

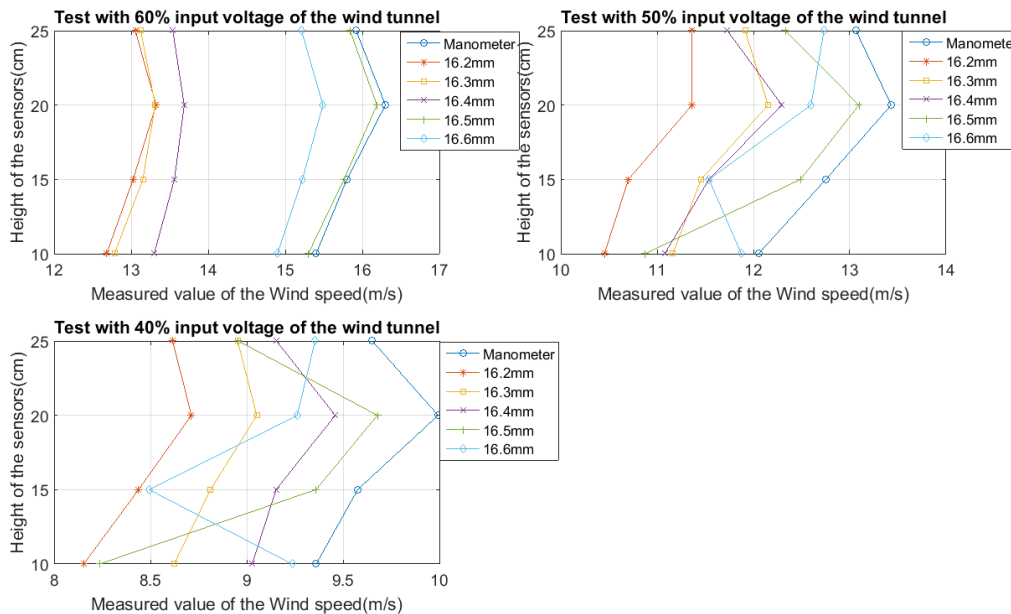


Figure 4.3 Results of the wind speed measurement in initial test

In 60% wind speed, the values measured in the 16.5 mm round hole (green line) have the smallest errors with those from the tube manometer compared to other sizes.

Therefore, in this wind speed, 16.5 mm is the optimal diameter for the round hole for installing the PAW sensors in any height. However, in 40% and 50% wind speed, the measured values from PAW 1 and PAW4 installed in the 16.5 mm round hole are far different from the manometer test. This is mainly because excessive space could make much turbulence due to the closed rear end of the PAW sensor. In addition, the 16.6 mm round hole provides more excessive space for pressed sponge and its results have more error. According to the above analysis, the optimal diameter of the round hole is 16.6 mm for PAW 1 and PAW4, and is 16.5 mm for PAW2 and PAW3 operated within 40% to 60% input voltage of the wind tunnel.

4.2.4 Summary

In preliminary test, the difference between the readings of the inclined tube manometer and PAW sensors is within an acceptable range, which proved the feasibility of the PAW sensors for this experiment and the comparisons above indicate the appropriate size for each of the holes on the tower to optimise the performance of the PAW sensors. In addition, the calibrated PAW sensors are only tested in the wind speed of 40% to 60% to minimise the turbulence between the sponge and the inner wall of the hole and thus to guarantee their performance. However, it cannot be ignored that there is a certain error in the readings from the inclined tube manometer. Therefore, the results from the PAW sensors installed in the ‘optimal holes’ are not completely reliable but closest to readings from manometer.

On the other hand, the sensors with this type of working principle still have many technical problems which need to be solved prior to it is formally used under the sea.

For example, the sponge must be replaced by other materials due to floating matters and microbial growth. The sensitive element with this deformation characteristics need to withstand additional underwater pressure which would affect the performance in long-term operation. And, it will be difficult to monitor the running state of the sensor itself because of its underwater operation. In summary, the flow pressure sensor with this type of deformation element needs more testing and improvement to realise this idea for TST application.

4.3 Experimental Arrangements

The main experiments were conducted in the same wind tunnel. The schematic diagram of the test rig is shown in Figure 4.4. The part which is used to fix the servo motor will not be moved during the test to prevent the error caused by the difference of wind speeds in horizontal direction in tunnel. The part used to fasten the support pillar was designed with movable base for adjusting it to a required distance with blade.

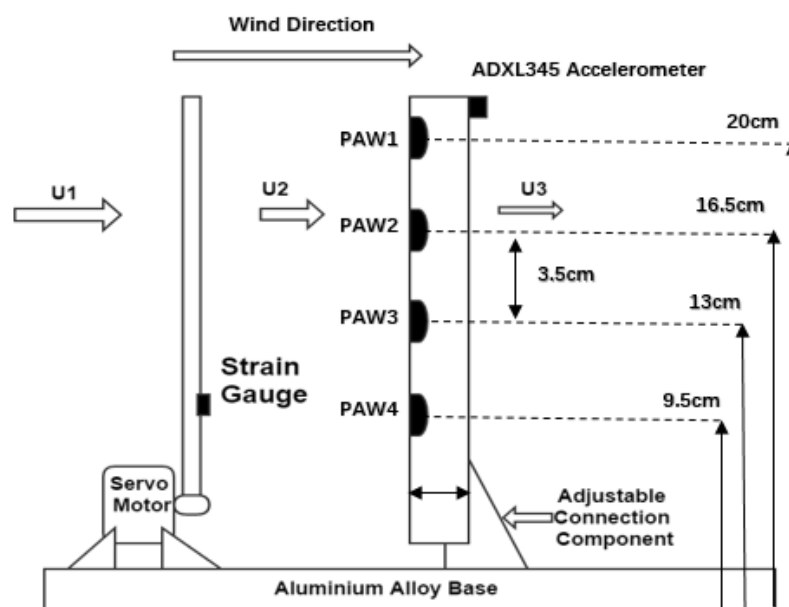


Figure 4.4 Schematic diagram of the test rig

4.3.1 3-D Printed Blades

The two blades used in the experiment are printed by the high quality 3-D printer due to the low cost and good performance of the material. The geometric features of the tidal turbine blade are not being studied; therefore, the blades are designed as a homogeneous and symmetrical 240x30x7 mm flat plate. The two blades are shown in Figure 4.5. The Blade 1 is instrumented with strain gauge, which the relationship was calibrated between the output voltage and the deflection of the blade tip rather than its strain. In the test, the root of the blade is fixed on a servo motor that can precisely rotate to any azimuth angle with specific speed. The Blade 2 is designed with the same properties but 5° pitch angle offset. Note that Blade was in good conditions before the experiments and the failures were gradually added as required during the experiment.

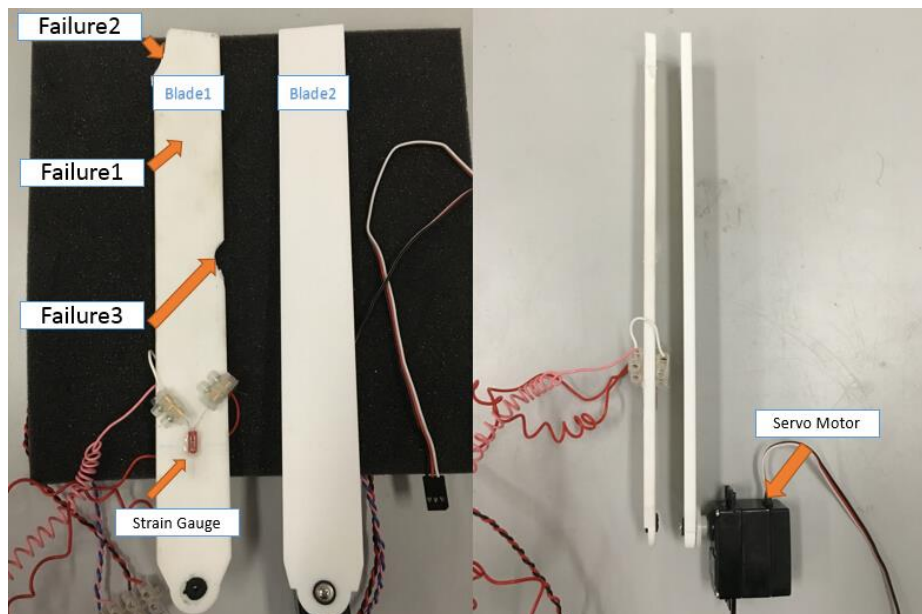


Figure 4.5 Instrumented 3D printed blade

4.3.2 Stanchion and Base Frame

As the Blade-structure interactions are associated with the vibration of the entire

structure and deflection of the stanchion, a structure with independent blade and support pillar was designed for simplifying the issues to the interactions only brought by aerodynamics. The stanchion (which is longer than the printed one in pre-test) in the experiment was made by a 250x27x12 mm aluminium cuboid with four holes on the surface. The servo motor and the tower structure was independently mounted on an aluminium alloy base which is tightly fixed to the bottom plane of the wind tunnel. The diameter for each hole is determined by the results of the pre-test with many 3-D printed models of the stanchion. Figure 4.6 shows the pictures of the test rig in the wind tunnel. All the cables come out from the sealed hole on the bottom.

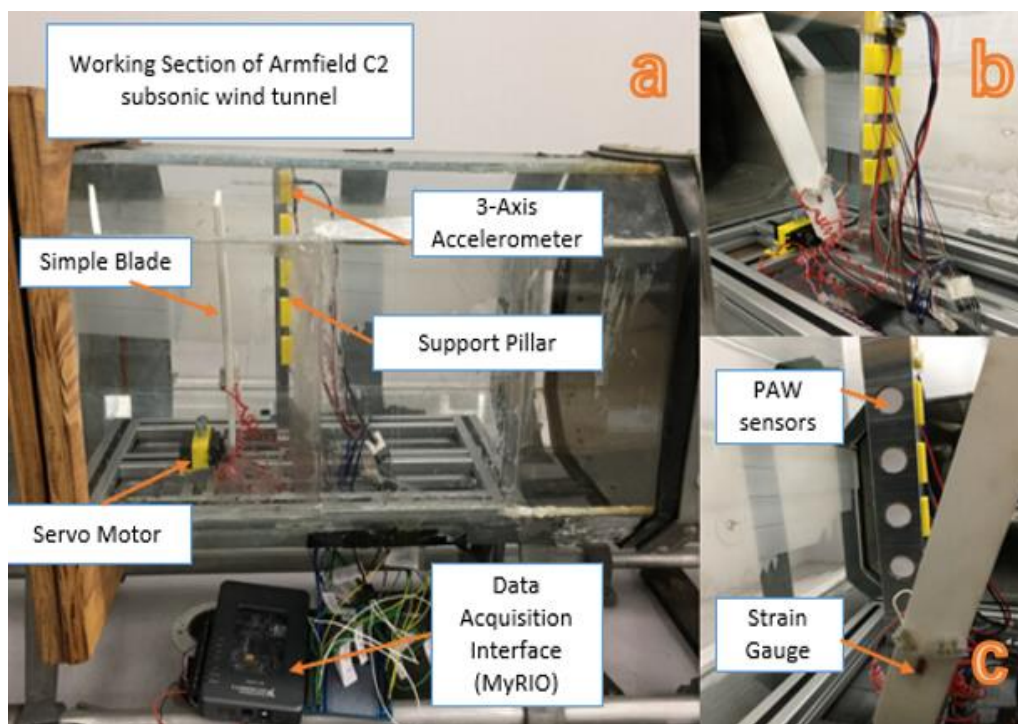


Figure 4.6 Configurations of the test rig

Figure 4.6(a) shows a side view of the general arrangement. Figure 4.6 (b) and Figure 4.6(c) respectively shows a face view and a back view from within the wind tunnel.

4.3.3 Monitoring System for Test

Two LabVIEW programs are designed and run independently in the PC and myRIO, as the latter device cannot be programmed to record by directly selecting the file path on the PC. In Figure 4.7, the Main VI conducted in the myRIO acquires all data and transfers them to the PC. The Logging VI performs the recording task once the user needs.

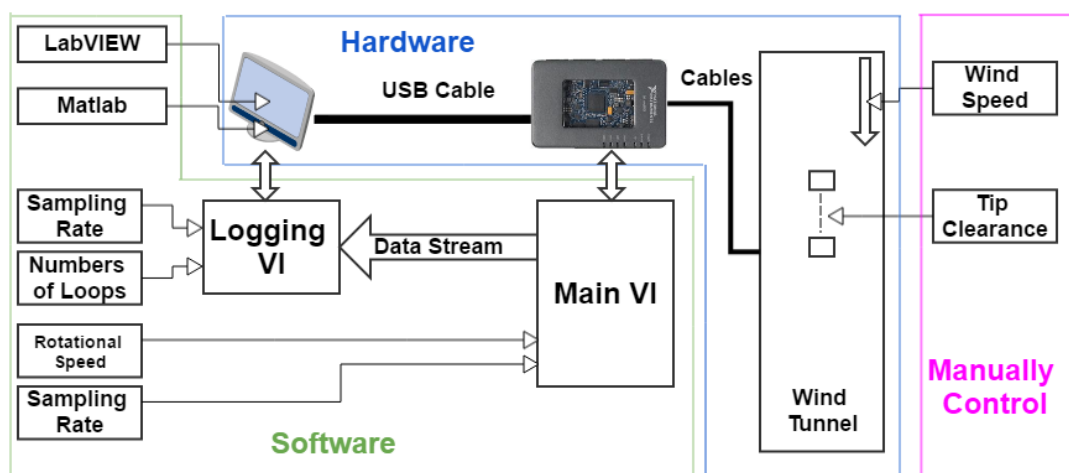


Figure 4.7 Schematic diagram of the monitoring system

Figure 4.8 shows the front panel of the LabVIEW program. The top window with white background shows the real-time vibration signal at 3-axis. The bottom four windows indicate the pressure variation from the top to the bottom of the stanchion and the gap in each window represents the shadowing area caused by the blade passing. The window in the upper right corner shows the real-time tip deflection of the blade and the area below is programmed to control the rotational speed and direction of the servo motor.

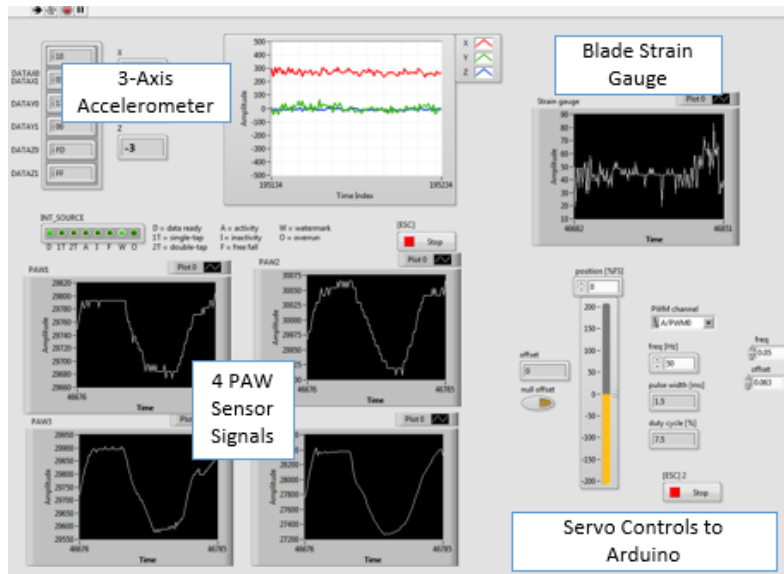


Figure 4.8 Front panel of monitoring system

However, the offset for the servo motor needs to be reset to start the Main VI, which would reduce the accuracy and efficiency of the experiment. Therefore, the area in the bottom right corner is programmed for the Arduino board that can automatically and precisely reset the motor to the default position.

Figure 4.9 shows the typical recording of wind pressure measurements from the 4 deployed PAW sensors and the unit of the Y axis shown in the data acquisition screen is millivolt. The estimate flow pressure had been remaining stable and decreased as the blade-tower interaction.

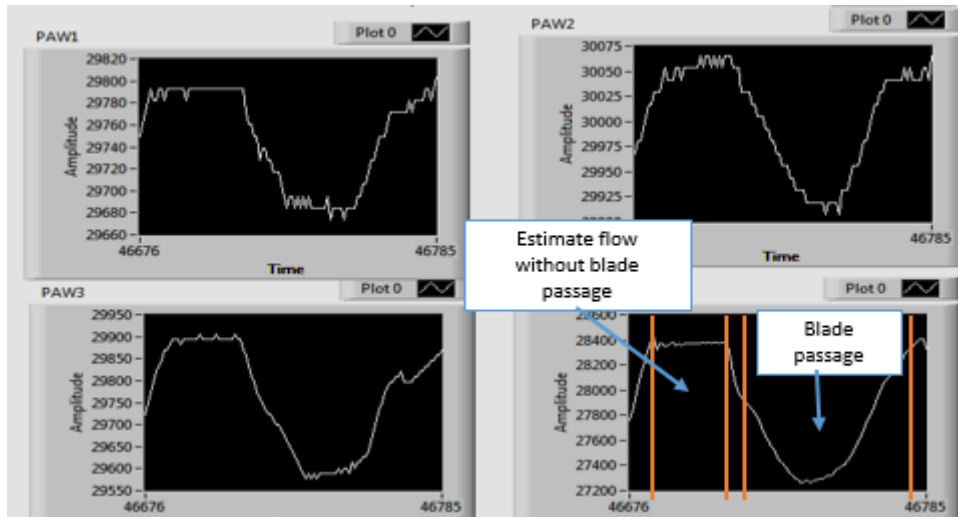


Figure 4.9 Screen shot of flow pressure measurement

4.4 Experiment Procedure

There are five groups of the test as Table 4.2 shown. The first group of the tests was conducted by using the flat blade (marked as Blade 1) and the blade with 5° pitch angle offset (marked as Blade 2) only used in second group. From the third to the last group, Blade 1 was physically modified with the different failures step by step, which means the blade in fifth group had already been modified to the one with Failure 1, 2 and 3 after finishing the experiments above.

Table 4-2 Arrangement of the blade in static and dynamic tests

The Testing Group	The Blade Type (Pitch Angle)	Testing Method	Description
No. 1	0 °(flat) with strain gauge	Static &Dynamic	A rectangular plate without any defects
No. 2	5° without strain gauge	Dynamic	A rectangular plate with 5 degrees offset from its root.
No. 3	0 °(flat) with strain gauge	Dynamic	An obvious abrasion was made behind the plate. The shape of the blade is same as before but the stiffness was changed. (Failure 1)
No. 4	Same as above	Dynamic	Based on above, an obvious breach was made on the leading edge of the plate top. (Failure 2)
No. 5	Same as above	Dynamic	Based on above, an obvious breach was made on the trailing edge of the middle of the plate. (Failure 3)

4.4.1 Static Test

The static test is conducted in 3 tip clearances as 3cm, 4cm and 5 cm. Set the vertical

position as 0 degree, the blade started from -30 to 0 degree with 5-degree increments. And, the input voltages for adjusting the wind speed were 40%, 50% and 60%. Before each test, the blade was set by the main LabVIEW program to the desired angle in the certain wind speed. After that, the program for logging data are executed for 90 seconds with 200 Hz sample rate which is sufficiently high for analysis. Each group would be tested in 40%, 50% and 60% wind speed. Finally, there are 63 data sets of the deflections of the blade and the pressure on the tower are recorded. Table 4.3 shows the details of the static test and only Blade 1 is used in this test.

Table 4-3 Static tests settings

Blade	Wind speed	Tip clearance (mm)	Tower width(mm)	Azimuth angle
Blade 1	40%	30, 40 and 50	27	-30° to 30° with 5° increments
	50%	30, 40 and 50		
	60%	30, 40 and 50		

4.4.2 Dynamic Test

With the same tip clearances and the wind speeds in the static set, the dynamic tests conducted as the blade starts rotation from -30 to 30 degrees and then turn back to -30 degrees after 60 degrees of rotation with same angular velocity. The servo motor drives the blade to move and is controlled by the triangle signal generated from LabVIEW. By

changing frequency of the triangle signal, the rotational speed was set to 8, 10 and 12 RPM for each group and marked in turn as S1, S2 and S3 for convenience. Table 4.4 shows the sequence of the experiments.

Table 4-4 Dynamic tests settings

Blade	Blade conditions	Wind speed settings	Rotational speed	Tip clearance (mm)	Tower width (mm)
Blade 1	Reference blade	40%	S1, S2 and S3	30, 40 and 50	27
		50%			
		60%			
		40%			
		50%			
		60%			
	Failure 1	40%			27
		50%			
		60%			
	Failure 2	40%			
		50%			
		60%			
Failure 3	40%				
	50%				
	60%				
Blade 2	5° Offset	40%			
		50%			
		60%			

There are 144 datasets in total were recorded and each set of data includes vibration,

flow pressure, blade strain and the additional generated logic signals for synchronization of the above data. Figure 4.10 shows the method of the data processing before the signal analysis.

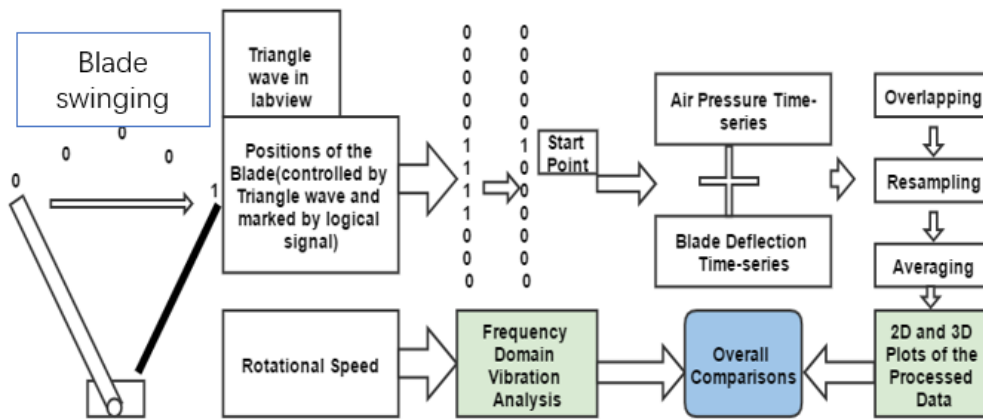


Figure 4.10 Diagram of the signal processing

As the discrete nature make the value of the triangle signal obtained in the program cannot perfectly indicate the real initial point of each of the one-time periodic swinging, therefore, by setting a small threshold value near the start point, the program will simultaneously generate logic value 1 within the threshold and 0 otherwise with 200 Hz sample rate. Although the position of the blade can be at any degree at the beginning of running the data logging program, the first logical value 1 which is followed by a short list of value 1 still can indicate first start point of the blade swinging. And then replacing the extra logical value 1 to be 0. However, it is inevitable that a certain degree of error happens during each one-time periodic swinging due to the immediate stop when the blade reaches 30 degrees. For example, the first loop of the blade swinging at 10 RPM could have 400 data points but the second might be 406. By using the ‘Find’ function in MATLAB to record the number of the data points of each loop as a vector.

And, overlapping and resampling air pressure data to calculate the average trend of the pressure variation for each loop for the further processing or comparisons. Figure 4.11 shows an example of processing the data with S2, 60% and 3 cm tip clearance.

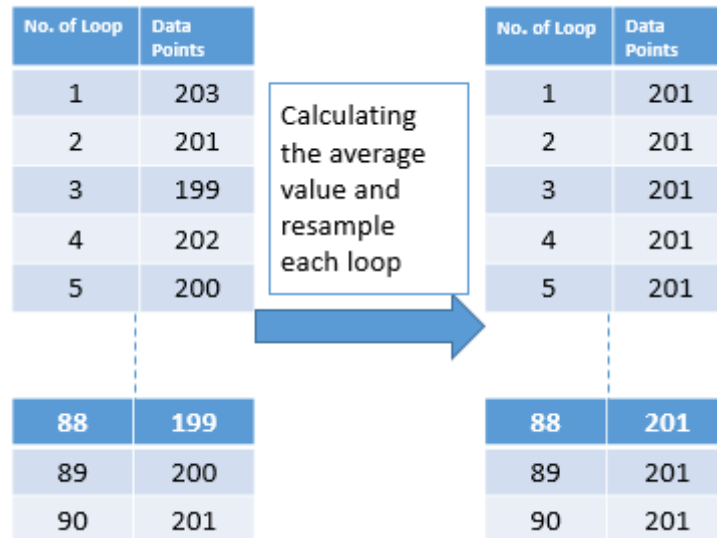


Figure 4.11 Procedure of the resampling each loop

Although the data points obtained in S2 (10 RPM) for each loop should be 200, the left table shows the actual number of data points from raw signal. After calculating the average number, each loop can be then resampled to 201. (Note that the average value could be different for each set with same rotational speed) However, if the comparison was made between the cases with the same rotational speed. Each loop in every set should be resampled to the same frequency. For example. The sets with S2 and S3 were respectively resampled to 200 and 167.

4.5 Experimental Results and Analysis

4.5.1 Static Test

From top to bottom, the PAW sensors are marked as PAW1, PAW2, PAW3 and PAW4. Before the test, a tube manometer had been used to measure the wind speed and

determined the highest wind speed is in the middle of the wind tunnel which is the location of the No.3 PAW sensor (marked as PAW3). Figure 4.12 shows the wind pressure at the four PAW sensors in different height and there is no blade in front of the tower, which means the curves roughly indicate the flow profile in middle vertical position direction.

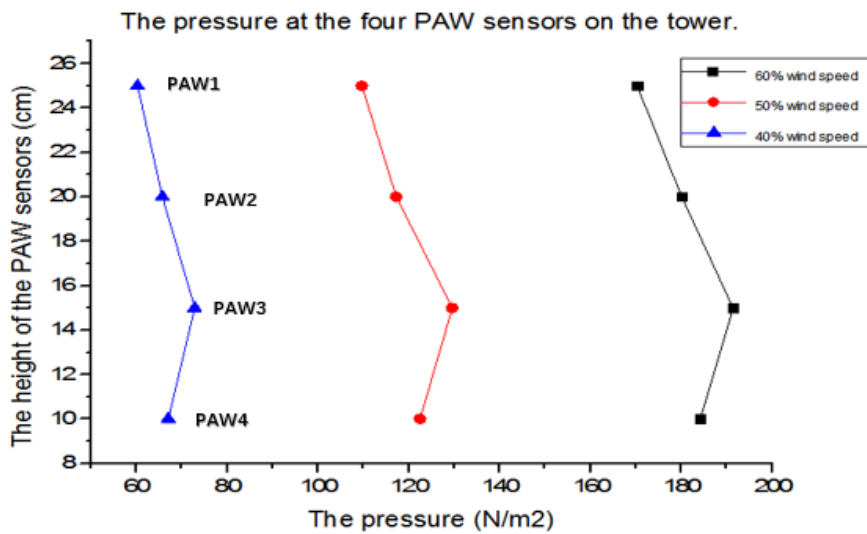


Figure 4.12 Wind pressure distribution on the stanchion at different wind speeds.

Figure 4.13 shows an example of the average pressure values from four PAW sensors when the blade was stopped in different positions with 3 cm tip clearance in 40% wind speed. Note that the sensor positions are changed as the tower in the preliminary test is shorter than the one in this experiment.

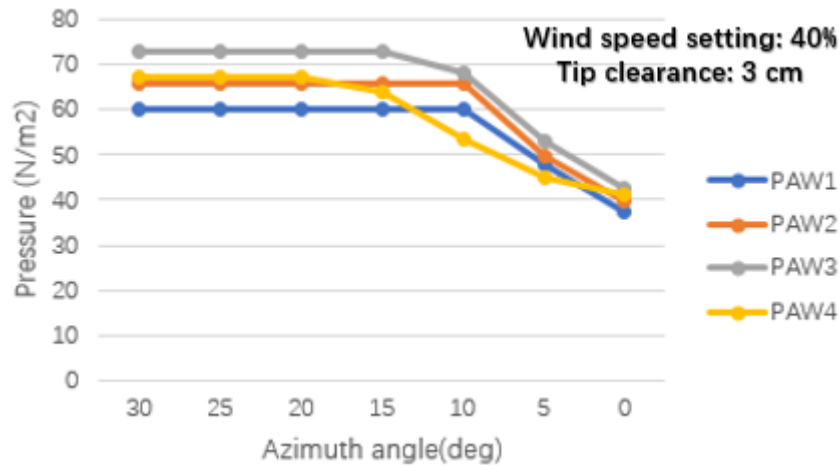


Figure 4.13 Pressure variation on the stanchion with 3 cm tip clearance.

The pressures on the tower from PAW1 to PAW4 are affected between 15 and 20 degrees due to the blade coverage and dropped to the lowest point when the blade is vertical as the tower. Due to the more blade coverage, the pressure on PAW4 starts to decrease from 20 degrees and keep dropping with smaller gradient compared to others.

Figure 4.14 shows the pressure change of PAW sensors with 5 cm tip clearance in 40% wind speed. The larger tip clearance made the PAW sensors receive the different stage of the wake flow of the blade and thus changed the gradient of the pressure decrease.

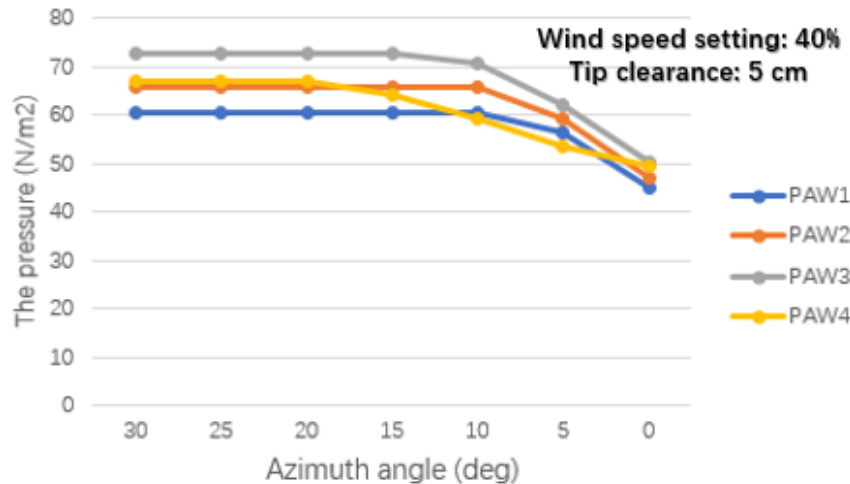


Figure 4.14 Pressure variation on the tower with 5 cm tip clearance.

There is another example about pressure on the tower in 60% wind speed shown on Figure 4.15. With the same tip clearance, the pressure on PAW4 declined faster than it in 40% due to the coverage of the blade with higher deflection in 60% wind speed.

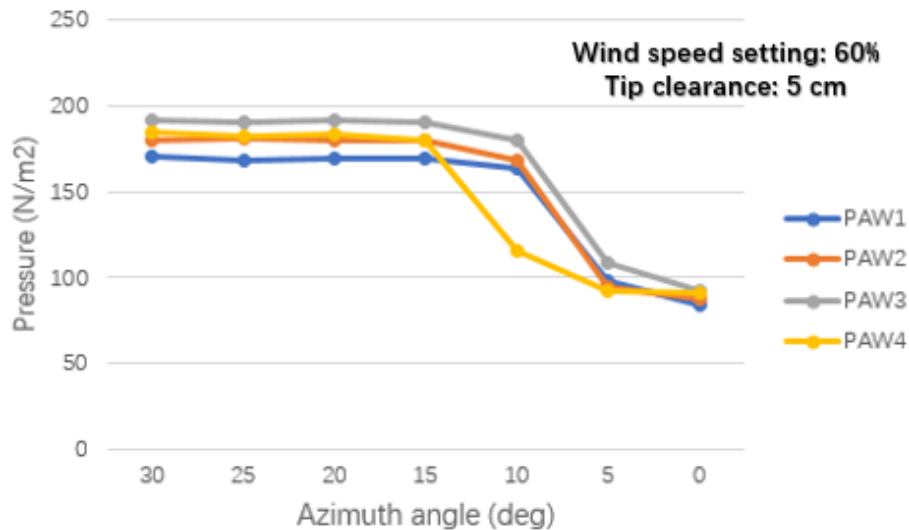


Figure 4.15 Pressure variation on the stanchion with 60% wind speed

Due to the flow profile inside the wind tunnel, the highest blade deflection occurred in the vertical position. There is an example of the average deflection results is shown in Figure 4.16. The blade deflection increases as the reduced shadowing area. This phenomenon can be explained as : the presence of the tower changed the flow direction or status between each other and the fluctuated wake made the blade has a transient vibration which will affect the measured results. Considering that the extra deflection reduces the thrust and the reduced thrust causes the reduced deflection, the values shown in this figure are the results of the balanced blade. The results of the flap-wise blade deflection could be very difficult to estimate in dynamic test as the major loading conditions applied to the blade are not static.

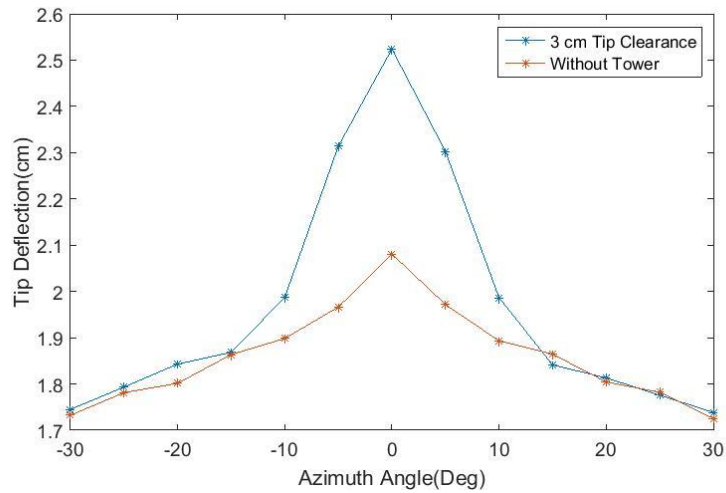


Figure 4.16 Static deflections at 60% wind speed.

As Figure 4.17 shown, the deflection of the blade increased with the decreasing tip clearance at the same wind speed when the tower was fully covered by the blade. And, the tip deflection would be lower than any tip clearance sets if there was no tower structure after the blade.

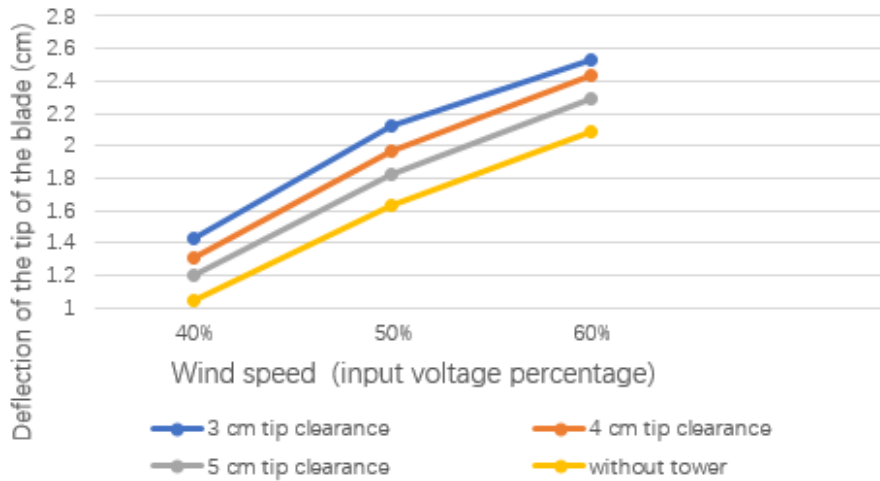


Figure 4.17 Deflections of the blade in vertical position in static test

4.5.2 Summary

The performance of the sensors was validated by the comparisons with the tube manometer. However, for measuring a greater range of the wind speed, the diameter of

the holes on the tower should be redesigned to improve the accuracy.

The results of this static test could help to understand the causes of the fluctuation of the total thrust on the entire system in practice. First, due to the different linear velocity for each point along the blade, the shadowing area in different positions of the tower starts and ends at different time for each rotation. Especially for the tidal turbine blade which has wider blade compared to the wind turbine, the corresponding blade-tower interactions have a greater impact on the overall structure. In addition, as the magnitude of pressure change on the tower is proportional to the flow speed, this variation will contribute to much more thrust fluctuation in higher load. Although the pressure variation on the tower might not be large enough to affect the vibration of the entire system in practice, but its influence on the rotor balance or the fatigue life of each blade is still unknown.

Secondly, the extra deflection of the blade due to smaller tip clearance at the same flow speed can also cause the greater degree of the pressure drops on the tower and thus increases the pressure difference. In dynamic condition, however, it can present a more complicated interaction, which means the static value of the blade deflection cannot be used to create a threshold to indicate the working status of the dynamic turbine blade. Based on this, there are two problems with the application of the strain gauge on the blade: 1, the performance of the sensors in long-term operation is uncertain. 2, the threshold of the blade deflection is rigorous enough to be established only by using the data of the static test of strain gauge. More importantly, the design of the blade is still early stage and any attached sensors will limit its design possibilities.

4.5.3 Dynamic Test

Although the tip deflection is the most intuitive way to indicate the status of the blade, the feasibility of the strain measurement on rotating blade is still in doubt. Besides the constantly changed wind profile, the edge-wise deflection caused by the rotation and gravity can also affect the results from the strain gauge. Figure 4.18 shows an example of the zoomed strain data which was calibrated to the tip deflection.

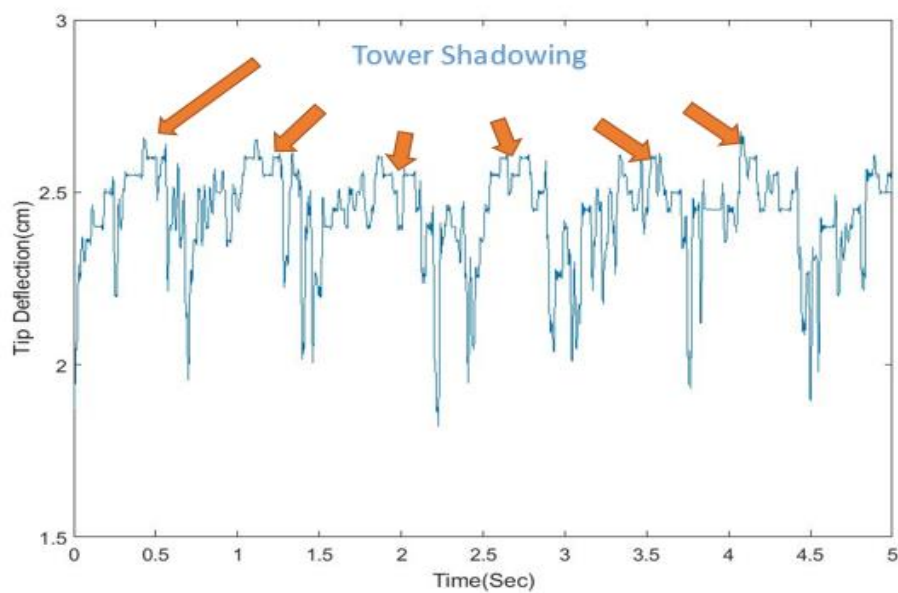


Figure 4.18 Tip deflection time series

The signal is synchronized with the starting position. As the rotational speed for the strain signal in Figure 4.19 is 12 RPM, the number of the crests is consistent with the fact that there should be 6 loops of the blade swing occurs within 5 seconds. By using the method of signal processing mentioned above, the overall trend of the averaged variation of the tip deflection is plotted in Figure 4.19 and the static one is plotted as well for comparison.

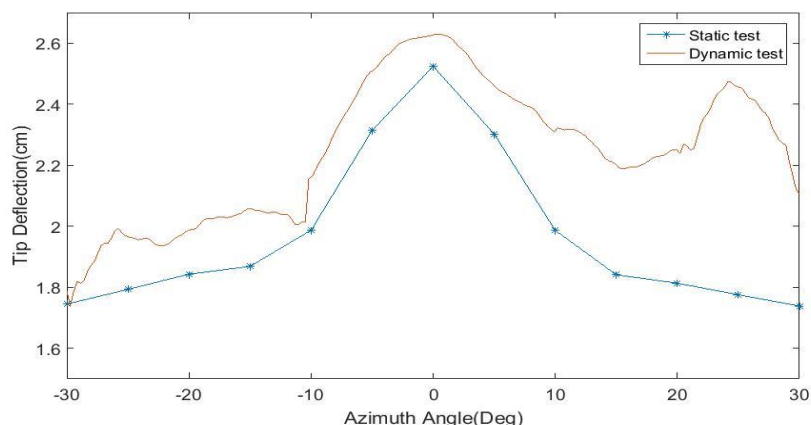


Figure 4.19 Comparison between the averaged static and dynamic tip deflection

In Figure 4.19, the dynamic tip deflection starts at the same level with the static one and then it becomes larger as the blade approaches the middle vertical position and the tower. After the complete passage through the tower, the blade still maintains a high deflection and even reaches to about 2.5 cm. As the deformation of the resistance coil of the strain gauge can be also affected by the edge-wise deflection, the torque from the servo motor leads to larger output voltage in the first 30 degrees. For next thirty degrees of rotation, however, there are two possible factors: 1, the always existed load variation on the blade makes the vibration of the blade in flap wise direction and this type of vibration becomes larger when the blade rotates away from the tower due to the blade-tower interaction. 2, the rotation and the gravity of the blade makes extra bending during the period. On the other hand, the deflection of each actual tidal turbine blade for one rotation can be affected by many factors include above. The variation of the edge-wise bending is inevitably mixed with the strain gauge output. Therefore, the dynamic measurement of strain gauge is not reliable for representing the operating status of the blade.

As described in the section of the experimental procedure, the pressure signals from PAW sensors during the clock-wise rotation in each cycle were selected to analyse. Every selected part is resampled with same data points and an average data is recreated to indicate the overall trend of the pressure variation on the tower at specific location. After this, 10 more pressure data sets with same sample rate are made to fill up each blank area between each two PAW sensors and the values of the data are linearly made between the two values from the adjacent PAW sensors. Therefore, there are 30 sets of extra data are made for each group. By using mesh function in MATLAB, an example of the pressure variation is visualized and represented as Figure 4.20 shown.

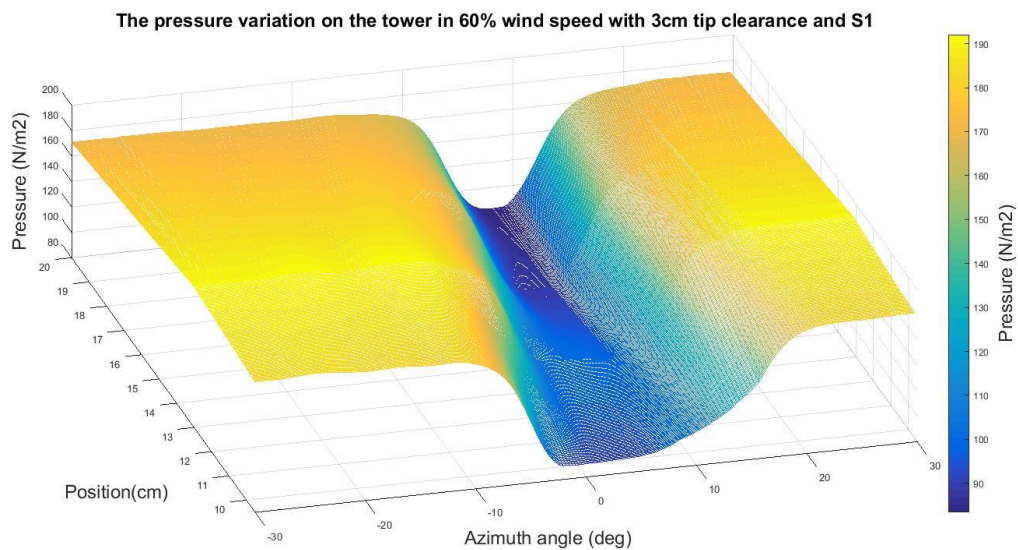


Figure 4.20 Example of the estimated flow profile

For further comparison and better viewing, the plot is rotated as Figure 4.21 shown. The top view of the 3D plot omitted the Z-axis but became more intuitive with the colour bar.

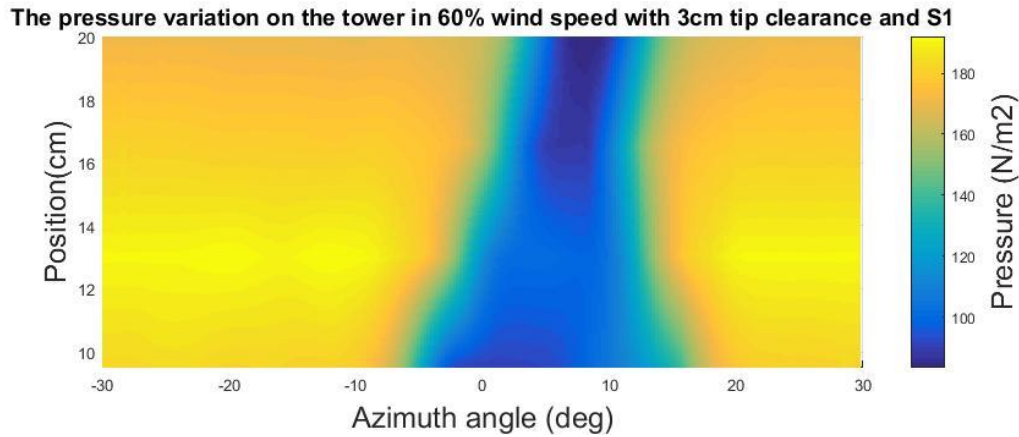


Figure 4.21 Top view of the mesh plot of the pressure variation in 60% wind speed with 1 and 3 cm tip clearance.

In Figure 4.21, the pressure at PAW1 started to change after the 0 degree (The vertical position of the blade) and pressure on the other positions all have different levels of delay due to the time of the wake travel to the tower. It is obvious that the relatively more blade coverage during the rotation at the height of the PAW4 caused more shadowing area than that at PAW1. The width of the shadowing area is reduced with different level from top to bottom is consistent with the fact that each part of the blade has the different linear velocity.

Figure 4.22 shows the pressure variation with different tip clearances in 40% wind speed and S1 rotational speed. The results have the similar shadowing area but occurred in different point. This is because of both the longer travel distance of the wake and varying degrees of pressure decay after the blade.

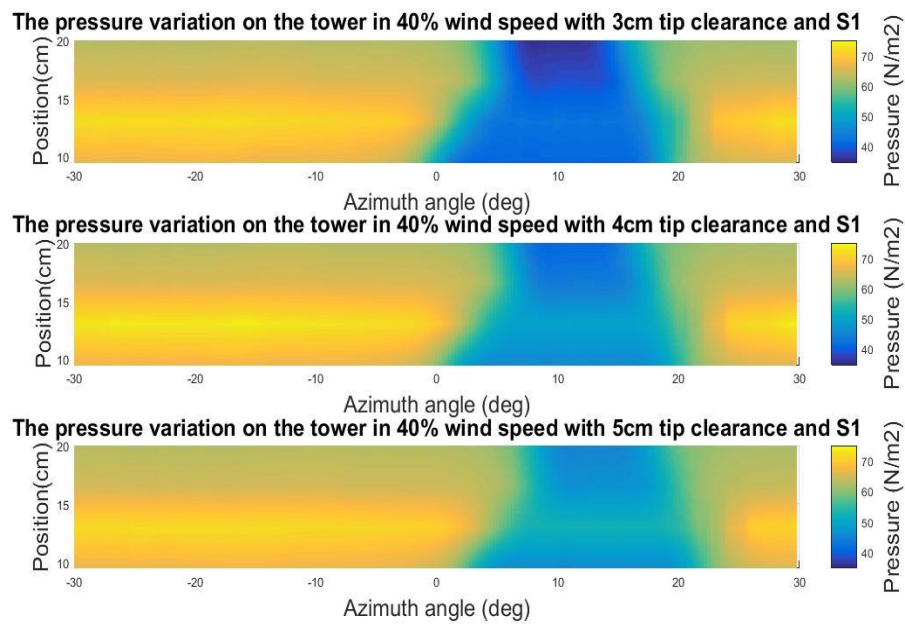


Figure 4.22 Comparison of the pressure variation between 3 cm, 4 cm and 5 cm tip clearances

By using the same colour bar, it is clearly observed that the lowest pressure is in the 3-cm tip clearance, which also means that the maximum blade deflection occurred in the set of the 3-cm tip clearance according to the conclusion of static test. Another comparison with the same rotational speed S1 and tip clearance 3 cm between different wind speeds is shown on Figure 4.23.

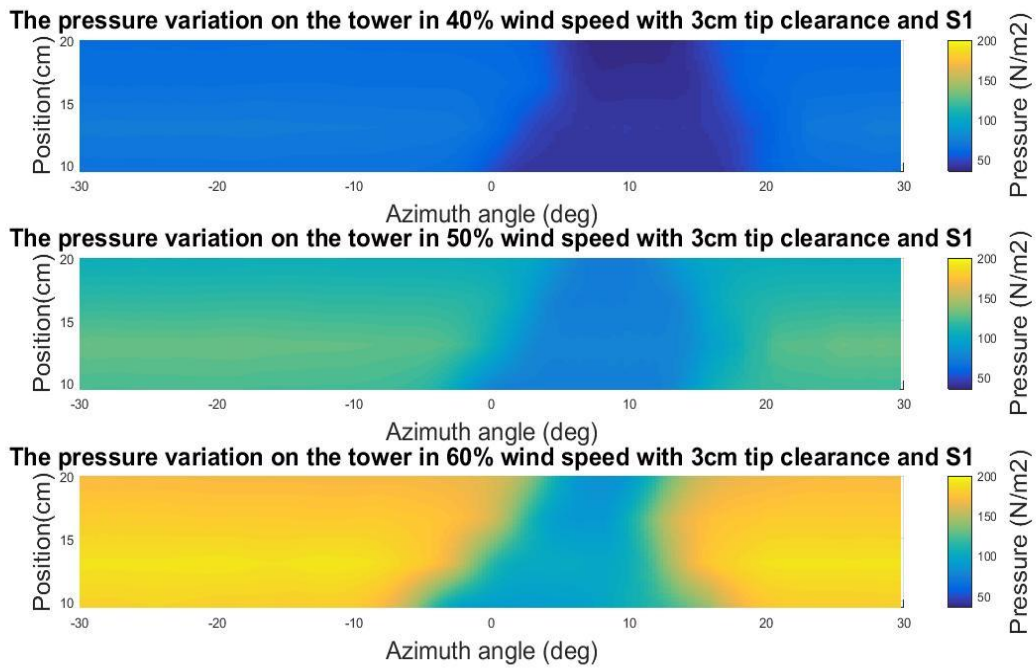


Figure 4.23 Comparison of the pressure variation in different wind speed

As the higher wind speed can reduce the time of the wake travel to the tower, the delay of the shadowing area in 60% wind speed is apparently smaller than it in 40% wind speed. And due to the same reason, the shape of the shadowing areas is also very different compared to each other. The result of this comparison also practically corroborated the one of the conclusions of static test that the starting and end point of the pressure change are based on the flow speed.

The next comparison, shown on Figure 4.24, is about how the different rotational speed affects the pressure variation at the same wind speed.

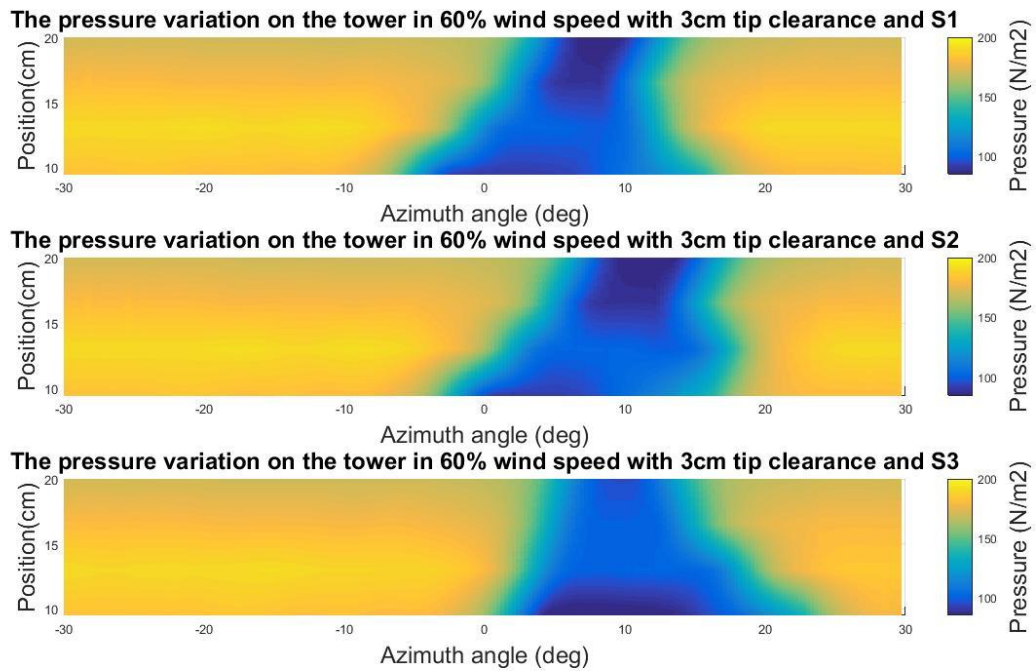


Figure 4.24 Pressure variation on the tower in 60% wind speed with different rotational speed.

The changes brought by the rotational speed of the blade are readily observed and mainly reflected in two aspects: 1, without any change of the blade, this can be understood as the time of the wake travel from the back of the blade to the tower is dramatically changed by the rotational speed. 2, the trend of the pressure change from each PAW sensor has no certain rules to be tracked. That means the shadowing area on the tidal turbine in practice could be specific based on the different flow profile.

The following comparison is between the default and wider tower under the same settings and one of the examples is shown on Figure 4.25. As expected the wider tower caused the bigger shadowing area with advanced start point and delayed end point.

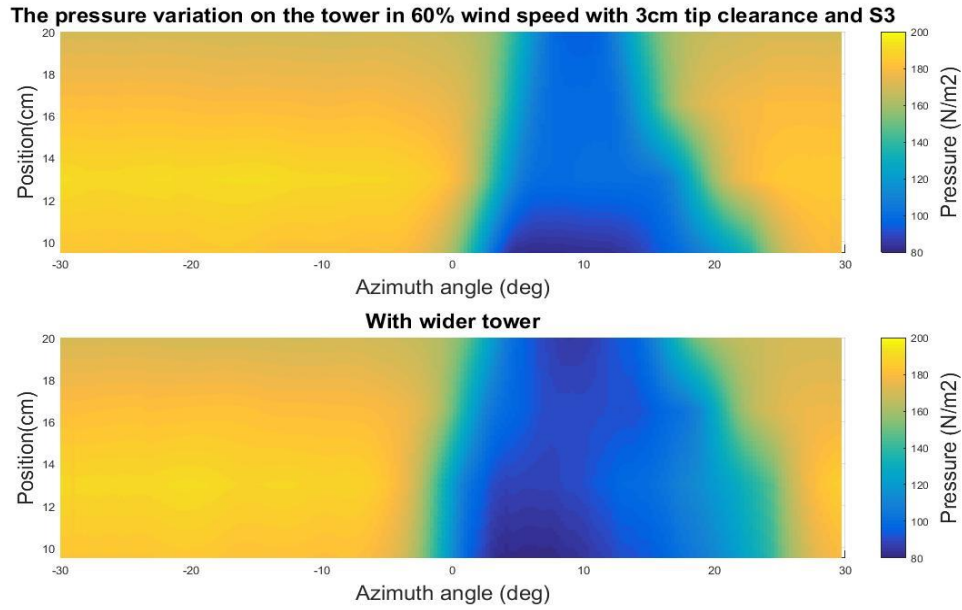


Figure 4.25 Pressure variation on the tower with different widths.

By using the same plotting method, the pressure variation caused by the Blade 1 with optimal condition and Failure 1 are respectively plotted in Figure 4.26.

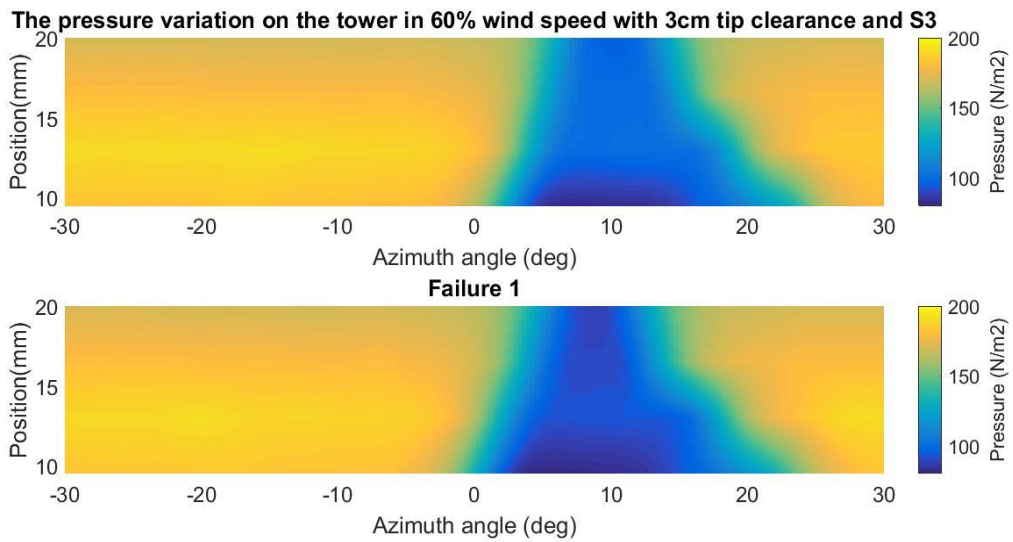


Figure 4.26 Comparison between the Optimal condition and Failure 1

The Failure 1 of the blade will cause the extra deflection of the blade due to the thinner blade. According to the results of the static test, the flap-wise deflection of the blade is inversely proportional to pressure on the tower. In Figure 4.26, the shape of

these two shadowing areas is similar but the pressure change is significantly different. This difference is obvious in the 3D drawing, but does not represent the real situation due to the data fill. Therefore, the pressure variation from the four PAW sensors is respectively shown in Figure 4.27.

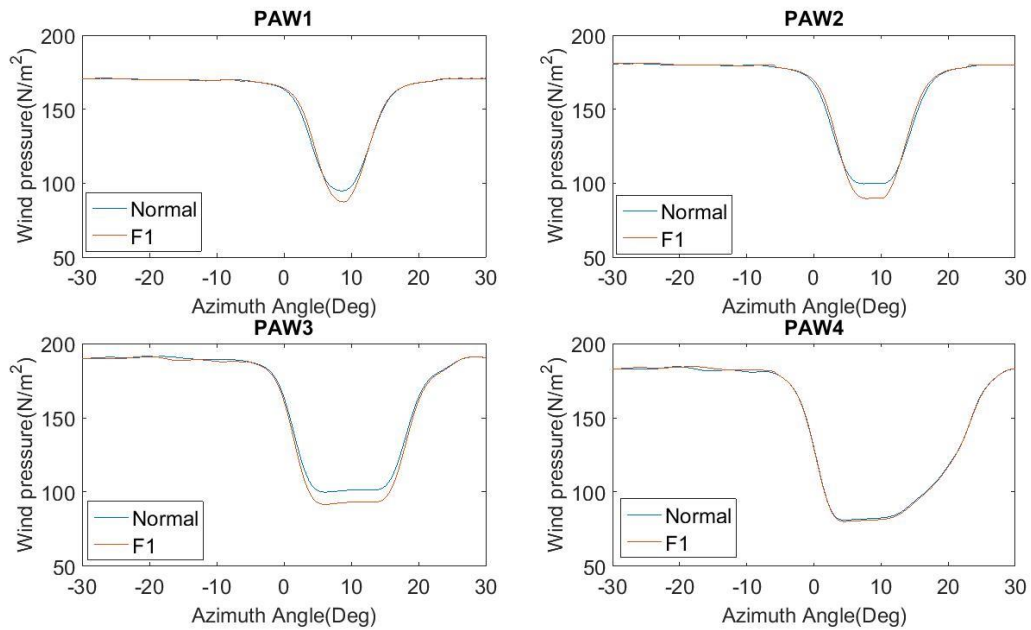


Figure 4.27 Pressure comparisons between Optimal and F1

The four graphs in Figure 4.27 indicate that the pressure drop of the Failure 1 group is greater than the optimal condition. That means the extra blade deflection caused by the thinned thickness is detected by the PAW sensors. Another example of comparison, shown in Figure 4.28, is between Failure 1 and Failure 1+2, because Failure 2 is directly made to the Blade 1 with Failure 1. Compared to Failure 2, the blade with Failure 1 even can be considered as a reference set.

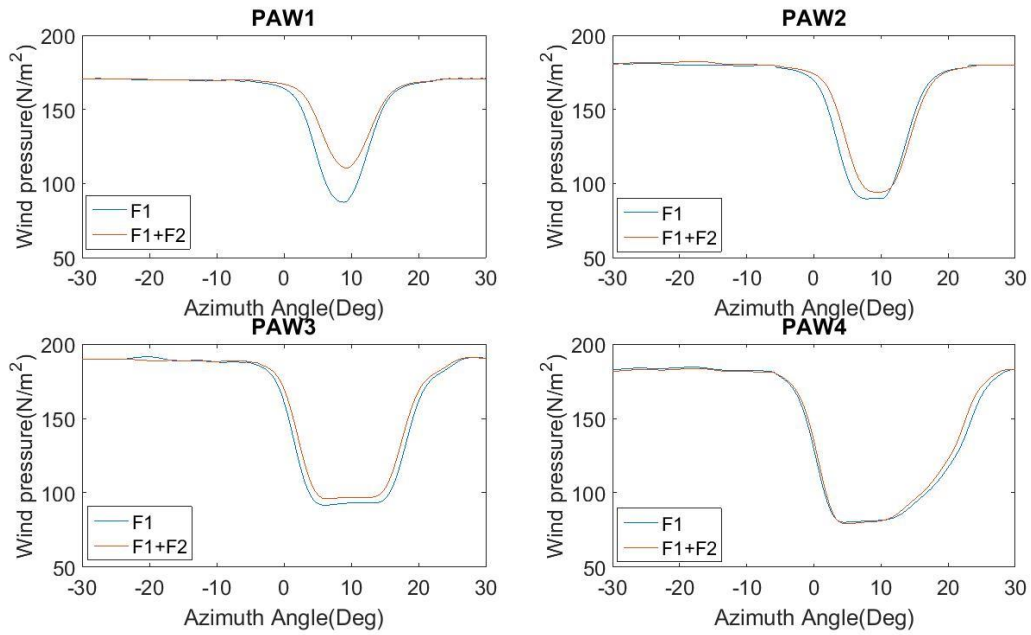


Figure 4.28 Pressure comparisons between F1 and F1+F2

Unlike the Failure 1, the lost part on the leading edge on the blade tip not only changed its geometry but reduced the total load on the blade. Due to the decreased total load, the deflection on the different position of the blade has decreased with different levels and the pressure on the tower should be increased during the blade passage. Meanwhile, the broken leading edge on the blade tip delayed the occurrence of the shadowing area, which is confirmed in the first graph. On the other hand, the broken tip didn't affect the total deflection due to the location of the breach.

Figure 4.29 shows the pressure comparison between the Failure 1+2 and Failure 1+2+3.

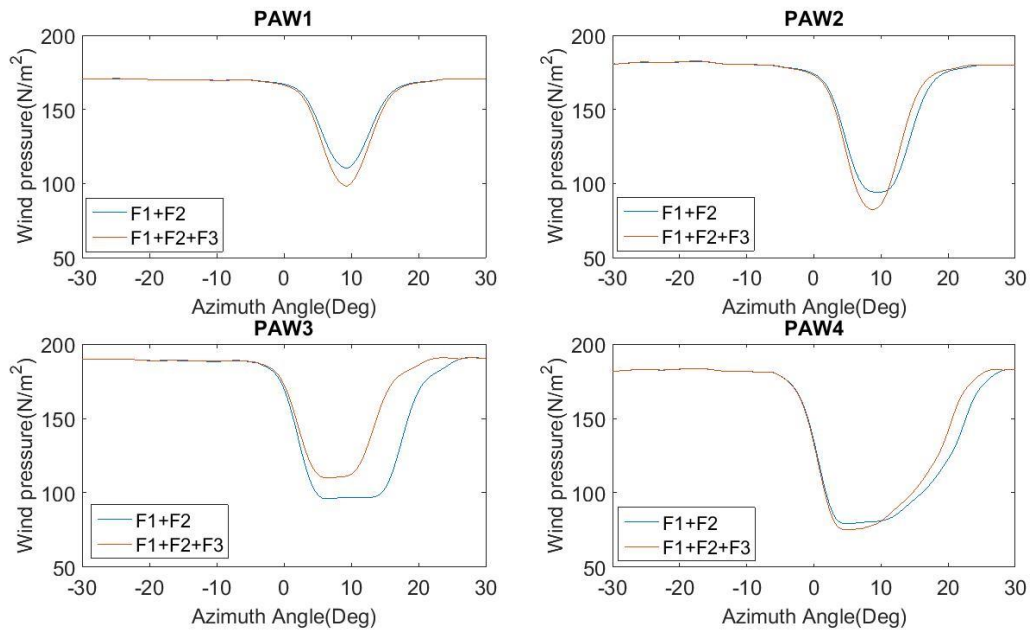


Figure 4.29 Pressure comparisons between F1+F2 and F1+F2+F3

The broken part was made on the trailing edge of the blade and very close to the PAW3. In addition to the load drop caused by the shape change, the bending performance of the blade were significantly reduced for the same reason, as the first two graphs in Figure 4.29 shown. The lost part on trailing edge on PAW3 position also led to a less shadowing area which represents less blade coverage on later half.

The last comparison is between the healthy Blade 1 and Blade 5, which is shown in Figure 4.30.

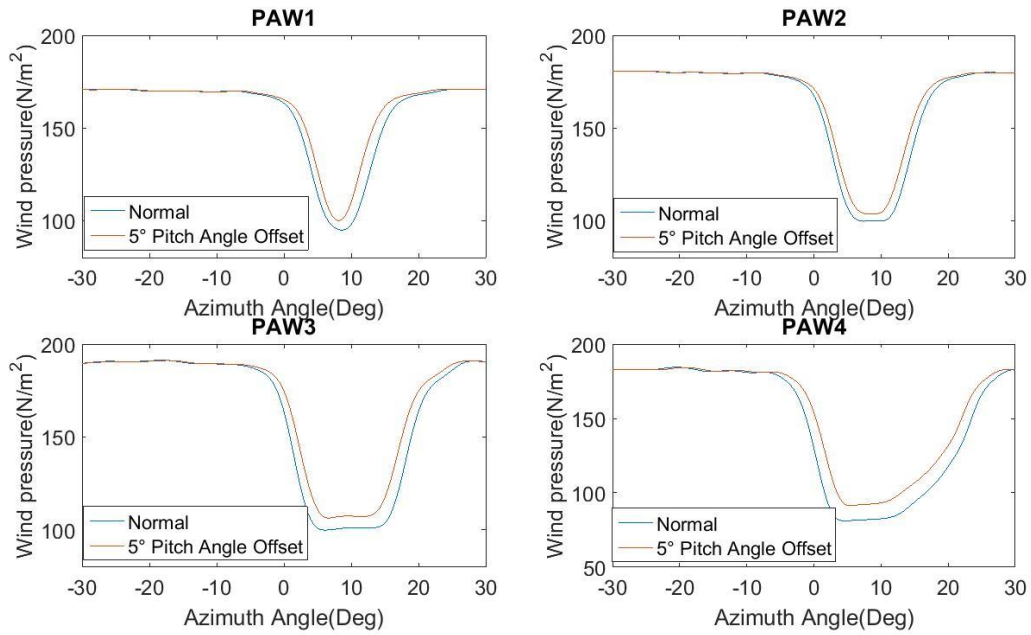


Figure 4.30 Pressure comparisons between Blade 1 and Blade 2

As expected, Blade 2 has narrow shadowing area due to both the less coverage area and the less total thrust. The relation between these two pressure variations is similar with that of the projections of these two blades, which means the larger projection has wider shadowing area.

4.5.4 Summary

Many comparisons between ‘reference’ blade and ‘offset’ blade above confirmed that any change of the blade or flow condition can be reflected in the pressure variation on the tower, especially in the PAW 1. In addition, the failures related to breach can be positioned by the rest of the PAW sensors. As each of the 3-D figures above are extracted and from the 4 sets of the wind pressure data, the reconstructed flow profile must have a certain degree of error compared to the practice (Wind profile power law cannot be used here as the test was conducted in the tunnel). The meaning of the 3-D plot is visualizing the difference of the pressure variation due to the change of the wind

speed, rotational speed, and tip clearance. The accuracy of the reconstructed flow pressure on the tower is determined by the number of the PAW sensors used.

However, for a rotating 3-bladed rotor with variable speed, it is impossible to directly do the comparisons as above. Differences in the comparisons above have two dimensions, which raises higher requirements for establishing the threshold. Each blade of the rotor could be slightly different due to change of its stiffness and strength caused by water absorption, which will bring the difficulty to build a unified and unchanging threshold to determine the change of the blade condition. Therefore, the main comparison should be done with the same blade rather than between the adjacent blades. For creating the method of processing the continuous pressure signal, a further simulation work is needed.

5. Pressure Signal Simulation and Blade Health Monitoring System

This chapter introduces modelling work and analysis method of pressure signals from the pressure sensors installed on the tower. A series datasets of continuous pressure signals were made by combining the experimental data with and without blade passing. Some trapezoidal waveforms were chosen as training datasets to conduct the duty cycle analysis and frequency domain analysis for a better understanding of the pressure signals. The amplitude and initial phase angle at blade passage frequency was analysed and the overlap processing of signals from PAW2, PAW3 and PAW4 was introduced for identifying the specific blade failure. Finally, by combining the analysis methods above, a comprehensive and reliable diagnostic tool is designed for specific failures. A validation of the proposed blade health monitoring system was presented at the end.

5.1 Pressure Signal Simulation

As stated in Chapter 4 that the continuous rotation of the blade mounted inside the wind tunnel cross-section was not possible due to the maximised length of the scale blade, the pressure signals are obtained from the blade passing cycle of 60° rather than a rotation of 3-bladed rotor with tower. For simulating the operation of a rotating 3-bladed TST, each 360° rotation includes the 3 segments of pressure signal when shadowing is in effect and the other 3 segments of signal which is measured without blade in front. A detailed procedure of the signal simulation is given in following

section.

5.1.1 Method of Simulation

In physical experiments (Chapter 4), a flow pressure test lasts 90 seconds was made before the servo motor starts to operate and a series of pressure signals without blade passing for each wind speed setting was recorded. Due to the effects of the turbulence inside the wind tunnel, the flow pressure shows the random fluctuations within a certain range. The raw pressure signals (without blade passing) are divided into several signal segments with required number of points. The pressure signal obtained from the test with blade passing, after the resampling in Section 4.4.2, are also divided into the several segments with same number of points according to the rotational speed. The procedure of stitching the two signals as Figure 5.1 shown.

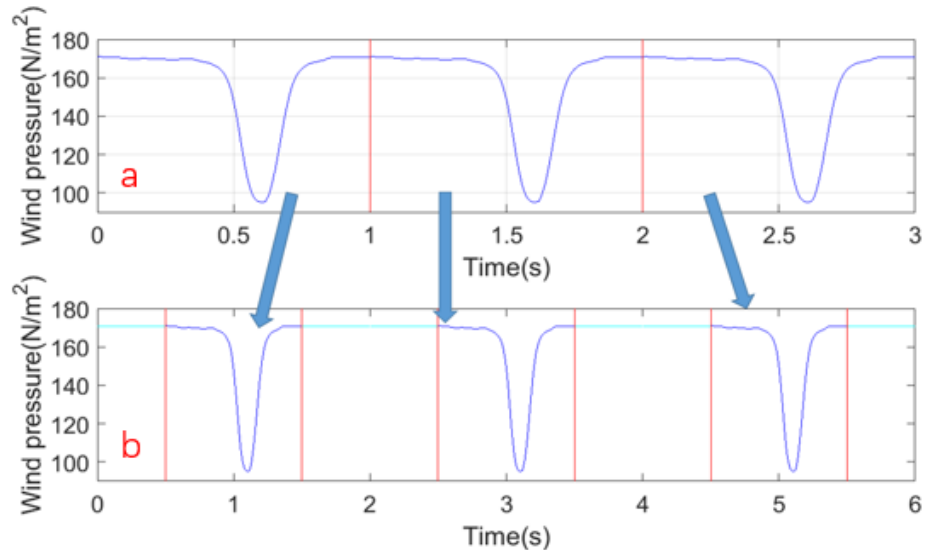


Figure 5.1 Procedure of the pressure signal simulation for one rotation. a) shows the experimental data from Chapter 4; b) shows the simulated pressure signal.

The signal above in Figure 5.1 is from results of No.1 PAW sensor in the test conducted with reference blade in 60% wind speed and 10 RPM rotational speed (600

data points in total for this three shadowing parts within 3 seconds). The blue parts present the flow pressure without blade in front. According to the rotational speed of the test, the numbers of data points for the four segments are respectively 100, 200, 200 and 100 from left to right. The simulated signal in Figure 5.1(b) presents the pressure variation on the tower for a single rotation of the rotor. Note that the one or more pressure signal segments can be shifted by any previous physical experiment data of different sets but the number of data points should be strictly set by the rotational speed of the test.

5.1.2 Simulation with Different Scenarios

Based on the experiments in Chapter 4, there are 4 types of blade failures are listed and prepared for the signal simulation. To start with, the data from PAW1 are used to simulate the continuous pressure signal and detect the existence of the failures since all types of failures contribute more tip deflection on the blade tip. Next, the data from PAW2, PAW3 and PAW4 are used to distinguish and diagnose these four typical failures and the simulations are made as Table 5.1 shown.

Table 5-1 Simulation of the estimated pressure signals from PAW1

No.	Blade 1	Blade 2	Blade 3	Signal Name
1	Reference	Reference	Reference	SN
2	Reference	Reference	Failure 1	SF1,
3	Reference	Reference	Failure 2	SF2
4	Reference	Reference	Failure 3	SF3
5	Reference	Reference	Failure 4	SF4
6	Reference	Failure 1	Failure 1	SF1F2
7	Reference	Failure 1	Failure 4	SF1F4
8	Failure 1	Failure 2	Failure 4	SF1F2F4
<p>Notes: Failure 1 is Stiffness and Strength Deterioration. Failure 2 is Broken Blade Tip</p> <p>Failure 3 is Broken Middle Section Failure 4 is Pitch Angle offset with 5°</p>				

Note: The number of the simulated signal on the right shows the possible situations of the failure(s) in different blade.

The signal of No.1 group in Table 5.1 is composed of three pressure variation segments from the healthy blade and is used as the reference. The groups from No.2 to No.5 are the cases of the specific failure in single blade and the failures could be in any blade. The No.5 and No.6 groups respectively represents the same failures and different failures occurred in two blades.

Although the movement trajectory can be estimated by the obtained logical signal from LabVIEW, the synchronization of blade position and pressure variation on the tower may not to be achieved on current full scale tidal turbine. As Section 5.1.1

described, the initial point and the number of data points for each signal segment are ideally set by the information of the blade position. To simplify the description, the system to achieve this synchronization is temporarily called Blade Positioning system (BPs). The following two sections will respectively discuss the analytical methods for the pressure signals with and without BPs.

5.2 Analysis with Blade Position

By assuming that BPs can provide the information of the blade position, the pressure signal could be obtained accurately starts from the point ahead of the Blade 1 with 30° azimuth angle as the proposed simulation procedure. The error caused by the procedure of signal resampling will be therefore reduced.

The shape of the simulated pressure signal is very similar to the upside-down cosine squared (raised cosine) pulse with relatively high duty cycle, the analysis of some cases about the trapezoidal wave and square wave is necessary to be made for better understanding. First, the duty cycle of a pulsing signal is defined as the ratio between the pulse duration. For the simulated pressure signal, the ‘pulse’ and ‘duration’ can be respectively seemed as pressure without blade passing and the blade shadowing time. Second, the frequency domain analysis of the exemplified pulsing wave is needed due to its periodicity.

5.2.1 Duty Cycle Analysis

To start with, four trapezoidal waveforms are created as Figure 5.2 shown. The parts with 1 and -1 amplitudes are normally defined as ‘Positive’ and ‘Negative’. The 1st and 2nd trapezoidal waveforms have same fall and rise times and different duty cycle. And,

the 2nd and 3rd trapezoidal waveforms have same ‘Negative’ time and different ‘Positive’ time. The 3rd and 4th have the same fall and rise times but the former has the ‘raised SIN’ rising and falling edge. In addition, the 1st and 4th have same ‘Positive’ time and different ‘Negative’ time. All waveforms are created with same frequency and amplitude. The trapezoidal waveforms 1-4 are simplified as TW1-4.

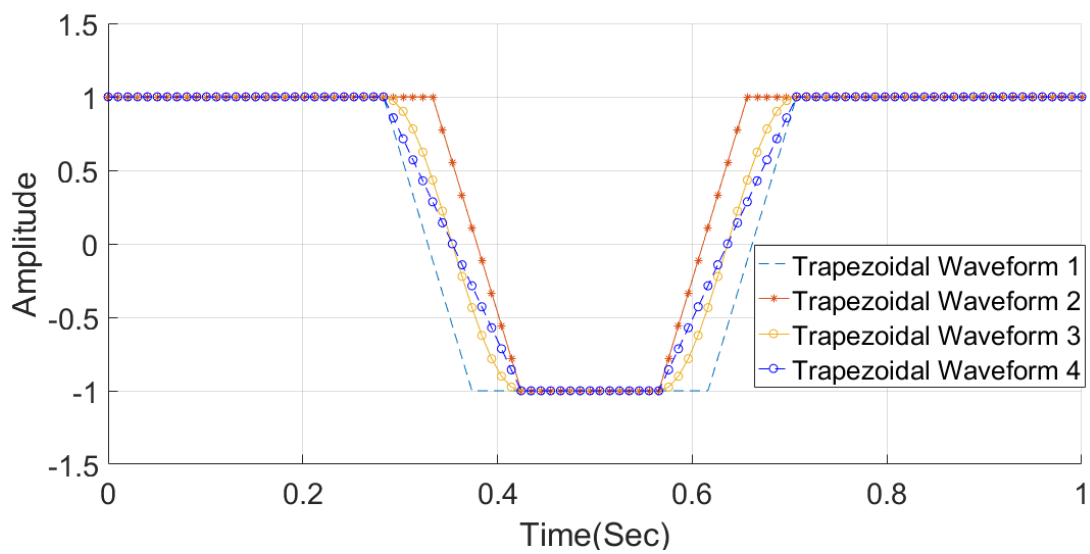


Figure 5.2 Simulated trapezoidal waveforms

Unlike the square waveform, there are various ways to define the pulse width of trapezoidal waveform such as width at half-max, or the time for which the signal is flat. In the MATLAB function of Duty Cycle, the default calculation of pulse width is based on the State-Level Tolerances which is used to define the state boundaries for both ‘Positive’ and ‘Negative’. The lower- and upper-state boundaries for each state are calculated by setting the scalar multiple of the difference between the high state and the low state. Figure 5.3 shows the example of the State-Level definition with 0.2 tolerance.

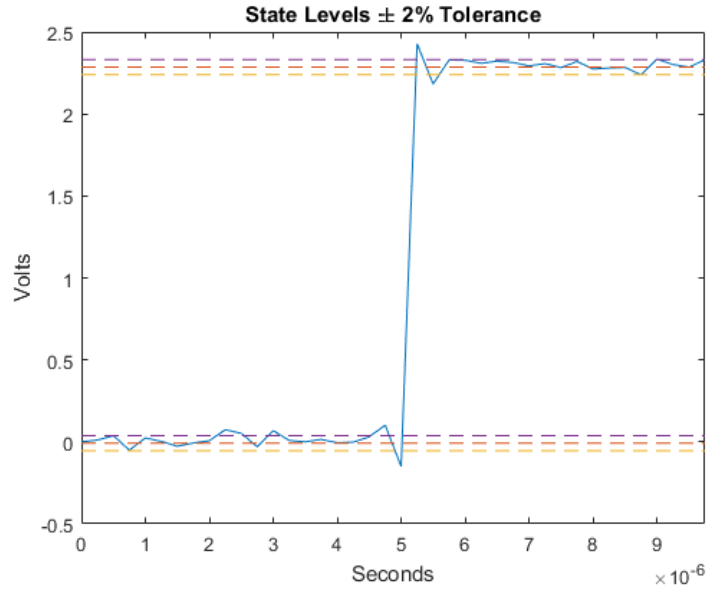


Figure 5.3 State levels estimation of the trapezoidal wave

The tolerance region is expressed as,

$$S_1 \pm \alpha(S_2 - S_1) \text{ (For Low State)} \quad (5.1)$$

$$S_2 \pm \alpha(S_2 - S_1) \text{ (For High State)} \quad (5.2)$$

Where,

S_1 is the low-state level,

S_2 is the high-state level,

α is the scalar multiple of the difference between the high state and the low state.

Figure 5.4 shows the simulated the trapezoidal wave 1 and 2 with 10 cycles. The values, which are shown in the right table, are the duty cycles calculated by MATLAB.

The obtained duty cycles series are same for a simulated wave as each pulse is identical.

The duty cycle of TW2 is higher than that of TW1 as expected.

hand, as the constant values of the pulse are same, other State-Level Tolerances will not affect the results.

As for the simulated pressure signal, the SN and SF1 are made according to Section 5.1.1 and the pressure variation on the tower for one turbine revolution with 10 RPM in 60% wind speed are shown in Figure 5.6. In this case, due to the reduced thickness of the blade, the blade is more vulnerable to bending deformation. With extra bending, the reduced distance between the tower and blade can lead to the pressure drop as observed.

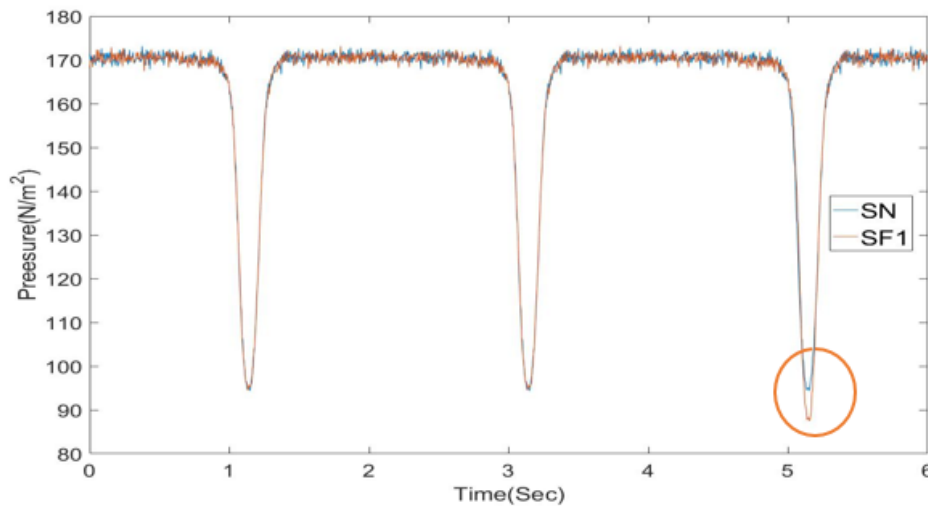


Figure 5.6 Comparison between SN and SF1

The time-vary duty cycles of SN and SF1 were shown in Figure 5.7 with 89 data points calculated from 30 turbine revolutions (One has been ignored by the function). Due to the turbulence in wind tunnel used, the duty cycles of SN are fluctuating in a certain range. With the same Y axis range, it is clear to see that the SF1 has much more fluctuation for its duty cycles than SN1 due to the Failure 1 on the Blade 3. Note that the data points of the calculated duty cycles within a certain period are directly

determined by the rotational speed.

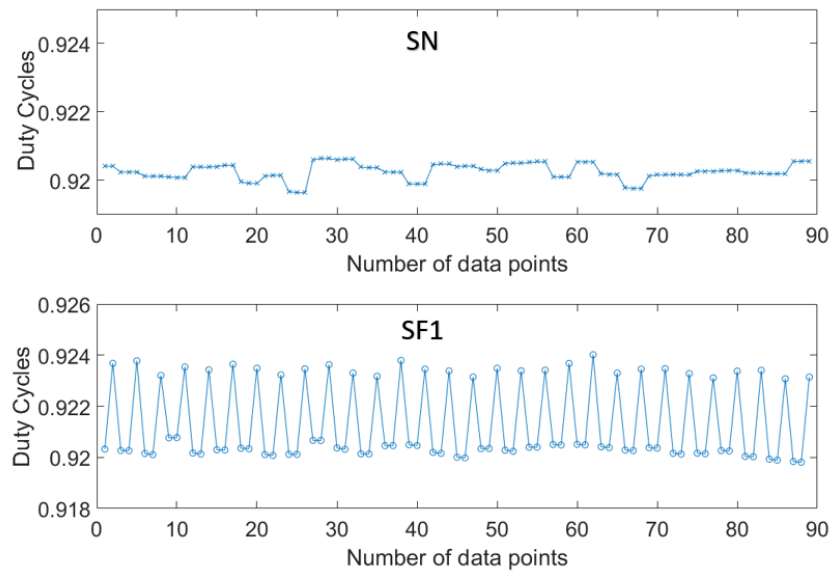


Figure 5.7 Duty cycles of the SN and SF1

Since both the rotational frequency and sample rate are known, the frequency of the calculated duty cycles is 0.5 Hz for this case. It seems that this is possible to create the threshold of amplitude in specific frequency for initially detecting the failure (not diagnose). In practice, however, the faulty blade could affect the rotational speed of the TST, which means the number of duty cycles for optimal and faulty rotors could be different. For example, the number of duty cycles for SF1 can be 83 instead of 89 but its fluctuation will still exist. As the duty cycles are expected to be a similar value, therefore, calculating the variance is more intuitive way to distinguish the difference between the healthy and faulty rotor blades for a given wind speed. The practical turbine blades may also have subtle differences, which means the corresponding pressure variation caused by blade passing will be different within a certain range. The threshold of the variance should be determined according to the data of the full-scale test in long term. In this case, the variances of SN and SF1 are respectively 3.5011×10^{-7} and

22.771×10^{-7} . By using the same method, the variance of the duty cycles of SF1F4 (No.7) which has two of the rotor blades are subject to different failures is calculated as 469.28×10^{-7} .

5.2.2 Initial Phase Angle Analysis

By using Fast Fourier Transform (FFT) function with the MATLAB environment, the spectrums for each set in Table 5.1 are plotted to find the differences among the groups. As the one-dimensional data, the amplitudes in the fundamental wave and the harmonics cannot be used to reflect the multiple changes (pulse width, time and edge of raise & fall, 'Negative' value and starting point of the pressure drop). Therefore, it is necessary to extract more information from the spectrums to help analyses the simulated pressure signal.

Before analyzing the pressure signal, the four trapezoidal waveforms 1-4 are used again for understanding. Figure 5.8 shows the zoomed FFT results of the four trapezoidal waveforms. As the signal are simulated with 10000 samples within 100 seconds, the peak amplitudes can be observed at 1 Hz as expected.

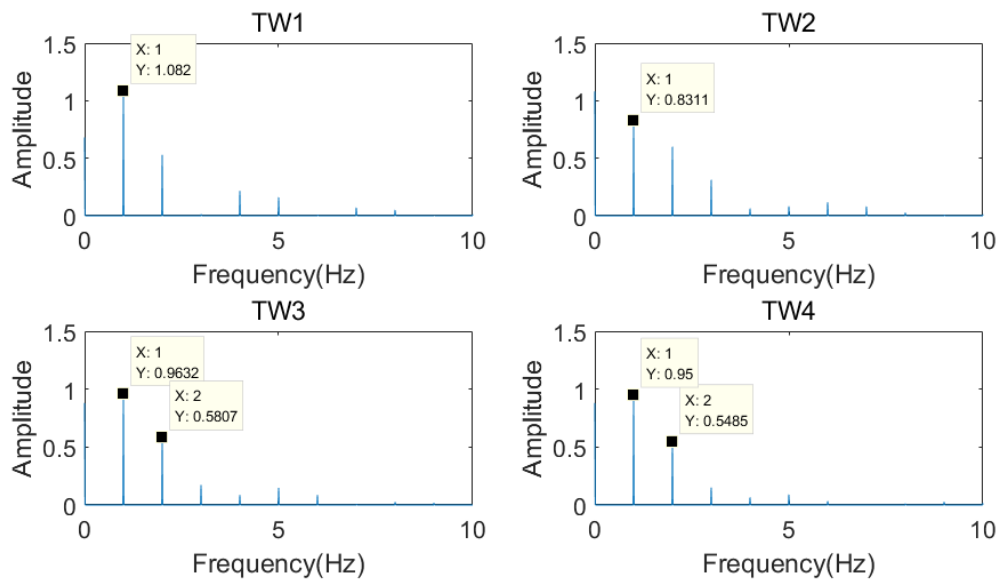


Figure 5.8 Frequency spectrums of the simulated trapezoidal waveforms

With the same ‘Negative’ and ‘Positive’ values, the differences of peak amplitudes in this comparison are influenced by both the pulse width and rise & fall times and edge shape. The comparison between TW1 and TW2 shows that peak amplitude increases as the duty cycle decreases. And, the comparison between TW3 and TW4 represents that the rise & fall edges would slightly affect the amplitude at 1 Hz compare to its difference between TW1 and TW2.

Before processing the simulated pressure signal, another example is necessary to be made for finding the trends in change of the blade 3 with different failures in frequency spectrum. A normal trapezoidal wave is made for presenting the reference blade. Some other trapezoidal waves are made with the characteristics of the different failures. By using the method in Section 5.1.1, the segment for blade 3 can be switched by any other offset trapezoidal waves. Figure 5.9 shows the FFT plots of the exemplified signals which has 9000 samples and 100 Hz sample rate. Note that the value of pulse is 1.

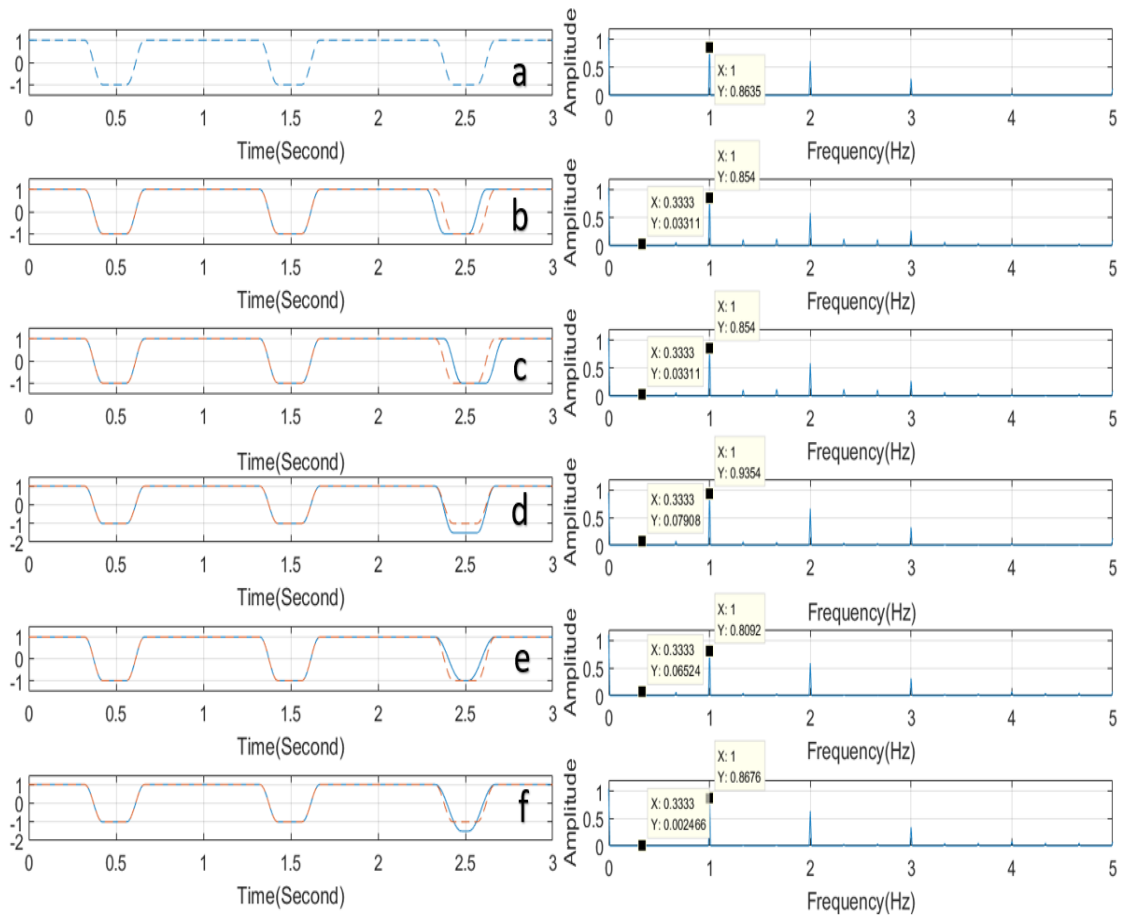


Figure 5.9 Simulated trapezoidal waves and corresponding frequency spectrums

Figure 5.9(a) shows the zoomed pressure variation for the operation of 3 assumed reference blade in one turbine revolution. The frequency of the blade passage can be observed at 1 Hz (marked as ω) as expected. Figure 5.9 (b) and Figure 5.9(c) show the optimal waves with an advanced gap and a delayed gap. The frequency of the blade 3 passing in front of the tower can be observed at 0.3333 (marked as $\frac{1}{3} * \omega$) which is one-third of the blade passing frequency and equal to rotational frequency. It is also found that the amplitudes of both Figure 5.9(b) and Figure 5.9(c) are same at corresponding frequency. Therefore, the advanced or delayed gap with same ‘Negative’ time doesn’t affect the result of the FFT if their gap width is same. In Figure 5.9(d), Figure 5.9(e) and Figure 5.9(f), the amplitude at $\frac{1}{3} * \omega$ still can be observed as expected. In (d), the

peak amplitude increases due to the deeper gap. In Figure 5.19 (e), although the ‘Negative’ value is same as the optimal wave, the peak amplitude decreases as the gap becomes narrower. In Figure 5.19 (f), the amplitude at $\frac{1}{3} * \omega$ does not increase because of the deepening and narrowing of the gap. Moreover, the amplitude at ω doesn’t change too much compared to above. Therefore, these comparisons once again demonstrate that multiple changes cannot be reflected in the amplitude values.

Based on the comparisons above, one scenario that the reference blade 3 starts to have Failure 1 at 90 seconds of 180 operation time is simulated by the pressure data as the Figure 5.10 shown.

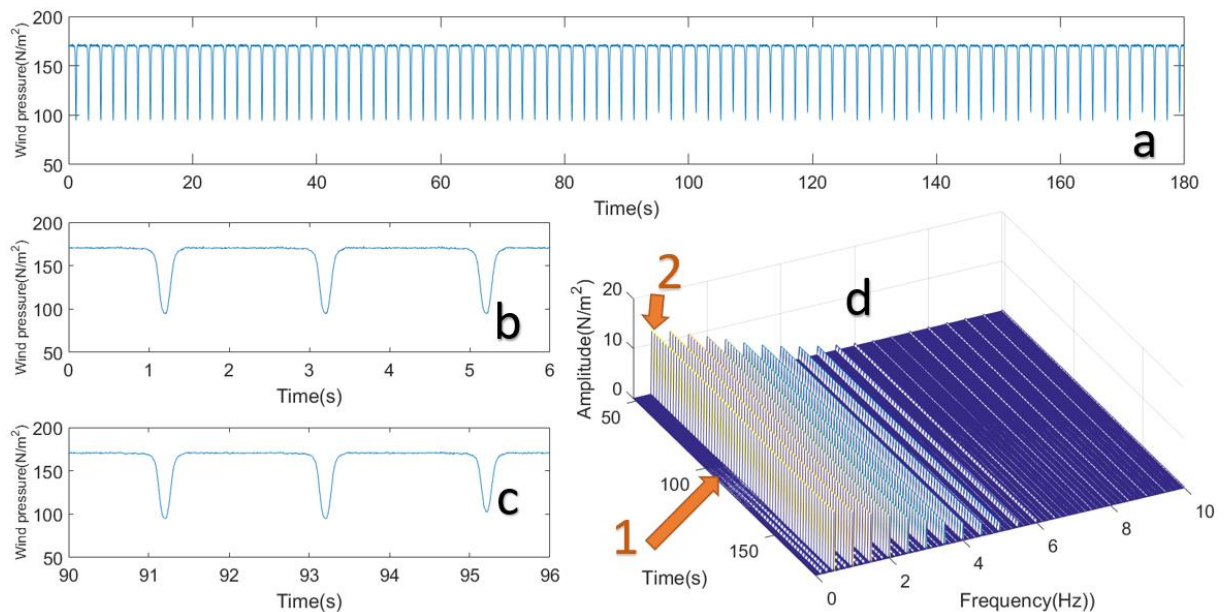


Figure 5.10 Simulation of the occurrence of Failure 1 on Blade 3; a) is the simulated signal in 180 seconds; b) is the zoomed signal of one rotation of 3 reference blades in first 6 seconds; c) is the zoomed signal of one rotation of 2 reference blades and 1 faulty blade in from 90 to 96 second; d) is the zoomed waterfall plot of the frequency

spectrums.

There are many harmonics can be observed as the duty cycles of the signal is relatively high. The mark 1 in Figure 5.10 shows that occurrence of the frequencies at $\frac{1}{3} * \omega$ and $\frac{2}{3} * \omega$. That means the faulty Blade 3 is detected. The mark 2 shows the amplitude at ω decreases because of the failure occurs at 90 second, which cannot be clearly seen from this angle of viewing.

As for the simulated pressure signals from Table 5.1, they will be more complicated due to the fluctuated flow pressure. For a given rotational frequency ω , the peak amplitude of pressure spectrums for the simulated 3 healthy blades should be always at ω as expected. Figure 5.11 shows fundamental wave and the first 11 harmonics extracted from SN.

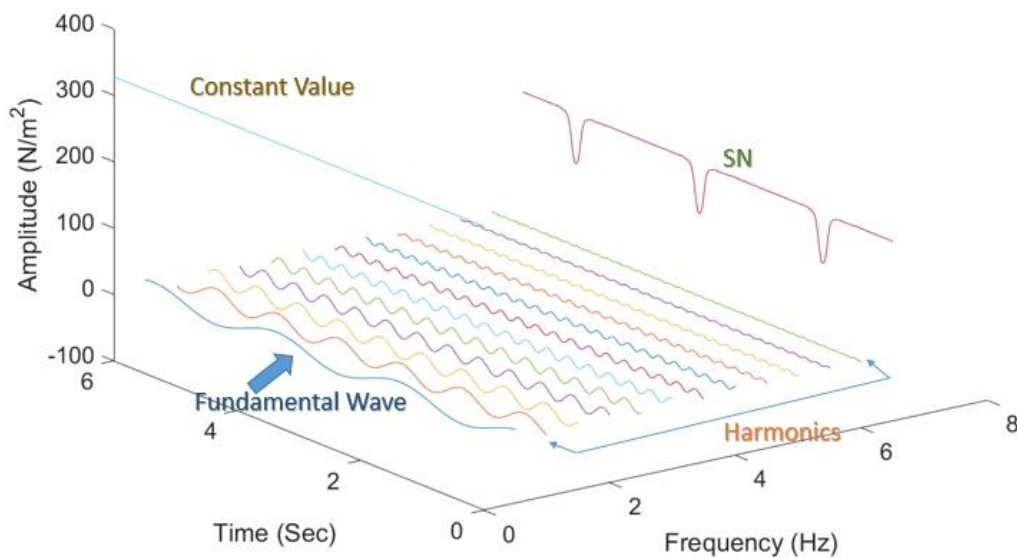


Figure 5.11 Fourier decomposition of the simulated pressure signal SN.

Since all simulated signals accurately start from a specific point after resampling, the initial phase angle of the wave with blade passing frequency ω varies as the amplitude.

Therefore, the first attempt is made for the SN and SF1. As their only difference is the condition of Blade 3, 9 more pressure values between SN and SF1 have been evenly obtained as Figure 5.12 shown. The purpose is to simulate the deterioration procedure of the Failure 1 on Blade 3.

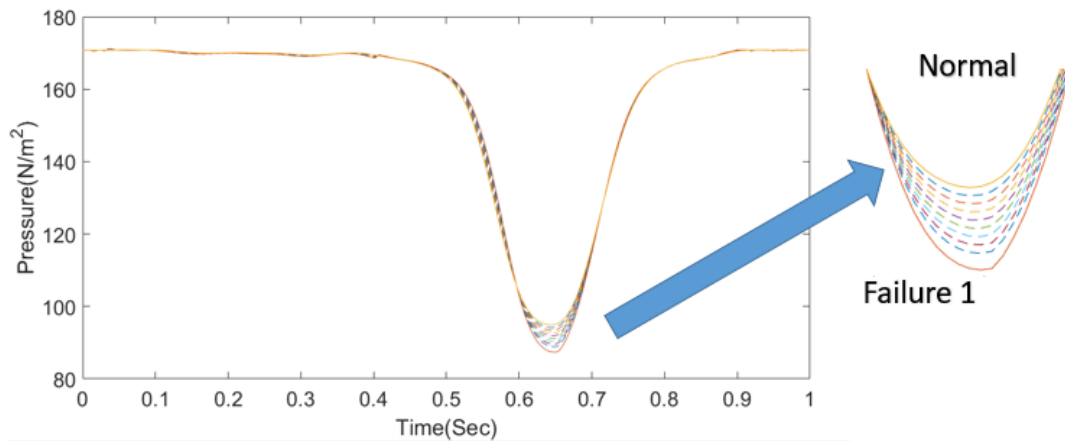


Figure 5.12 Extra simulated pressure signals between SN and SF1

The extra simulated signals replace the segment of the Blade 3 and the corresponding continuous pressure signal are marked from S1 to S9. After FFT, their amplitudes and initial phases angle of the wave at ω are obtained as Figure 5.13 shown. The figure is called the Pase-Angle (P-A) curve.

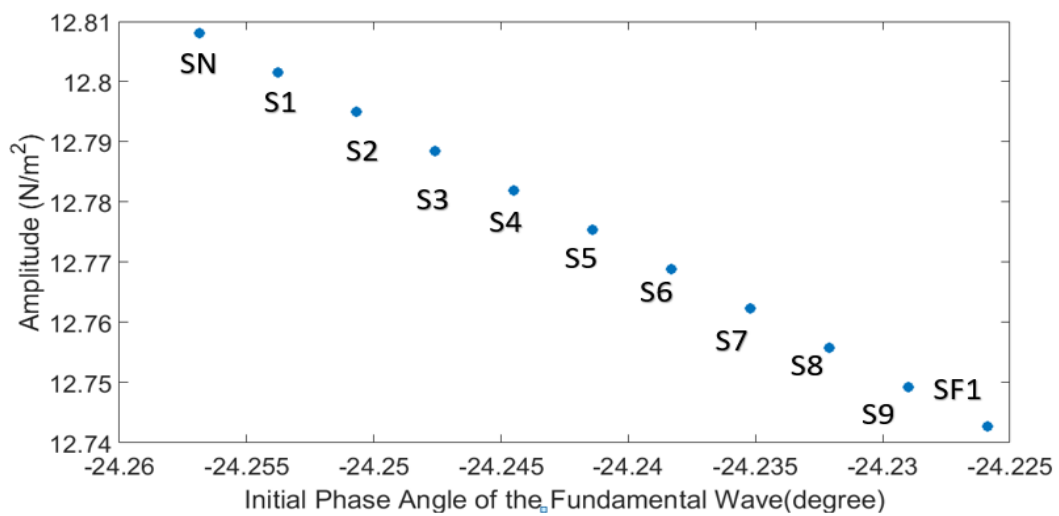


Figure 5.13 P-A curve from SN to SF1

As the deterioration of the Blade 3, the initial phase angle of the fundamental wave increases and the corresponding amplitude decrease. However, this linear relationship can only be described the change from SN to SF1. By using the same method, the 8 groups of the simulated signal are processed and the completed P-A curves for these four failures are plotted in Figure 5.14.

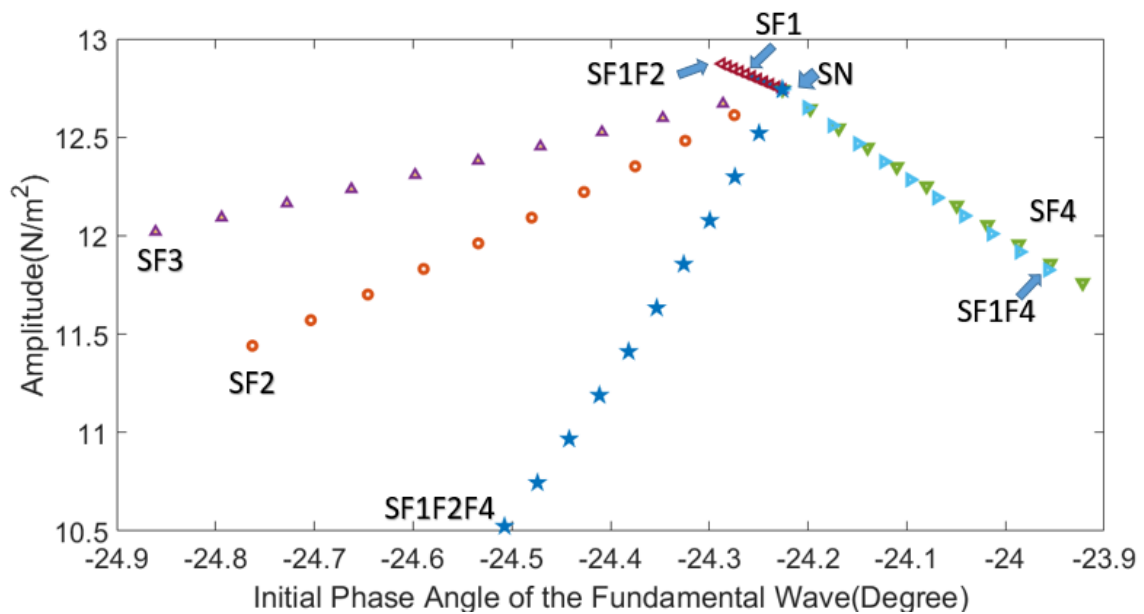


Figure 5.14 Complete P-A curves

According to the results of the complete P-A curves, the threshold can be set to an area around the SN point shown above. Since the blade tip can reflect the most deflection caused by the failures or Blade-Tower interaction, all the data used for simulating the groups of the pressure signals in Table 5.1 are from PAW1. As mentioned in Section 5.1.1, the Failure 2 is the breach on the blade tip and the following accumulated Failure 3 and 4 also contains the impact of the former. Therefore, the first comparison should be done with single faulty blade. From SF1 to SF2, these two P-A

curves tend to the two completely different directions. Moreover, the added Failure 3 (breach on the middle of the blade) on Blade 3 doesn't change too much in the P-A curve compared to the difference between SF1 and SF2. This is because the Failure 3 indirectly change the wake behind the blade tip by the blade deflection and the changed shape of the blade tip (Failure 2) can bring more direct changes for the pressure variation on the closest point of the tower. Although the blade used in the physical experiments (Chapter 4) is flat, the shape and roughness of the surface will also affect the pressure changes to a large extent. The SF4, which the Blade 3 has 5° pitch angle offset, tends to another direction.

On the other hand, not every fault can be directly identified by only use the P-A curves. For example, if the broken middle section (Failure 3) occurred as an independent issue, the initial phase angle and amplitude at ω Hz might be within the assumed threshold area above. Therefore, there are two things need to be emphasized: 1, the P-A curves in Figure 5.14 is only used as rough reference, as each previous failure is retained by the faulty blade with next failure except Failure 1 and Failure 4 (Individually applied on another blade). 2, the data from PAW2 to PAW4 are as important as PAW1 for further failure diagnosis. For simplifying the establishment of a failure threshold for data from these three PAW sensors, another method is proposed in following section.

5.2.3 Overlap

Once the failures have been detected by an optimized P-A figure of PAW1 in practice, the signal of PAW2, PAW3 and PAW3 would be used to identify the problems. Owing

to the Blade Positioning system (BPs), the pressure signals can be evenly divided into the fragments which can individually presents the pressure variation with 120 degrees of the rotation. The difference between the former and latter segments can be recorded as a new signal segment and plotted as Figure 5.15 shown. (60% Wind speed, 10 PRM and 200 Hz sample rate)

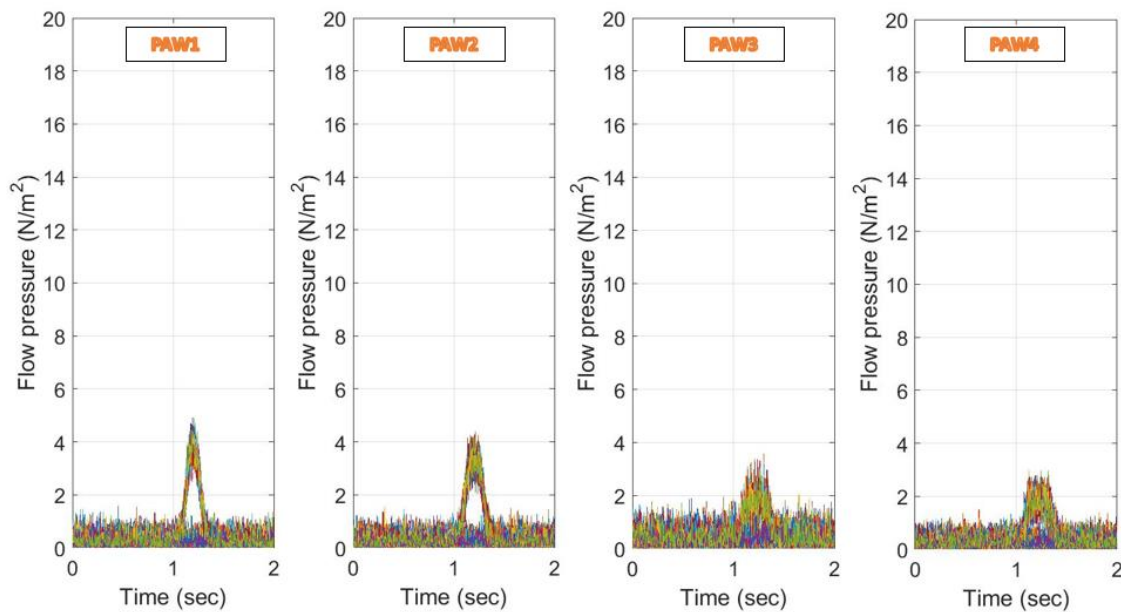


Figure 5.15 Overlap of the pressure difference between Reference and Failure 1

In Figure 5.15, the raised part of the overlapped segments shows the degree of change between the normal operation and Failure 1. From top to the bottom of the blade, the degree is gradually reduced as the biggest deflection occurred on the blade tip. As any types of the blade change in shape or property will eventually reflect in the pressure on the tower, the overlap results can both visually and quantifiably represent this unevenly distributed deflection along the blade.

There is another overlap result from the simulated signal that Failure 1 on the first two blades and Failure 2 on the third blade is shown in Figure 5.16. In this comparison,

the first two blades are deemed as reference condition as the Failure 2 is directly applied on the faulty blade with Failure 1. Compared to Figure 5.15, the extremely high value of some signal segments in leftmost graph of Figure 5.16 caused the abnormal gradient of the peaks from PAW4 to PAW1.

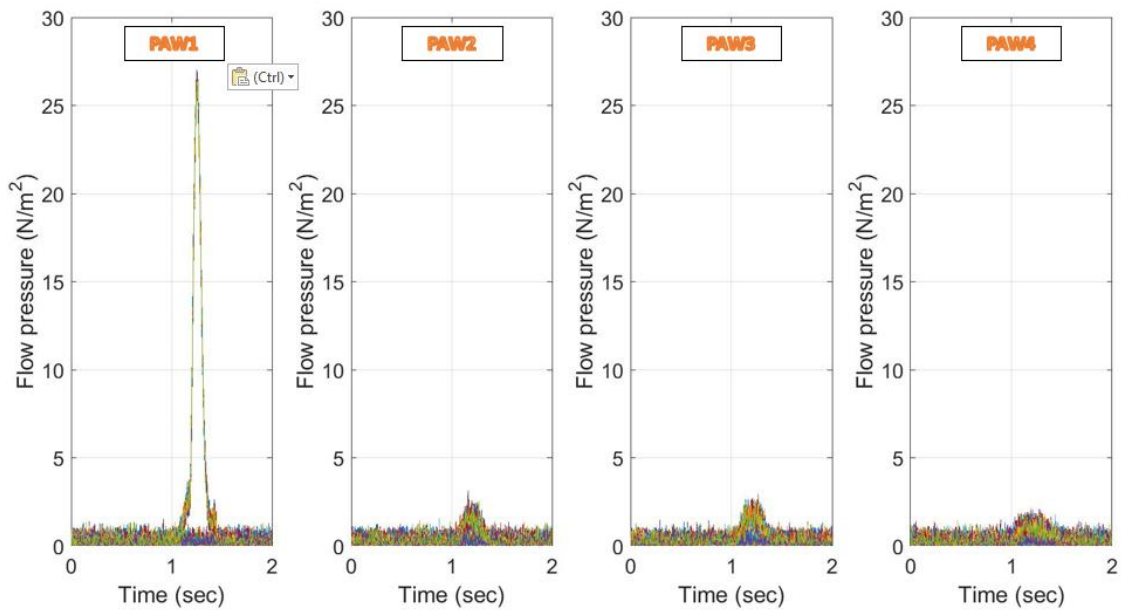


Figure 5.16 Overlap of the pressure differences between Failure 1 and Failure 2

This confirmed the breach on the blade tip changes the shape and level of the shadowing area behind but doesn't have much impact on the deflection of the below part of the blade. Another example, which is from the simulated signal that Failure 2 on the first two blades and Failure 3 on the third blade, is shown in Figure 5.17.

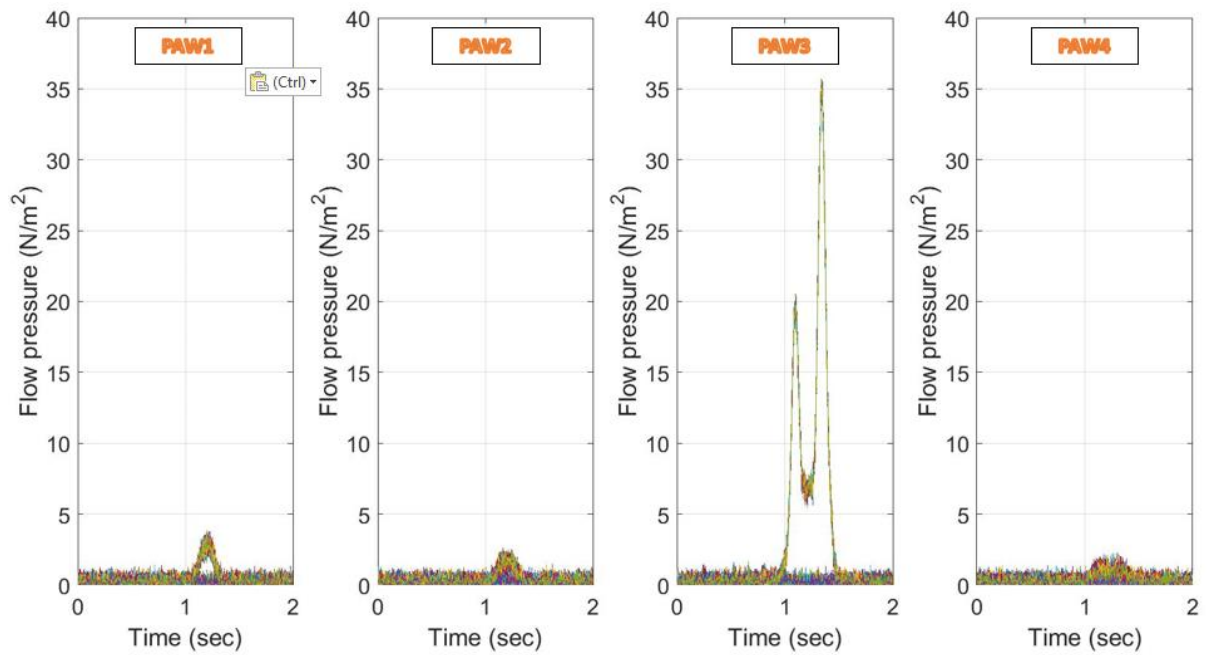


Figure 5.17 Overlap of the pressure differences between Failure 2 and Failure 3

In this case, again, the first two blades are deemed as reference condition as the Failure 3 is directly applied on the faulty blade with Failure 2. The double peaks in the overlapped PAW3 signal indicates changes of the shadowing area brought by the breach on the middle of the blade. In addition, the second peak proved that the location of the breach is on the trailing edge.

By combining the analytical methods above, a logical order of proposed blade health monitoring system is summarised as Figure 5.18 shown.

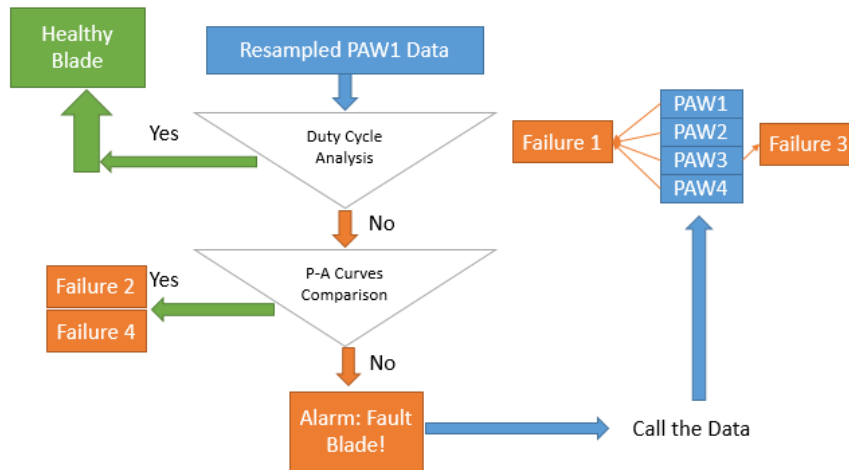


Figure 5.18 Logical diagram of the proposed BHM system

The detailed working principle is listed below:

1, the data from PAW1 is preferentially selected to calculate its duty cycle and the blade status can be initially estimated. If the variance of the duty cycles is within threshold, that means the 3 blades are operating well. Otherwise, the one or more blades must exist some error or failures.

2, the P-A curves is then used to initially identify failures like Failure 2 or 4 due to their influence. The Alarm can automatically report the error level according to the previously set P-A threshold area.

3, the data of PAW2-4 are used for locating and finally diagnosing some specific blade failures especially occurred between the tip and root.

4, During the procedure of the monitoring, the flow profile is very important to determine whether a piece of signal is available for data analysis. The higher turbulence will affect the credibility of the results from the proposed monitoring system.

5.3 The Analysis without Blade Position

The prerequisite for implementing the analytical methods above is that the starting point of the Blade 1 can be accurately located. Without the blade positioning system, however, the initial phase angle of the fundamental wave is no longer a meaningful value for establishing the threshold area as above. Therefore, an algorithm of repositioning the starting point of the simulated signal is established to solve this problem.

In this case, the synchronous logical signal will not be used as the BPS to find the starting point of the Blade 1, which means that the obtained pressure signal could be simulated as Figure 5.19(b) shown. They are all simulated as 30 turbine rotations and the time range is set to 0-6 seconds for better viewing. The simulated pressure signal, shown in Figure 5.19(b), starts from a random point located in the shadowing area of an unknown blade.

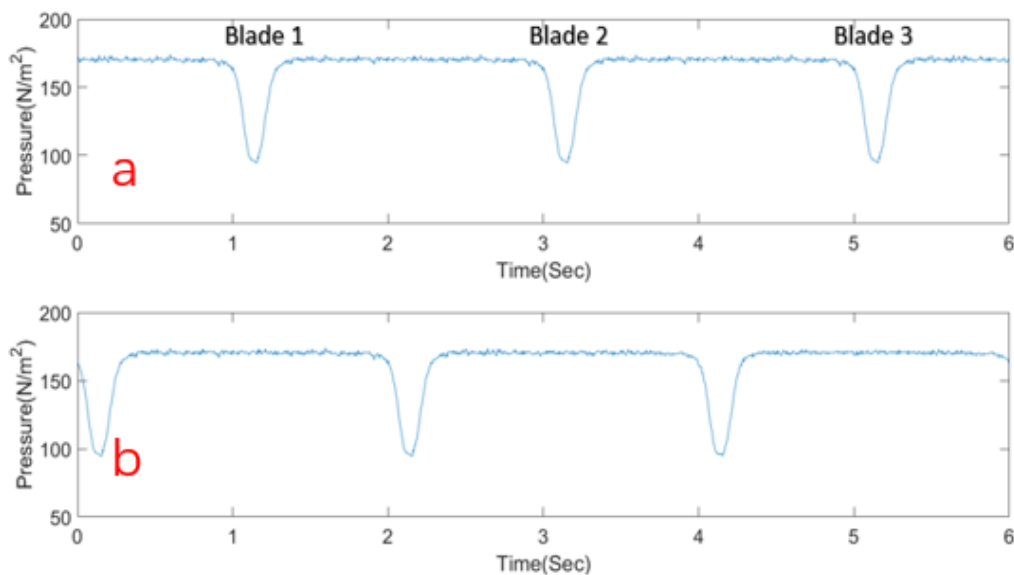


Figure 5.19 Comparison between the simulated pressure signal with and without blade

position

Inspired by State-Level Tolerances in MATLAB, the proposed algorithm needs a lower boundary which is as close as possible up to lowest point of the slightly fluctuated flow pressure. In this case, this boundary is set as a vector contains of 36,000 identical constants 164.5. By comparing the corresponding elements of each of the two signals, a new logical signal was obtained as Figure 5.20 shown.

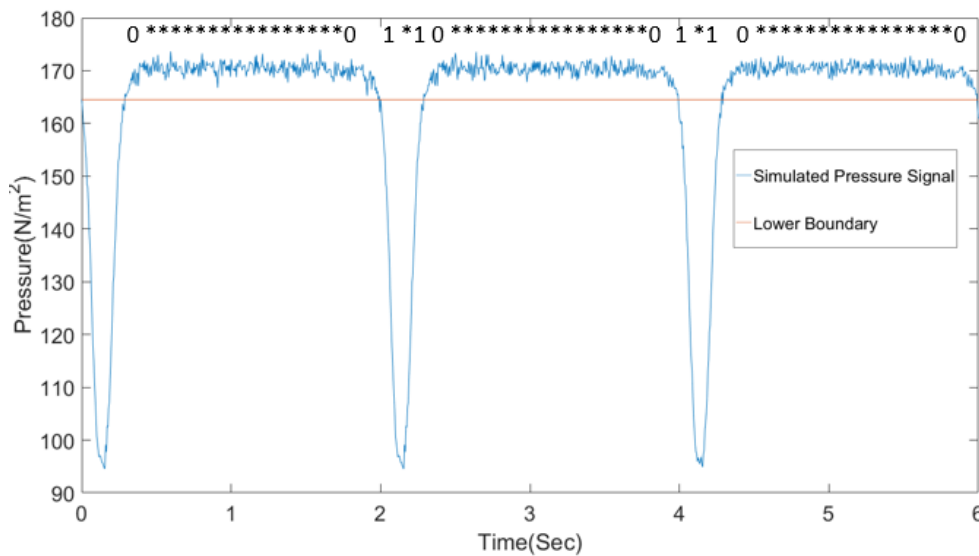


Figure 5.20 Generation of the logical signal

First, the generated logical signal above is used to re-select the starting point of the signal. Note that the new simulated pressure signal in this case should contain 29 turbine rotations instead of 30. Discarding the signal segments of 1 turbine rotation is to ensure the integrity of the simulated pressure signal. Next, resampling each signal segment by using the processed logical signal. Further, collecting the initial phase angle and amplitude of the fundamental wave in each data set to create new P-A curves. Figure 5.21 shows the flow chart of the pressure signal processing.

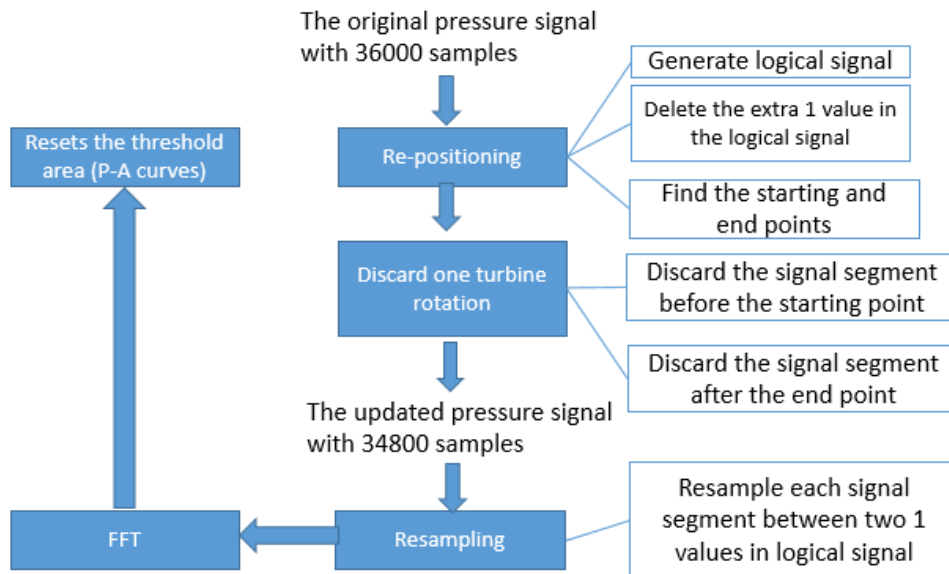


Figure 5.21 Procedure of the pressure signal processing without blade position signal

After the procedure above, the previous diagnosis methods can be used for analysing the processed pressure signal.

5.4 Summary

All the analytical methods above are feasible with a premise that the rotational speed is relatively stable in any certain wind speed. Once all blades were pitched to different angle for better energy extraction at a given flow speed, the P-A curves should be reset due to the changed TSR. Therefore, this problem can be solved by either creating more P-A curves for wider flow speed range or by insuring that the signal is only sampled at some specific flow rates. In addition, the wrongly yawing tidal turbine will not only reduce the accuracy of the measurement results of the PAW sensor but cause the fluctuation of the rotational speed. The proposed BHMs cannot therefore function effectively within this scenario.

The larger fluctuation of the duty cycle values, caused by the blade failure, is only

visually identified. The failure occurred on the single blade can affect two values of duty cycle to the extent of uncertainty and the interaction of two failures is more difficult to be diagnosed. More importantly, the method of calculating duty cycle in MATLAB ignores the rise & fall edge of the simulated pressure signal, which makes the calculation error becomes larger. This is the biggest reason that the duty cycle analysis is only used to detect the failures instead of diagnosing the specific failures. In practice, the fracture is common in the blade tip instead of middle body. The Failure 3 simulated above is only used to reflect the necessity of the overlap method. In extreme cases, the blade tip is completely broken and there is little or no pressure variation on PAW1 of the tower. The number of the obtained duty cycles of the pressure signal can directly diagnose this problem.

Last but not the least, the pressure compensation should be applied on each sensor to improve the accuracy of the measurements due to the vertical arrangement of the sensor under the sea.

6. Discussion

The research discussed in this chapter has the main aim of establishing the potential for a structure-based condition monitoring system for TST. The first objective of the research presented in Chapter 3 was to increase the understanding of the dynamic behaviour of the TST structure under different structural attribute assumptions and flow conditions. The second objective presented in Chapter 4 was the establishment of a viable method for flow measurement. In this application, this required that the flow profile measurement for the wind tunnel was achieved by using the PAW sensors. In-depth considerations about the application of the pressure sensors are discussed in this chapter. Following the proof of concept relating to the capability of the PAW sensors more suggestions for the design and application of CM algorithms are given. The objective was to demonstrate the potential of this approach to enable TST blade faults detection and classification under different operating scenarios. This was achieved by combining the results from Chapter 4 and Chapter 5.

The above aim and objectives can be best set against the consideration of the main features of the three sets of physical experiments in the wind tunnel and the simulation work for modelling the operation of the 3-bladed TST. This is presented in the following sections.

6.1 Wind Tunnel

The three sets of experiments which form the basis of this research were all conducted in the wind tunnel. The feasibility of using a wind tunnel to study the problems of TST was based on the known similarity between the hydrodynamics of

water and air. The major benefit in adopting this approach is related to the relative ease with which experimentation may be undertaken within the wind tunnel environment. Previous flume or tow tank based experimental investigations may be considered to present real challenges in terms of the operating environment (being under water) in which they are undertaken. This will result in experiments being performed within flow regimes that can be much more complicated and under much more challenging environmental conditions. Based on the experience of the experiments for this thesis, the advantages of the wind tunnel testing for researching the development of CM approaches for TST can be identified as:

- The cost and difficulty in operation of the wind tunnel is much less than water flume or tow tank testing.
- The required controllable, repeatable and steady flow conditions can be achieved with the use of flow conditioning (using honeycombs for example) or with the deployment of a specially designed smaller pressurised tunnel structure.
- The flow measurement and characterisation for the wind tunnel is much more straightforward and convenient. The options for the appropriate measurement method are both lower cost and more available.
- More extensive and flexible elements or complete models of the TST can be tested at a smaller scale. This not only reduces the cost but also improves the ease and efficiency of the part modification.

- Hydrodynamic influences associated with some design parameters of the TST structure can be predicted by analysing the aerodynamic behaviour of the models in the wind tunnel.
- The insulation environment available within the wind tunnel allows electronic equipment and sensors to be better protected during the test.
- With appropriate and safe operation and good installation the TST and/or element under test will not be damaged by wind force.

In order to assure that these advantages could be fully exploited there were wind tunnel related factors that needed to be considered during the setting up of the test program. The first consideration was that the input voltage of the fan motor did not follow a linear relationship with the generated wind speed. This required careful calibration and consideration when planning the different experiments. In order to make these plans it was important that the most suitable wind speed range for testing the different parts or models should be selected according to the specific test requirements. For instance, to undertake the vibration-based tests such as those reported in Chapter 2, the input voltage of the wind tunnel was controlled within 60% to prevent the vibration interference arising from the wind tunnel fan motor.

According to the previous experience from the water flume test, the structure-based test is not convenient to be conducted in the water tank. Although the underwater sensors are currently available and have good performance, the safe installation, good long-term performance and easy dismount still cannot be guaranteed. The wind tunnel

experiments conducted in this thesis are based on some similar properties and equations of water and air in fluid mechanics. First important similarity is that the principle of the pressure measurement for airflow and waterflow is same. Secondly, the Reynolds number equation can be applied to both medium, which means the acquired pressure or vibration results are reliable. Therefore, the body of work presented in this research does justify the initial assertion that, in terms of engineering condition monitoring techniques for application to a TST the application of the wind tunnel can provide a cost-effective, safe and reliable platform. This can be utilised for further developments, especially for the testing of various sensing principles and/or structural performance. In this research the wind tunnel set up has been used to successfully prove the feasibility of PAW sensors. The investigation of the occurrence of the known interactions between the rotating blades and the TST tower have been confirmed and achieved by use of the wind tunnel. In this way it was possible to link this research with previous research that utilised scale model turbines in a flume or tow tank and to CFD based simulations. By establishing this link, it was then possible to develop blade condition monitoring techniques that utilised this ability to replicate known phenomena in the wind tunnel experimental set up. This in turn enabled the design and manufacture of small scale but accurate 3-D printed parts and structures at low cost. The manufactured blades were then used for all the experiments in this thesis. This reduced the time and cost for manufacture and enabled very effective modification, including the manufacture of faulty blades. This has great potential as the relationship between turbine performance and blade condition is of critical importance and the ability to replicate such faults

would be a significant contribution for future wind tunnel experiments with the more advanced 3-D technology.

6.2 Vibration-based Investigation on Blade Failures Of TST

The research investigating the vibration-based behaviour of the TST models associated with faulty blade and yaw error was presented in Chapter 3. The two experiments in this chapter are mainly used to provide a good reference for the proposed flow profile and blade health monitoring method developed and applied in Chapter 4. The understanding of these experiments was based on the simplification of the WT or HATT structure which was presented in Section 2.3.2.

6.2.1 Experiment 1

The initial experimental investigation highlighted the influence of the flow pressure on the TST structure. The chord length of the blade and the tower or tower diameter of a TST are typically designed to be relatively greater than those of a WT with same rated power. This is to make sure that both elements are strong enough to manage the loading mechanisms arising due to them operating in water. However, due to the nature of the loads arising the flow pressure variation applied on the tower could be an important vibration source that may affect the dynamic behaviour of the entire structure. To initially investigate this type of effect and provide the basis for further work, the smaller tunnel and TST structure were designed and manufactured. Two important design criteria were identified in this initial set of experiments in order that the output could be considered to provide good reference for future physical experiments in the wind tunnel. These were that the object under test could be assumed to operate without

deformation within a steady and uniform flow profile.

The first important design feature for the scale model TST used in these initial experiments was the adoption of metallic blades. It was assumed that the deflection caused by the flow pressure was small enough to be ignored. This rigid body setting was important since it meant that the investigation to characterise the wake or flow profile occurring after the blade in the different air speeds could be based upon the adoption of a blade geometry that doesn't change with the air pressure. This assumption was important since it was then possible to subsequently deploy blades that had been deliberately manufactured to replicate the deflection of a faulty blade and to then associate any changes to the flow profile with the introduced fault.

The second important property engineered into this test rig was the flow profile within the swept area of the rotor. The air flow in the full wind tunnel was profiled as the test results indicated. It is possible to predict that, when the blade rotor was being driven by the resulting profiled flow, the vibration in the axial direction would be affected by ever-changing thrust on each blade arising due to this turbulence. Therefore, in order to capture the vibration characteristics of the flow-related pressure variation on the tower, the smaller wind tunnel was equipped with an additional flow straightener honeycomb and provided with smooth inner walls. These additional elements were deployed to generate the relatively steady and uniform flow conditions required. These flow conditions are difficult to achieve in the larger wind tunnel.

The comparisons between the healthy and faulty blade with and without air flow were shown in Figure 3.1. They indicated that the assumed flow-related influences can

be observed from this small model. From this it was possible to postulate what influence these faults would have on the full-scale TST.

The first thing that needed to be considered is the role of the geometric design of the TST tower based on vibration considerations. Work by CMERG researchers (Mason-Jones et al 2013) investigated the effect of the tower shape on TST performance by simulating the axial wake velocity around the surface of the tower. However, the corresponding vibrations both in the lateral and horizontal axis of different towers as they operate underwater is still un-researched.

Although the amplitude at the fixed rotational frequency increases as the wind speed increases from 20% and 60%, its cause can be interpreted as being related to both the asymmetrical thrust on the rotor due to the faulty blade and the unique pressure variation on the tower due to the wake of the faulty blade. However, in this case, it is difficult to distinguish between the two causes which contribute more for the horizontal axis even though the vibration of the structure itself can be excluded by comparing the group tested without wind. In one aspect this does not represent a serious problem since both causes are related to the presence of a blade fault. It is the diagnosis of this fault that lies at the heart of this CM application, and that will not depend upon the attribution of the change in vibration, but will be related to the detection of this change.

It may be inferred that, for full-size or even larger TST structures, both of these two causes could play a more significant role in the horizontal axis vibration. This will vary, depending on the structural design of the tower and the specific failure mode of the blade(s).

6.2.2 Experiment 2

The second set of experiments used a scale model HATT structure. This comprised of a 3-bladed rotor, motor, 3-D printed tower and base for investigating the vibration of the system with faulty blade and yaw errors. The tower was set to have the square aligned cross section and wider surface compared to the blade used. Whilst this ratio of dimension between the blade and tower may not be practical, in a structural sense, the duration of the pressure variation on the tower due to blade passage was extended for each blade and the influence of the B-T interactions in each rotation was strengthened.

According to the analysis of the experimental results, the vibration signal from the nacelle or hub can be the initial monitoring node for the blade health monitoring system. The overlap STFT identified changes made to the condition of the blade. Although the most sensitive part for the blade failure should be on the mid span or blade tip, due to the potentially harsh environment to which they will be exposed, the attachment of the sensors on the blade was not the best choice. The vibration-based monitoring technique is the most cost-effect method to serve other techniques for detecting and identifying the blade failures both in short term and long term.

6.3 Flow Profile Measurement and Pressure Variation on the Tower

Chapter 4 presented the experimental work undertaken to validate the feasibility of an innovative flow profile measurement approach. This was intended to support a new monitoring principle for blade status. A test rig featuring the structural independence of the blade and the tower was designed. The aim of this design was eliminating the vibration of the tower from rotation effects associated with the healthy or faulty blade.

The software for the test rig was developed and integrated using two differing platforms. The central monitoring software was developed using NI LabVIEW 2013myRIO and implemented using a myRIO running the NI Linux Real-Time operating system. An open-source Arduino Software (IDE) was programmed for blade control and blade position tracking. By installing the corresponding add-on, the programmed Arduino board could be directly controlled by the LabVIEW allowing the setting of the rotational speed and cyclic rotation angle. Another program was developed by LabVIEW for data storage in the PC. Once in place the testing was undertaken, and the following points were identified.

6.3.1 The Flow Profile Measurement

The most commonly used method of flow speed or pressure measurement in a wind tunnel is a manometer with a pitot static tube and probe. With the correct installation and fixation of the probe, the flow speed can be precisely read on the manometer. However, to store the results in digital form for further processing and analysis, this setup of measurement equipment is clearly not ideal. Therefore, in this research, the pressure-based sensors were considered as being the best option. They could be operated with a simple and accurate calibration.

In most wind tunnel experiments measuring the pressure on an object utilises a pressure taps, which is usually considered as a reasonable and accurate method. However, the pressure transducer typically deployed in this method may only be able to measure static pressure due to its working principle. These are not suited for the determination of the dynamic air pressure variations arising at the levels of wind speed

associated with the experiments performed in the wind tunnel. Based upon this consideration, an alternative pressure sensor called PAW, designed by RT Corporation in Japan was identified. The choice and applicability of this sensor was discussed in Section 4.3.2. The most important characteristic supporting the choice of these sensors was the concept of the combination of deformable materials and light sensor. It was decided that this combination could make the sensor suitable for dry fluid pressure measurement within the required operating environment, pressure medium and range. The subsequent experimental investigation can be seen to justify this selection and the novel method produced has great potential.

The sensitivity of the deformation part is the most important criteria for the measurement accuracy. However, for underwater application, the deformation part (currently a urethane sponge) of the PAW sensors mounted on the tower may need to be made nonporous. It must remain semi-translucent, but needs to be adapted for water immersion. In addition, the design of the hole on tower for mounting the PAW sensors to ensure their performance, which was considered in **Section 4.2**, is also important. These two factors can be seen to be resolvable but are not be discussed in this thesis.

The number of the PAW sensors on the tower is another key factor in improving the accuracy of the estimated flow profile. In this test rig, the results from a manometer based assessment showed that the highest wind speed was close to the middle of the cross section of the test section. In this set-up PAW3 was the closest to this position, but not actually on the mid-point. At the scale of the tests being undertaken here it was not possible to deploy sensors closer together and the corresponding missing data could

result in a limited and possible inaccurate flow profile. However, the results indicate the method was successful and as tower geometry becomes larger, it becomes viable to add further sensors. As such the method should be enhanced. As a consequence, it is possible to see that the method could be adapted to provide better pressure estimation and thus support TST blade monitoring.

6.3.2 The 3-D Printed Blade

The 3-D printed blade used in the experiment in Chapter 4 was designed as a cuboid as blade geometry is not an object of study here. Although the quality of the blade appeared to be reliable and repeatable, it was found that the bending stiffness of the blade could be different even for the blade with same size and shape. This was most likely due to variations in the finished part which the naked eye cannot observe. To mitigate against these effects having an influence on this study two points should be considered.

Firstly, the calibration of the strain gauge on the blade was made between the tip deflection and output voltage instead of the relation between applied force and the output voltage. This is because the wind force applied on the blade is unevenly distributed and unknown. The loads on the blade are thus not a reliable value in this case. The method also removes any influence associated with the variation in blade properties. An example of laser-based tip deflection measurement in wind turbine shows that the tip deflection is the most intuitive indicator for blade health. It must be stated that similar data is still difficult to obtain in TST application.

The No.2 3-D printed blade, which represents the wrongly pitched blade, is not instrumented with strain gauge for dynamic measurement as the loads on the blade can

be predicted to be certainly different with the first blade under the same wind setting.

Therefore, the static test for No.2 blade is also unnecessary.

In practice, the state, bending stiffness or even the shape of the blade could be different for each installed blade. In addition, over time the properties of each blade may change from what they were on installation due to long-term operations with effects such as water absorption within the composite material. To assure the viability and accuracy of any monitoring method it is therefore important that the comparisons between the healthy and faulty conditions should be conducted on the same blade and not on adjacent blades. This in effect relates to the need to monitoring changes in condition and not actual condition, which is a commonly applied CM approach.

6.3.3 Static Test

Based upon the static comparisons of the pressure on the tower with different blade positions it is possible to identify that, for each incident of blade passage, the duration of the coverage for each of the PAW sensors is different. This is due to the corresponding angular velocity. However, the information provided by each PAW sensor is consistent between blade passages suggesting that the method can reliably monitor each rotation. For real-life TST blade monitoring it may be asserted that more factors such as surface roughness, local geometry, rotational speed and flow velocity profile need to be considered. As such the static tests presented in this research were used to provide a reference to how the approach may be applied for a full-size case but cannot be considered as enabling the setting up of actual thresholds for appropriate blade fault or failure monitoring; the method will need to be applied in specific

installations.

One parameter identified as critical to blade health is fatigue and it can be considered that identifying and quantifying any occurrences of extra deflection arising could be a very important factor for full-size turbine blade health prognosis. In addition, the work done by each blade whilst continuously withstanding the cyclic short-time fluctuations of flow loads could also be potentially acquired from the deployed sensor set-up. These points may be further reinforced with the consideration of the dynamic testing results.

6.3.4 Dynamic Test

The information made available from the dynamic assessment of blade deflection/position via the strain gauge measurement during the blade rotation was shown in Figure 4.18. The extra deflection due to the blade passage can be observed as expected. After averaging the data for each blade deflection, the comparison between the dynamic and static deflection was shown in Figure 4.19. It may be asserted that the more complicated turbulent flow arising under the sea may result in more unpredictable blade deflection during each rotation. This makes the acquisition and analysis of real-time strain data very challenging. In addition, installing the required strain gauges either inside or outside of the blade is difficult; strain gauges will potentially experience high failure rates not least due to their location in the water.

This highlights the importance of the monitoring technique without installing anything on the TST blade. The obtained pressure signals in each test indicated the pressure variation at four different points. The flow profile was estimated as Figure 4.20

with data being interpolated between two sensor positions. This was required because, considering the size of the sensor and the tower, four sensors were appropriate. For a full-scale TST such a restriction may not apply and the surface of the tower could be covered with sensors. In addition to providing more detailed data this would also prevent problems brought on by individual sensors failure.

The significance of the resulting multi-sensor flow profile based blade monitoring technique thus enabled will include:

- The estimated flow profile in real TST could be more precise than the simulated flow profile which is based on the surface velocity and flow profile power law.
- The sensors on the tower may be considered as providing a sensitive tool for blade monitoring. This will also allow them to be used for warning of the extreme flow conditions which currently is the biggest threat for blade failures.
- Assuming that the blade position can be measured, as it in this case, by extracting signal segments which present the pressure without blade passage, a long-term flow profile time series can be accumulated. This can support further blade load simulation and turbine design iteration.

The next phase of this research considered how the above approach may be applied, with the introduction of geometry changes intended to be representative of potential blade faults. The efficacy of this work is discussed as below:

The removal of material from behind the blade (No.3 in Table 4.2) was undertaken with the objective of simulating the reduced bending stiffness without changing the

shape and surface conditions of the blade. It is likely that a number of potential blade failure modes in real life will lead to abnormal flap-wise deflection. The research question posed was therefore to investigate if such a change could cause the change of the pressure variation.

- The capability for the deployed method to detect this change has been proved by comparison, as shown in Figure 4.27. The possible influence of the extra deflection for reference blade in the static test due to the closer tower cannot be validated by the dynamic test.

The next section of work considered the removal of sections of the blade, which is again a potential consequence of blade failure. Considering the results obtained from these experiments suggested that:

- The application to the analysis of the missing blade tip (No.4 in Table 4.2) was more successful than for the missing part in the middle span (No.5 in Table 4.2). This implies that the data from the sensor which is close to the blade tip is the most sensitive one for detecting the failure. This principle potentially applies to the TST with any scale levels.

In the final section of this initial testing blades were set up for tests at wrongly pitched angles. The effectiveness of the approach is again being successful demonstrated:

- The tests (No.2 in Table 4.2) resulted in the discrepancy of the pressure variation at all four positions compared to the optimal group as shown in Figure 4.30. In this case, the chord length in blade tip is same as that of the blade root, which is

used to highlight the potential discrepancy by the blade failures but not practical for full-size TST. Therefore, the sensor which is close to the first aerofoil profile (blade root) could be the most sensitive one to detect this failure.

The results from Chapter 3, confirmed the potential of the approach with the identification of the yaw error and faulty blade. These can respectively result in the fluctuation of the rotor speed in one rotation and reduced rotational speed, which pose a challenge for conventional CM analysis methods. By synchronisation with the azimuth of the blade, the pressure variation can be processed and plotted as shown in the figures in Chapter 4. This method enhances monitoring techniques that may be in place.

The feasibility and performance of the approach based upon the monitoring of the pressure on the tower have been verified in Chapter 4. The design suggestions of the selection, location and operation of the pressure sensors adopted based on the testing in wind tunnel was also considered. The discussion about the specific analytical methods for these pressure signals will be given in the next section.

6.4 Pressure Signal Simulation and Analysis

Chapter 5 presented the analytical method developed using the simulated signal of the pressure on the tower during the operation of the 3-bladed TST. The simulation method was presented in Section 5.1.1 and the simulated scenarios based on the failures from Chapter 4 were presented in Table 5.1.

By using the similarity in shape between the simulated pressure signal and the

trapezoidal wave, some examples of the latter were used to test the feasibility of the MATLAB-based Duty Cycle functions for further analysis. This function simplified the traditional method for analysing square or trapezoidal waves. According to the characteristics of the pressure signal obtained from wind tunnel experiment, the duration and shape of the rise and fall time are not considered in the duty cycle analysis for highlighting the more important information.

6.4.1 Duty Cycle and P-A Curves

The duty cycles of the pressure signal from PAW1 are the most sensitive and intuitive values for detecting the discrepancy brought by the faulty blade. In other words, this method focuses on the changed duration of blade passage. As mentioned in Section 6.3.1, the number of the sensors on the tower can improve the accuracy of the estimated flow profile. This approach would not be adopted in real-life as the integrity of the CM functions associated with the sensors may be threatened.

The proposed P-A curves are established by extracting the initial phase angle and amplitude at the frequency of 3ω (ω is rotational frequency) from all of the possible combinations of the blade faults. In practice, these failures can be tested in the field by using the different prototypes of the turbine blade for more reliable results. The point at this stage in the development is to consider whether the results from the feasibility study of this method are successful. The method is based on the processed signal which starts precisely from the required position so that the signal for each rotation of the rotor can be segmented. The difference between each of the trough segments caused by any deviations to the blade passage can be finally classified as the change of the amplitude

and initial phase angle of the fundamental wave. This method is simple and yet rigorous. To prevent the possibility of inference from anticipated events such as wave-current effects or the pressure changes due to water depth, it was decided that more reliable algorithms are needed.

6.4.2 Overlap

Overlapping the signal segments was identified as being another way to conduct intuitive comparisons. It is only applied for the signals from the sensors on the tower within the locations corresponding to the middle span strut. For flow profile measurement, these signals are used to improve the accuracy of the results. For failure diagnosis, they are only used to detect the wrongly pitched blade and the blades with missing parts. By testing the blade with different pitch angles, it was possible to create a model of the corresponding pressure variation. The missing part can also be highlighted by the sensors installed within the corresponding partial areas.

6.4.3 Blade Health Monitoring (BHM) system

The logical order of the proposed BHM system and the overall data processing flow were respectively shown in Figure 5.18 and Figure 5.21. The benefit of this approach is its ability to function with the loss of one or more sensors. The system can be programmed in advance to function without the missing data and is capable of recreating a new algorithm by estimating the flow profile between two healthy pressure sensors. This feature allows the system to continue to work until the broken sensors can be replaced by the scheduled maintenance.

In this proposed system, the duty cycle analysis is the first level to detect the changes brought by the failure blade. Based on the analytical method introduced in this thesis, the duty cycle analysis of the pressure signal is conducted by using the data from the relatively stable flow condition. For practical TST blade, the tip might produce smaller pressure variation or even turbulence on the tower. And, except for detecting pitch angle error, the blade root is the least sensitive part for the abnormal deflection caused by the failures. Therefore, the selection of the data from the sensors at different position is significant, which is highly related to the design of the TST structure.

The analysis of the initial phase angle and amplitude of the pressure signal is a reliable way to identify the level of the abnormal deflection. This provides the operator or upper level system to make the next decision of the turbine control. This is also highly related with the real-time flow condition which can also be obtained by the pressure sensors with specific algorithm.

The signal overlap is the most intuitive method that can be displayed on the user interface of the monitoring system. It could provide both type and the specific location of the potential failure.

Based on above, the advantages of the proposed BHM monitoring system if the feasibility are validated by flume tank or field test:

1. The cost of both the hardware and installation is low.
2. It is applicable for most of the existing TST projects.
3. Non-destructive monitoring.

4. The information of the local flow conditions can be accumulated by the system and can be used for further study.
5. No attachment on the rotating blade.
6. Reliable and intuitive.

7. Conclusions

This chapter concludes the entire work of this thesis. It summaries both the new methods for real-time flow profile measurement and blade health monitoring system for tidal stream turbine. Based on the discussions in Chapter 6 it also indicates directions and considerations for future work.

The following conclusions are made:

- The potential for the development of new techniques for the condition monitoring of tidal stream turbines using the wind tunnel was successful demonstrated. This can give other researchers the confidence to conduct TST related research within this low-cost environment at low risk but high efficiency.
- A series of techniques for condition monitoring, signal processing and data storage were developed in the LabVIEW-based CMs platform and the compatible Arduino IDE. These can be of direct relevance to any further related experiments in the wind tunnel. The approaches can be adapted and deployed using the “myRIO” platform for time saving and fine control.
- The flow profile was estimated by using the array of the PAW sensors on the tower to measure the dynamic pressure while the blade is passing. Using this approach, the Blade-Tower interactions were experimentally investigated in the wind tunnel. This is the first such investigation of this relationship.

- The first experiment in chapter 3 provided a better understanding of the vibration which is solely resultant from the incoming flow. This was added to the model TST structure via the experiment in wind tunnel. For the consideration of the much higher flow pressure on the tower and loads on the blade, it is instructive to analyse the vibration by classifying the vibration sources into two categories: Mechanical and Hydrodynamic.
- In the flow profile measurement experiment, the design of the structure to be comprised of the independent blade and tower was of great significance in eliminating the interference from the physical connection between the blade rotor and the tower. The same test rig could be adapted in the future for investigating the more realistic and detailed characteristics of the B-T interactions in water.

7.1 Contributions

The following contributions were generated by the research presented:

- A novel method for measuring air-flow and pressure in a lab-scaled wind tunnel was engineered. In doing so the concepts and the operating principles of the PAW were explored to provide a sensing method that is equally applicable in different fluid environments.
- The blade status was successfully estimated by the pressure variation on the tower during the blade passage without installing any sensors on the blade. This could be a most cost-effective method to both detect and classify the blade failures. Potential

identifiable faults include rotor imbalance, missing or damaged blade sections, wrongly pitched angles and the onset of variations in stiffness and/or bending.

- The deployment of the underwater PAW sensors will provide the capability to raise an alarm in the case of extreme flow conditions. This may be either to alert operators directly or, more beneficially, using the monitoring system. An emergency stop or pitch control can be carried out to prevent potentially devastating blade faults. This is a function that all the current TST projects most urgently need.
- The azimuth angle of the blade has been used in a novel way as a reference for the BHM system. This concept has not been previously studied by any researchers. It can provide useful information for the development of potential new techniques. These can be tested in the TST models. Accordingly, the concept of the Blade Positioning system (BPs) was proposed.
- A new and intuitive analytical method for acquiring and processing data on the pressure on the surface of the tower was established. This will increase the reliability of the CMs as they are applied to TST. These are operated in hostile and complicated flow conditions. Once a failure has been detected, its criticality determined and assessed then, depending upon the seriousness level corresponding measures can be taken in a timely fashion.

7.2 Recommendations and Future Work

Some consideration of the further research regarding the wind tunnel system

development can be identified:

The influence of the air directionality is unknown for the proposed monitoring method. For example, if there is yaw error occurring on the structure, the deviations of measured data from the PAW sensors for both blade passage and/or wind velocity profile may be uncertain. This is related to the working principle of the sensors which respond to changes in pressure.

Although the dynamic performance of the PAW sensors is better than any other sensors tested, the data obtained provided an indication of the real dynamic wind pressure. This requires further consideration and potential design enhancements to provide better resolution and accuracy. The design of the PAW sensor and the material of the force collecting element may be further improved.

The geometry of the blade, which is not studied in the thesis, may be a further influence on the wake behind the blade and hence the pressure variation on the tower. In addition, the geometry of the pillar used in the tests is cuboid, which is not practical for real TST. For more detailed understanding, water flume testing of a scale TST is necessary to investigate these two factors.

The flume or water tank test of this system installed onto a scale model TST is the next step to further implement and verify the proposed methods. A prototype TST model, designed by CMERG, and water flume are available for these future tests. Some considerations for establishing the corresponding underwater test rig are listed below:

7.2.1 Sensor Design

For underwater deployment, the pressure sensors must have water proof sealing. This

needs to provide good performance, durability, and sensitivity. The force collector element of the candidate pressure sensors plays a crucial role on the accuracy of the sensor. It acts to enable the conversion from pressure to digital data. The resultant pressure signal is then synchronized with a global timestamp, blade position, thrust etc.

The influence of the surface measurement area of each pressure sensor on the reliability of the data is still unknown. Theoretically, reducing the area of each sensor and increasing the number of the sensors on the tower can improve the resolution and accuracy of the estimated flow profile. However, the area of each sensor can also affect the sensitivity. These relationships can be validated by the flume test with sensor prototypes of different sizes.

7.2.2. Blade Positioning System

The midpoint between the two adjacent blades is a very important reference for signal processing in the proposed monitoring system. In practice it can be realized by the addition or modification of an existing rotary encoder which can be set up to generate a pulse corresponding to each midpoint. It may be anticipated that most TST designs will include such an encoder within the hub; it is a simple task to include one if necessary. More importantly, the blade position information can be used to analyse other datasets such as the thrust, vibration, torque and power output. This added monitoring item is not difficult to implement on the prototype TST in the water flume.

7.2.3. Monitoring System

The algorithms of the proposed monitoring system may need to be modified and/or improved for adapting the system to the characteristics of water. The pressure at depth

is the first factor that may affect the measured results and its dynamic impact needs to be investigated. In particular, the discrepancy of the pressures at depth is magnified by the height and operating depth of the existing TST project. Therefore, the compensation data for measured pressure may be necessary for the specific environment. However, it should be noted that the monitoring approach is based upon pressure change, and as such the adaption of the technique should be straightforward.

The monitoring system needs an enhanced algorithm to ensure the performance of the sensors and the reliability of the data. Any data related to broken or faulty sensors should be eliminated from the process of the estimation of the flow profile. This can be developed based on the following principle: The data from adjacent sensors can provide the upper and lower limits for the measured values of the target sensor. Once the measured value extends beyond the limits, the corresponding sensor will be determined as the faulty one by the system.

7.2.4. Structural Design

As the sensors of the proposed method were mounted on the tower the measured flow profile can only cover half of the swept area of the rotor blade. If necessary it would be possible to mount a structure above the nacelle to support additional sensors to measure the complete flow profile. With smaller diameter of this extended upper tower, the impacts from the upper blade passage can be minimised. This approach may be seen as only necessary if the existing set up cannot provide the sensitivity needed. It is not currently needed.

The vibration of the TST may have an impact on the performance of the pressure

sensors in the flume. The installation or design of the tower of the model TST must therefore be adapted to withstand the drag force from the water.

7.2.5. Flow Conditions

The existing geometry of the sensor array collecting the force the pressure profile assumed that the flow is ideally at right angles. Since the air in the wind tunnel is relatively stable, the obtained pressure signal is assumed to represent the velocity profile. In a marine environment, the effects of waves and turbulence are known to be continuously changing the local flow conditions. Therefore, the tests in a flume of flow tank must be used to study how to minimise or eliminate the interference on the obtained signal arising from local flow conditions. This represents a challenge which is the most significant factor for the full realisation of the proposed monitoring technique. It should be noted that such flow conditions will vary continuously but that the effect of a blade fault will not. Thus, the analysis approach embodied in this research will be effective, with modification.

7.2.6 Implementation on Full-scale TST

Although there is still a long way to go before the proposed technique may be implemented on a full-scale TST, there is a factor that needs to be considered in advance. As the tip clearance and the blade geometry of the existing TST are different. The flow impacting on the tower will therefore need to be characterised. If necessary an extra support structure may need to be installed behind the blade for mounting the sensors. Other factors such as the collision of mammal or cavitation are not discussed here but still important for its implementation. It is intended however that the system deployed

will utilise a sensor array derived from sensors modified to suit. They will be located as required on the tower and will provide a robust and reliable blade health monitoring function.

References

- Ahlstrom, A., 2006. Emergency stop simulation using a finite element model developed for large blade deflections. *Wind Energy* 2006, 9, 193–210.
- Aleem, S., Ibrahim, A. Zobaa A., 2014. Mathematical Analysis of the Turbine Coefficient of Performance for Tidal Stream Turbines. Retrieved from: <http://bura.brunel.ac.uk/handle/2438/11044>
- Allmark, M., 2017. Condition Monitoring and Fault Diagnosis of Tidal Stream Turbines Subjected to Rotor Imbalance Faults. PhD thesis, Cardiff University.
- Allmark, M., Grosvenor, R., Byrne, C., Anayi, F., Prickett, P., 2013. Condition Monitoring of a Tidal Stream Turbine: Development of an Experimental Methodology. Presented at the 9th European Wave and Tidal Energy Conference, Aalborg, 2013.
- Andrew, H., Stecki, J. and Shoshanna, D., 2008, The Maintenance Aware Design environment: Development of an Aerospace PHM Software Tool, PHM technology, [Online], pp. 12/12/2012 available at: <http://www.phmtechnology.com/assets/technical/How%20MADe%20works.pdf>
- Andritz Hydro Hammerfest(AHH), 2012. ANDRITZ HYDRO Hammerfest: One of the world leaders in the hydropower business, 1–12.
- Aquatic Renewable Energy Technologies (Aqua-RET), 2008. Operational Principles Description of the “Wave-to-Wire” Chain, Available at: <http://www.aquaret.com/images/stories/aquaret/pdf/tsopprinciples.pdf> (accessed July 2017).

- Arifuzzaman, M., Mashud, M., 2012. Design Construction and Performance Test of a Low Cost Subsonic Wind Tunnel. IOSR Journal of Engineering, 2(10), 2250–3021.
- Atlantis Resources., 2015. Ar1500 Tidal Turbine, 6. Retrieved from:
<https://www.atlantisresourcesltd.com/wp/wp-content/uploads/2016/08/AR1500-Brochure-Final-1.pdf>
- Back, C. Madsen, H. and Johansen, J., 2001. Influence from blade-tower interaction on fatigue loads and dynamics. EWTEC 01 Proceedings 394-397. 2001
- Back, C., Aagaard Madsen, H., Johansen, J., 2001. Influence from blade-tower interaction on fatigue loads and dynamics, EWEC '01 Proceedings (2001) 394-397
- Bahaj, A.S., 2011, Development of marine current turbines for electricity production. IEEE Power and Energy Society General Meeting, July 2011 Detroit, pp. 1–4.
- Balageas, D., Fritzen, C., Güemes, A., 2006. A Structural Health Monitoring; ISTE Ltd.: London, UK, 2006.
- Bao, X., Chen, L., 2012. Recent progress in distributed fibre optic sensors, Sensors, vol.12, no.7, pp.8601–8639, 2012.
- Batten, W. M. J., Bahaj, A. S., Molland, A. F., & Chaplin, J. R., 2006. Hydrodynamics of marine current turbines. Renewable Energy, 31(2), 249–256.
<https://doi.org/10.1016/j.renene.2005.08.020>
- BBC, 2010. Blade fault on giant tide turbine AK1000 in Orkney. [Online], Available: <http://www.bbc.co.uk/news/uk-scotland-highlands-islands-11492829>. (accessed July 2017)

BBC, 2016, 'Strangford tidal energy turbine to be removed', Available at:

<http://www.bbc.co.uk/news/uk-northern-ireland-35416282> (accessed July 2017)

Betz, Das Maximum der theoretisch möglichen Ausnützung des Windes durch Windmotoren, Zeitschrift für das gesamte Turbinenwesen, vol. 26, no. 307–309, p. 8, 1920.

Betz, A., Windenergie und ihre Ausnützung durch Windmühlen, Vandenhoeck und Ruprecht 1926,

Black & Veatch Ltd., 2005. Tidal stream energy resource and technology summary report. Carbon Trust.

Bodil, A.; Mats, D.; Magnus, U., 2011. Feasibility Study of Thermal Condition Monitoring and Condition Based Maintenance in Wind Turbines; Elforsk Report 11:19; ELFORSK: Stockholm, Sweden, 2011.

Boslet, M., 2010, A Big Setback for Tidal Power, Greentech Media, Available at:

<https://www.greentechmedia.com/articles/read/a-big-setback-for-tidal-power>

Brinck, D., Claesson, J. 2013. The Development of a Vertical Axis Tidal Current Turbine. Master of Science Thesis. KTH School of Industrial Engineering and Management.

Burton, T., Sharpe, D., Jenkins, N., Bossanyi, E., Wind energy handbook. Wiley. 2000. ISBN: 978-0-470-69975-1

Campbell S.: 'Annual blade failures estimated at around 3800', Wind Power Monthly,

14 May 2015, Available at:

<http://www.windpowermonthly.com/article/1347145/annual-blade-failures->

[estimated-around-3800](#), (accessed July 2017.)

Caraiman, G., Nichita, C., Mînză, V., Dakyio, B., & Jo, C. H., 2010. Concept study of offshore wind and tidal hybrid conversion based on real time simulation Key Words Introduction into the Hybrid System: offshore wind turbine-tidal wind turbine, (May).

Carroll J., McDonald A., McMillan D., 2016. Failure rate, repair time and unscheduled O&M cost analysis of offshore wind turbines, Wind Energy, DOI: 10.1002/we.1887.

CCC (Committee on Climate Change), 2008. Building a low-Carbon economy -the UK's contribution to tackling climate change. Chapter 5: Decarbonising electricity generation. Available at: <http://www.theccc.org.uk/pdf/7980-TSO%20Book%20Chap%205.pdf> (accessed July 2017)

Chattot, J. J., 2006. Extension of a helicoidal vortex model to account for blade flexibility and tower interference, J. Solar Energy Eng., 128 (2006) 455-460

Chen, B., Zappalá, D., Crabtree, C.J., Tavner P. J., 2014. Survey of commercially available scada data analysis tools for wind turbine health monitoring [Technical report]. Durham University School of Engineering and Computing Sciences; 2014.

Committee on Climate Change, 2012. The 2050 target – achieving an 80% reduction including emissions from international aviation and shipping, (April), 137.

Coscetta, A., Minardo, A., Olivares, L., Mirabile, M., Longo, M., Damiano, M., Zeni, L. 2017. Wind Turbine Blade Monitoring with Brillouin-Based Fiber-Optic

- Sensors. Journal of Sensors, 2017. <https://doi.org/10.1155/2017/9175342>
- Crumpton N., 2004. A Severn barrage or tidal lagoon? (January), Report. Retrieved from
https://www.foe.co.uk/sites/default/files/downloads/severn_barrage_lagoons.pdf
- De Laleu V., 2009. La Rance Tidal Power Plant. 40-year operation feedback – lessons learnt, in: BHA Annual conference. Available at: <http://www.british-hydro.org/downloads/La%20Rance-BHA-Oct%202009.pdf> (accessed July 2017)
- DECC, 2011. Digest of United Kingdom energy statistics (DUKES). Archived from the original (PDF) on 16 December 2011. Retrieved 20 March 2012.
- DECC, 2013. Energy Trends. Practice, (June). Retrieved from
https://www.gov.uk/government/uploads/system/uploads/attachment_data/file/295362/ET_March_2014.PDF
- DECC, 2015. Statistics – Solar photovoltaics deployment. Available at:
<https://www.gov.uk/government/statistics/solar-photovoltaics-deployment>.
(Accessed July 2017)
- Dietz, T. (2015). Energy Consumption, 112(6), 1654–1655.
<https://doi.org/10.1073/pnas.1423686112>
- Elasha, F., Mba, D., & Teixeira, J. A., 2014. Condition monitoring philosophy for tidal turbines. International Journal of Performability Engineering, 10(5),521–534.
- Elghali, S. Benbouzid, M. & Charpentier, J., 2007. Marine Tidal Current Electric Power Generation Technology: State of the Art and Current Status. 2007 IEEE International Electric Machines & Drives Conference, 1407–1412. Available at:

<https://doi.org/10.1109/IEMDC.2007.383635>

Emery, W. J., Thomson R.E., 2001. Data analysis methods in physical oceanography. Gulf Professional Publishing. p. 83. ISBN 978-0-444-50757-0. Retrieved 2011-02-06.

Energy Insight, 2009, NS Power and Openhydro Successfully Deploy In-Stream Tidal Turbine, Available at:
http://www.energyinsight.info/tidal_power_bay_of_fundy.html

Epler, J., Polagye, B., & Thomson, J., 2010. Shipboard acoustic Doppler current profiler surveys to assess tidal current resources. MTS/IEEE Seattle, OCEANS 2010, 2(1).
<https://doi.org/10.1109/OCEANS.2010.5664387>

European Commission,2005. SEAFLOW World's first pilot project for the exploitation of marine currents at a commercial scale. EU publications,

Feng Y., Tavner P., Long H., 2010. Early experiences of UK Round 1 offshore wind farms, Proceedings of the Institute of Civil Engineers – Energy, 163, (4), pp.167-181.

Fleming, P., Gebraad, P., Lee, S., Wvan Wingerden, J., Johnson, MChurchfield, K., Michalakes, J., Spalart P., Moriarty P., 2013. High-fidelity simulation comparison of wake mitigation control strategies for a two-turbine case. ICOWES Conference 2013

Fraenkel, P., 2007. Marine Current Turbines: pioneering the development of zero-head hydro. BHA Annual Conference, 1–27.

Fraenkel, P., 2010. Development and Testing of Marine Current Turbine's SeaGen

1.2MW Tidal Stream Turbine. 3rd International Conference on Ocean Energy, 1–7.

Fraenkel, P., 2011. Under water windmills, Harnessing the World's marine currents. INGENIA, Issue 46, March 2011.

<http://www.ingenia.org.uk/ingenia/issues/issue46/fraenkel.pdf>

Fraenkel-Wright Ltd, 2012. Tidal Stream Turbines: A Technical Update key generic factors affecting energy capture, (May).

Frau, E., Kress, C., Chokani, N., & Abhari, R. S., 2015. Comparison of Performance and Unsteady Loads of Multimegawatt Downwind and Upwind Turbines. Journal of Solar Energy Engineering, 137(4), 41004. <https://doi.org/10.1115/1.4030314>

Fung, C., Howell, R.J. and Walker, S., 2014. Effect of The Velocity Profile of Incoming Flow On The Performance Of A Horizontal Axis Tidal Stream Turbine. In: AWTEC2014. 2nd Asian Wave and Tidal Energy Conference, Tokyo, Japan.

Gan, L. K., Shek, J. K. H., & Mueller, M. A., 2017. Modeling and Characterization of Downwind Tower Shadow Effects Using a Wind Turbine Emulator. IEEE Transactions on Industrial Electronics, 64(9), 7087–7097.

<https://doi.org/10.1109/TIE.2017.2686306>

Giorgi, S., Ringwood, J. V., 2013. Can tidal current energy provide base load? Energies, 6(6), 2840–2858. <https://doi.org/10.3390/en6062840>

Glauert, H., 1933. Wind Tunnel Interference on Wings, Bodies and Aircrews. Tech. Rep. R. & M. No.1566

Graham, J. M. R., Brown C. J., Giannakidis, G., 2001. Aerodynamic interaction

- between wind-turbine rotor blades and the tower, EVEC '01 Proceedings (2001)
359-361
- Graham, J. M. R., Brown, C. J., Giannakidis, G., 2001. Aerodynamic interaction between wind-turbine rotor blades and the tower, EVEC '01 Proceedings (2001)
359-361.
- Guemes, A., Fernandez-Lopez, A., Soller, B., 2010. Optical fibre distributed sensing-physical principles and applications. *Struct. Health Monit.* 2010, 9, 233–245.
- Hameeda, Z., Honga, Y.S., Choa, Y. M., Ahnb, S.H., Songc, C. K., 2007. Condition monitoring and fault detection of wind turbines and related algorithms: A review *Renewable and Sustainable Energy Reviews.* 2007.
<http://doi.10.1016/j.rser.2007.05.08>.
- Hansen, M. O. L., Voutsinas, JENS., Sørensen N., Madsen, H. A., 2006. State of the art in wind turbine aerodynamics and aeroelasticity, *Progress in Aerospace Sciences*, 42 (2006) 285-330.
- Hansen, M.O.L., Sørensen, J.N., Voutsinas, S., Sørensen, N. & Madsen, H.A., 2006, "State of the art in wind turbine aerodynamics and aeroelasticity", *Progress in Aerospace Sciences*, vol. 42, no. 4, pp. 285- 330.
- Harries, T., Kwan, A., Brammer, J., Falconer, R., 2016. Physical testing of performance characteristics of a novel drag-driven vertical axis tidal stream turbine, With comparisons to a conventional Savonius. *International Journal of Marine Energy*, 14, 215–228. <https://doi.org/10.1016/j.ijome.2016.01.008>
- Hau, E., 2006. *Wind Turbines, Fundamentals, Technologies, Application, Economics*,

- 2nd ed.; Springer: Berlin, Germany, 2006.
- Hau, E., 2008. Windkraftanlagen - Grundlagen, Technik, Einsatz, Wirtschaftlichkeit
- Hess, A., Stecki, J. S., & Rudov-clark, S. D., 2015. The Maintenance Aware Design environment: Development of an Aerospace PHM Software Tool the Maintenance Aware Design environment: Development of an Aerospace PHM Software Tool, (July 2015).
- Houde, J., 2012. Cost-benefit analysis of tidal energy generation in Nova Scotia: A scenario for tidal farm with 300 MW of installed capacity in the Minas passage in 2020, Master thesis, Dalhousie University, Canada.
- Hoyle, N., & Flow, E., 2009. Royal Academy of Engineering: Renewable Power. Wind Turbine Power Calculations, 1(1), 1–5.
- Hulsbergen, K., Steijn, R., van Banning, G., Klopman, G., & Fröhlich, A., 2008. Dynamic Tidal Power (DTP) - A new approach to exploit tides. International Conference on Ocean Energy (ICOE), (October), 1–10.
- Hulsbergen, K., Steijn, R. Banning G, Klopman G., 2008. Dynamic Tidal Power – A new approach to exploit tides. 2nd International Conference on Ocean Energy (PDF). Brest, France.
- Hulsbergen, K., Steijn, R., Hassan R., Klopman G., Hurdle D., 2005. Dynamic Tidal Power (DTP), 6th European Wave and Tidal Energy Conference, Glasgow, UK, August 29th – September 2nd, 2005
- Hyun, B. S., Choi, D. H., Han, J. S., Jin, J. Y., & Roo, C. H. (n.d.). Performance Analysis and Design of Vertical Axis Tidal Stream Turbine. Power, 1–8. 2010

- Isshiki, H. Kenji S., Rho-Taek J., 2016. Water purification in fresh-water-lake adjacent to sea using tidal energy, IEEE, ISBN: 978-1-5090-2445-2. 150–157.
- Jha, S., 2016. Tidal Turbine Collision Detection – Requirements Report Tidal Turbine Collision Detection Requirements Report, (May).
- Joosse PA, Blanch MJ, Dutton AG, Kouroussis DA, Philippidis TP, Vionis PS. Acoustic emission monitoring of small wind turbine blades. In: Proceedings of the 21st ASME wind energy symposium conjunction with 40th AIAA aerospace sciences meeting, Reno, USA 2002:1–11.
- Jupiter Hydro Inc., 2012. Review of Selected Tidal Power Technologies Final Report. Available at:http://jupiterhydro.com/uploads/3/1/3/4/3134001/tidal_energy_report_20_09_12_final.pdf
- Kabir, M. J., Oo, A. M. T., & Rabbani, M., 2015. A brief review on offshore wind turbine fault detection and recent development in condition monitoring based maintenance system. 2015 Australasian Universities Power Engineering Conference (AUPEC), 1–7. <https://doi.org/10.1109/AUPEC.2015.7324871>
- Kabir, M. J., Oo, A. M. T., & Rabbani, M., 2015. A brief review on offshore wind turbine fault detection and recent development in condition monitoring based maintenance system. 2015 Australasian Universities Power Engineering Conference (AUPEC), 1–7. <https://doi.org/10.1109/AUPEC.2015.7324871>
- Keenan, G., Sparling, C., Williams, H., Fortune, F., & Davison, A., 2011. SeaGen environmental monitoring programme: Final report. Royal Haskoning, (January),

81.

Kim, H. G., Lee, S. M., Lee, S. G., 2010. Numerical analysis on the aerodynamics of HAWTs using nonlinear vortex strength correction. *Current Appl. Phys.*, 10 (2010) S311-S315.

Kim, H., Lee, S., & Lee, S. 2011. Influence of blade-tower interaction in upwind-type horizontal axis wind turbines on aerodynamics. *Journal of Mechanical Science and Technology*, 25(5), 1351–1360. <https://doi.org/10.1007/s12206-011-0311-5>

Kim, H., Lee, S., & Lee, S., 2011. Influence of blade-tower interaction in upwind-type horizontal axis wind turbines on aerodynamics. *Journal of Mechanical Science and Technology*, 25(5), 1351–1360. <https://doi.org/10.1007/s12206-011-0311-5>

Koh, W. X. M., Ng, E. Y. K., 2017. A CFD study on the performance of a tidal turbine under various flow and blockage conditions. *Renewable Energy*, 107, 124–137. <https://doi.org/10.1016/j.renene.2017.01.052>

Lee, J., Son, E., Hwang, B., & Lee, S., 2013. Blade pitch angle control for aerodynamic performance optimization of a wind farm. *Renewable Energy*, 54(June), 124–130. <https://doi.org/10.1016/j.renene.2012.08.048>

Lee, J., Son, E., Hwang, B., & Lee, S., 2013. Blade pitch angle control for aerodynamic performance optimization of a wind farm. *Renewable Energy*, 54(June), 124–130. <https://doi.org/10.1016/j.renene.2012.08.048>

Lewis, M., Neill, S. P., Robins, P., Hashemi, M. R., & Ward, S., 2016. Characteristics of the velocity profile at tidal-stream energy sites. *Renewable Energy*, 114, 258–272. <https://doi.org/10.1016/j.renene.2017.03.096>

- Li, W., Zhou, H., Liu, H., Lin, Y., & Xu, Q., 2016. Review on the blade design technologies of tidal current turbine. *Renewable and Sustainable Energy Reviews*, 63, 414–422. <https://doi.org/10.1016/j.rser.2016.05.017>
- Lockhart, R., 2016, Chinese Electricity Consumption Up 6.3%, *AsiaElec - Asia Power*, Available at: <https://newsbase.com/topstories/chinese-electricity-consumption-63>
- Lu, W., Chu, F., 2010. Condition monitoring and fault diagnostics of wind turbines. 2010 Prognostics and System Health Management Conference, 1–11. <https://doi.org/10.1109/PHM.2010.5413527>
- M. Yue, 2016, Three Gorges Dam. Report, Stanford University.
- MacEnri, J., Reed, M., & Thiringer, T., 2011. Power Quality Performance of the Tidal Energy Converter, SeaGen. *International Conference on Ocean, Offshore and Arctic Engineering*, 1–8.
- MacKay, D.J.C. *Sustainable Energy without the Hot Air*; UIT: Cambridge, UK, 2009.
- Mankowski, O., Wang, Q., 2016. Real-time Monitoring of Wind Turbine Blade Alignment Using Laser Measurement. *Procedia CIRP*, 56, 128–132. <https://doi.org/10.1016/j.procir.2016.10.041>
- Manwell JF, McGowan JG, Rogers AL., 2009. *Wind energy explained: theory design and application*. 2nd ed. UK: John Wiley & Sons Ltd, ISBN 978-0-470- 01500-1; 2009.
- Mason-Jones, A., O’Doherty, D. M., Morris, C. E., O’Doherty, T., Byrne, C. B. B., Prickett, P. W., ... Poole, R., 2011. Scaling of a prototype tidal stream turbine using non-dimensional parameters. *EWTEC 2011 Proceedings*, (February).

<https://doi.org/10.13140/2.1.4983.3767>

McEwen, L. N., Evans, R., & Meunier, M., 2012. Cost-Effective Tidal Turbine Blades. International Conference on Ocean Energy, 1–5.

MCT Ltd, 2014. SeaGen Project History. Retrieved from

<http://www.seageneration.co.uk/history.php>

MCT, 2013, World-leading tidal energy system achieves 5GWh milestone, Available at:

<http://www.marineturbines.com/News/2012/09/05/world-leading-tidal-energy-system-achieves-5gwh-milestone> (accessed July 2017)

Meinlschmidt, P., Aderhold, J., 2006. Thermographic Inspection of Rotor Blades. ECNDT 2006, 1~9.

Mérigaud, A., & Ringwood, J. V., 2016. Condition-based maintenance methods for marine renewable energy. Renewable and Sustainable Energy Reviews, 66, 53–78.

<https://doi.org/10.1016/j.rser.2016.07.071>

Milne, I. A., Day, A. H., Sharma, R. N., & Flay, R. G. J., 2015. Blade loading on tidal turbines for uniform unsteady flow. Renewable Energy, 77, 338–350.

<https://doi.org/10.1016/j.renene.2014.12.028>

Morris, C., 2014. Influence of solidity on the performance, swirl characteristics, wake recovery and blade deflection of a horizontal axis tidal turbine. Ph D Thesis. Cardiff University.

O’Doherty, D. M., Mason-Jones, A., Morris, C. E., O’Doherty, T., Byrne, C. B. B.,

Prickett, P. W., & Grosvenor, R. I., 2011. Interaction of marine turbines in close

proximity, (February 2015), 1–8. <https://doi.org/10.13140/2.1.236> [1.9367](https://doi.org/10.13140/2.1.9367)

O'Doherty, D. M., Mason-Jones, A., O'Doherty, T., & Byrne, C. B. B., 2009.

Considerations of improved tidal stream turbine performance using double rows of contra-rotating blades. EWTEC 2009 Proceedings. Retrieved from <http://orca.cf.ac.uk/16917/>

O'Doherty, D. M., Mason-Jones, A., O'Doherty, T., & Byrne, C. B. B., 2009.

Considerations of improved tidal stream turbine performance using double rows of contra-rotating blades. EWTEC 2009 Proceedings. Retrieved from <http://orca.cf.ac.uk/16917/>

Pedrazzani, J. R., Klute, S. M., Gifford, D. K., Sang, A. K., & Froggatt, M. E., 2012.

Embedded and surface mounted fibre optic sensors detect manufacturing defects and accumulated damage as a wind turbine blade is cycled to failure. Report. Luna Innovations Inc.

Power Technology, 2008, Strangford Lough Tidal Turbine, Available at:

<http://www.power-technology.com/projects/strangford-lough/> (accessed July 2017)

Ragheb, M., 2013. Aerodynamics of rotor blades. Available at:

<http://mragheb.com/NPRE%20475%20Wind%20Power%20Systems/Aeorodyna%20mics%20of%20Rotor%20Blades.pdf>

Ren N., Ou J., 2009 Aerodynamic Interference Effect between Large Wind Turbine

Blade and Tower. Computational Structural Engineering. Springer, Dordrecht

Rezaei, M., Behzad, M., Haddadpour, H., Moradi, H., 2015. Development of a reduced

order model for nonlinear analysis of the wind turbine blade dynamics, Renew.

Energy 76 (2015) 264e282.

Ribrant J., Bertling L.M.: Survey of failures in wind power systems with focus on Swedish wind power plants during 1997-2005, IEEE Transactions on Energy Conversion, 2007, 22, (1), pp.167-173.

Robert H. C., 2007. Tidal Power Schemes and Modes of Operation, in Elements of Tidal-Electric Engineering, 1, Wiley-IEEE Press, 2007, pp.35-45.
<https://doi.10.1109/9780470144985.ch5>

Roberts, A., Thomas, B., Sewell, P., Khan, Z., Balmain, S., & Gillman, J., 2016. Current tidal power technologies and their suitability for applications in coastal and marine areas. Journal of Ocean Engineering and Marine Energy, 2(2), 227–245.
<https://doi.org/10.1007/s40722-016-0044-8>

Robinson, E., & Byrne, G., 2008. Methodology for modeling tidal turbine characteristics. Oceans 2008. [Online], Available at:
<https://doi.org/10.1109/OCEANS.2008.5151948>

Robotham A. ,2008, Tidal Power, Available at: http://rpec.co.uk/rpec_new/pages/Art-11.html

Rogers, A. J., 1999. Distributed optical-fibre sensing. Meas. Sci. Technol. 10, 75-99 (1999)

Rolfes, R., Tsiapoki, S., Häckell, M., 2014. Sensing solutions for assessing and monitoring wind turbines, in Sensor Technologies for Civil Infrastructures - Applications in Structural Health Monitoring, M. Wang, J. Lynch and H. Sohn, Eds., Woodhead Publishing, 2014, pp. 565-604

- Ruan, J., Ho, S. C. M., Patil, D., & Song, G., 2014. Structural health monitoring of wind turbine blade using piezoceramic based active sensing and impedance sensing. Proceedings of the 11th IEEE International Conference on Networking, Sensing and Control, 661–666.
- Sala, G., 2000. Composite degradation due to fluid absorption. Composites: Part B, 31, 357-373.
- Sandeep, B., 2014. Tidal Energy: Technology Brief. Tidal Energy, (June), 122.
- Scottish Power Renewables (SPR) Ltd, 2010. HS1000 1 MW Tidal Turbine at EMEC Supporting Documentation, A30127-S03.
- Shah, S., Jin, K., Fuding, T., Liang, Z., & Chaudhri, A. Z., 2013. CFD Simulation of Vertical Axis Tidal Turbine Using Two- Way Fluid Structure Interaction Method. Proceedings of 2013 10th International Bhurban Conference on Applied Sciences & Technology (IBCAST), 286–291.
- Steijn, R., 2015, Dynamic Tidal Power Technology Advances, Renewable Energy World, Available at:
<http://www.renewableenergyworld.com/articles/2015/01/dynamic-tidal-power-technology-advances.html>
- SWN, 2017, Cape Sharp Tidal Turbine Tangled in Bay of Fundy, 2017, Available at:
<http://subseaworldnews.com/2017/05/05/cape-sharp-tidal-turbine-tangled-in-bay-of-fundy/> (accessed July 2017)
- T. Mikkelsen, 2014. Lidar-based research and innovation at DTU Wind Energy - a review, Journal of Physics: Conference Series, vol. 524, no. 1, 2014.

- Taaffe, D., & Manager, P., 2016. MeyGen Tidal Energy Project Phase 1a – Progress Update, (May). Available at: https://www.all-energy.co.uk/RXUK/RXUK_All-Energy/2016/Presentations%202016%20Day%202/Wave%20and%20Tidal%20Day%202/David%20Taaffe.pdf?v=635997729479358345
- Tartibu, L.K., Kilfoil, M., Van Der Merwe A.J., 2012. Vibration Analysis of a Variable Length Blade Wind Turbine. *International Journal of Advances in Engineering & Technology*. July 2012. Vol. 4, Issue 1, pp. 630-639.
- Tatum, S. C., Frost, C. H., Allmark, M., O’Doherty, D. M., Mason-Jones, A., Prickett, P. W., O’Doherty, T., 2016. Wave-current interaction effects on tidal stream turbine performance and loading characteristics. *International Journal of Marine Energy*, 14, 161–179. <https://doi.org/10.1016/j.ijome.2015.09.002>
- Thresher, R., 2011. A commercialization path and challenges for marine hydrokinetic renewable energy. *IEEE Power and Energy Society General Meeting*, 1–8. <https://doi.org/10.1109/PES.2011.6039092>
- Tidal Lagoon Cardiff Ltd., 2015. Scoping Opinion: Proposed Tidal Lagoon Development, Cardiff, South Wales, (April).
- Timmerman, H., 2009. SKF WindCon - Condition Monitoring System for Wind Turbines, *New Zealand Wind Energy Conference 2009*.
- Todeschini G. 2017, Review of Tidal Lagoon Technology and Opportunities for Integration within the UK Energy System. *Inventions* 2017, 2(3), 14; doi:10.3390/inventions2030014
- Tousif, R., Taslim, B., 2011. Tidal Power: An Effective Method of Generating Power.

- International Journal of Scientific & Engineering Research, 2(5), 1–5.
- UK Department for Business (DBIS), 2017. Digest of UK Energy Statistics (DUKES): renewable sources of energy, 153–191. Retrieved from https://www.gov.uk/government/uploads/system/uploads/attachment_data/file/633782/Chapter_6.pdf
- United Nations Treaty Collection (UNTC), 2016. Paris Agreement. 8 July 2016. [Online], Available at: http://unfccc.int/paris_agreement/items/9444.php
- United Nations, 2017. World Population Prospects: The 2017 Revision, Key Findings and Advance Tables, 46.
- Vennell, R., 2013. Exceeding the Betz limit with tidal turbines. *Renewable Energy*, 55, 277–285. <https://doi.org/10.1016/j.renene.2012.12.016>
- Wang, Q., Zhou, H., Wan, D., 2012. Numerical simulation of wind turbine blade-tower interaction. *Journal of Marine Science and Application*, 11(3), 321–327. <https://doi.org/10.1007/s11804-012-1139-9>
- Wentworth, J., 2013. POSTNOTE: Environmental Impact of Tidal Energy Barrages, (435), 2–5. Retrieved from: www.parliament.uk/briefing-papers/POST-PN-435.pdf
- Yang W., 2013. Testing and condition monitoring of composite wind turbine blades, in Brahim Attaf (Ed.): ‘Recent advances in composite materials for wind turbine blades’, ISBN 978-9889190-0-6, WAP-AMSA, 2013.
- Yang, B., Zhang, L., Zhang, W., & Ai, Y., 2013. Non-destructive testing of wind turbine blades using an infrared thermography: A review. 2013 International Conference on Materials for Renewable Energy and Environment, 407–410.

- Yang, W., Peng, Z., Wei, K., & Tian, W. (2017). Structural health monitoring of composite wind turbine blades: challenges, issues and potential solutions. *IET Renewable Power Generation*, 11(4), 411–416.
- Yang, W., Tavner, P. J., Crabtree, C. J., Wilkinson, M., 2010. Cost-Effective Condition Monitoring for Wind Turbines, *Industrial Electronics, IEEE Transactions on*, vol. 57, no. 1, pp. 263 –271, Jan. 2010.
- Yang, W., Tavner, P., Crabtree, C., Feng, Y., Qiu, Y., 2014. Wind turbine condition monitoring: technical and commercial challenges, *Wind Energy*, vol. 17, pp. 673-693, 2014.
- Yekang K., Derek K., 2011. South Korea's Plans for Tidal Power: When a "Green" Solution Creates More Problems. Report, Nautilus Institute. Retrieved 27 May 2016.
- Yurdusev, M.A.; Ata, R.; Cetin, N.S., 2006. Assessment of optimum tip speed ratio in wind turbines using artificial neural networks. *Energy* 2006, 31, 2153–2161.
- Zahle, F., Sørensen, N. N., Johansen, J., 2009. Wind turbine rotor-tower interaction using an incompressible overset grid method, *Wind Energy*, 12 (6) (2009) 594-619.
- Zhou, H., Wang, Q., Wan, D. C., 2012. Numerical simulations of the 3D viscous flows around wind turbine blade. *Proceedings of 21st National Conference of Hydrodynamics*. (in Chinese, in press).
- Zhu, J., Zhao, Z., 2017. Chinese Electric Power Development Coordination Analysis on Resource, Production and Consumption: A Provincial Case Study. *Sustainability*, 9(2), 209. <https://doi.org/10.3390/su9020209>